ANALYSIS OF HARD EXCLUSIVE SCATTERING PROCESSES OF THE HERMES RECOIL EXPERIMENT

IRINA BRODSKI

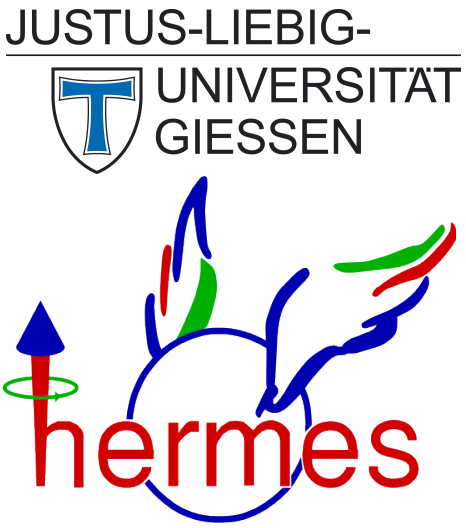

February 21st, 2014

It takes courage to grow up
and become who you really are.

— E. E. Cummings

Dedicated to my family and friends.

ABSTRACT

Deeply virtual Compton Scattering (DVCS), $ep \to ep\gamma$ is the simplest reaction giving indication of generalized parton distributions (GPD) of the nucleon. The DVCS process has the same final state as the Bethe-Heitler process (BH). For this reason the access is taken not through the cross-sections directly but through asymmetries between DVCS events depending on charge and polarization of the 27.6 GeV beam.

For the first time the azimuthal asymmetry amplitudes according the charge of the lepton beam are extracted using a kinematically complete reconstruction method at the HERMES experiment. The recoil detector installed in 2006 allows the reconstruction of recoiling protons that completes the measurements of the forward detector to cover almost the complete angle range around the vertex.

This approach allows suppressing the background processes by almost a complete magnitude compared to the traditional method using only the information of the forward spectrometer.

The analysis of the asymmetries was carried out at different values of the kinematic variables t_c, x_B and Q^2 to investigate the dependence of these variables.

This work pushes the limits of the readability of data and shows which periods have been found to be unstable in the data acquisition. It points out the impact of this finding to previous HERMES publications.

ZUSAMMENFASSUNG

Tiefvirtuelle Compton Streuung (DVCS), $ep \to ep\gamma$, ist die einfachste Reaktion, die Hinweise auf die Struktur der Generalisierten Parton Verteilungen (GPDs) im Nukleon gibt. Der DVCS Prozess unterscheidet sich im Endzustand nicht vom Bethe-Heitler Prozess. Daher erfolgt der Zugang nicht über die Wirkungsquerschnitte direkt, sondern durch die Messung der azimutalen Asymmetrien zwischen DVCS Ereignissen, in Abhängigkeit von Ladung und Polarisation des 27,6 GeV Leptronenstrahls.

Erstmals wurden aus Daten des Experiments HERMES Asymmetrieamplituden bezüglich der Strahlladung mit vollständiger kinematischer Rekonstruktion extrahiert. Hierzu wurden Daten des 2006 installierten Rückstreudetektors (recoil detector) ausgewertet, die auch die Messergebnisse zu rückgestreuten Teilchen erfasst. Zusammen mit dem Vorwärtsdetektor ist so eine fast vollständige Abdeckung über alle Winkelbereiche um den Vertex gewährleistet.

Auf diese Weise kann die Kontamination der Datensätze durch Untergrundprozesse gegenüber der traditionellen Methode, die nur den Vorwärtsdetektor benutzt, um fast eine ganze Größenordnung unterdrückt werden.

Die Auswertung der Asymmetrien erfolgte für verschiedene Werte der kinematischen Variablen t_c,x_B und Q^2, so dass deren Abhängigkeit von diesen Variablen untersucht werden konnte.

Diese Arbeit stößt an die Grenzen der Auswertbarkeit der Daten und zeigt, welche Zeiträume sich bei der Datenname als instabil erwiesen haben und zeigt auf, welche Auswirkungen diese Erkenntnis auf bisherige HERMES Veröffentlichungen hat.

CONTENTS

1 INTRODUCTION

The HERMES experiment at the DESY research center in Hamburg/Germany was built to investigate the quark-gluon structure of matter. One of its main purposes was to study the spin structure of the nucleon.

In the formalism of the Generalized Parton Distributions (GPDs) developed in the last decades a multidimensional description of the nucleon is possible. GPDs are directly connected with the parton distribution functions (PDFs) and nucleon form factors (FFs). They are the natural complement to the Transverse Momentum Dependent Parton Distributions (TMDs), as both are derived from the same parent WIGNER distributions. Since Ji [53] showed that GPDs might provide an access to the composed nucleon spin through the total angular momentum carried by quarks and gluons in the nucleon they became even more a focus of interests.

Experiments can put constraints on the so called COMPTON form factors, that have pendants on the GPDs, as will be explained in this Thesis, by measuring electromagnetic leptoproduction processes. The simplest process used for this purpose is the Deep Virtual COMPTON scattering (DVCS) $ep \to ep\gamma$. It is experimentally indistinguishable from the BETHE-HEITLER Process (BH) where the final state photon comes not from the proton but from bremsstrahlung before or after the interaction of the electron and the BH cross section is dominant at HERMES energies. The HERMES experiment measured azimuthal asymmetries in the DVCS/BH channel depending on the charge and helicity of the beam.

Until 2006 the reconstruction of $ep \to ep\gamma$ was performed with the so called missing mass technique where the kinematics of the recoiling proton where calculated from the measurement of leptons and photons in the forward spectrometer.

The HERMES spectrometer was upgraded with a recoil detector in winter 2005/2006 that allowed a kinetically complete measurement of the process. It consisted of a set of Silicon Strip Detectors (SSD) situated inside the HERA beam vacuum, a Scintillating Fiber Tracker (SFT) and a Photon Detector (PD). This allowed an effective suppression of background processes by almost one order of magnitude.

In this thesis for the first time the extraction of a beam charge asymmetry is performed using this kinematically complete data set. It provides constraints to the real part of the CFF $\mathcal{H}$ related to the GPD H. A special challenge for is the fact that there are limited statistics of the 2 years of data taking with the recoil detector. In this time not always the complete recoil detector was available and the beam charge was changed only once. No electron data is available with the complete recoil detector working. Only the SFT is available throughout the whole time.

The results complement the already published beam charge asymmetry with a kinematically complete data set and are compared with the results from traditional analysis extracted without the recoil detector.

Part I

THEORETICAL FUNDAMENTALS

If you wish to make an apple pie from scratch,
you must first invent the universe.

— Carl Sagan

2

THEORETICAL BACKGROUND

This chapter contains the theoretical background of this thesis's analysis. In the beginning basics of particle physics are introduced. Then the description of the nucleon structure through GPDs (Generalized Parton Distributions) will be derived from WIGNER distributions in a uniform formalism. The different steps can be found in various sources and this thesis intends to show the complete derivation way.

Afterward the GPDs will be linked to DVCS (Deep Virtual Compton Scattering) which is the simplest process where GPDs are being applied. The why and how of DVCS studies through asymmetries in beam spin and charge will be argued.

The properties of GPDs and their meaning in particle physics will be demonstrated. Therefore they are linked to quantities like nucleon spin and well known DIRAC and PAULI form factors. Finally fitting models of GPDs will be introduced.

2.1 PARTICLE PHYSICS BASICS

The established picture of matter [70] is summarized in the so-called standard model in particle physics as outlined in Table 2.1.1 on page 6. This model unites the concept of particles and forces and organizes elementary particles in families depending on their properties. Every fundamental spin $\frac{1}{2}$ particle has a correspondence to an anti-particle.

The basic quantum numbers like charge and color are the main characteristic of these smallest constituents of matter. These particles interact through gauge bosons of the fundamental interactions (see Table 2.1.2 on page 6) types that couple to different quantum numbers. The gauge bosons allow an exchange of energy, momentum, spin and others between different particles and the building of composite particles out of elementary constituents. The most well known composite particles are the nucleons: protons and neutrons building all nuclei in known matter.

Neutrinos ($\nu_{e,\mu,\tau}$) are electrically neutral. They carry the so-called weak charge. The only interactions they participate in are the weak interaction and gravitation. They are nearly massless and can be observed in the beta decay. Electrons (e), muons (μ) and tau (τ) are charged, massive leptons. In nature electrons surround every nucleus in nature, most muons and tauons arrive on the surface of earth through scattering reactions in the atmosphere. These leptons participate in electromagnetic and weak interactions.

Quarks form a huge number of different composed particles, they carry a color. Composed particles are called hadrons. They are color neutral carrying all three colors, all three anti colors or a matching color and anti color. Quarks can never be found solitary or in colored compositions in experiments. Hadrons participate in all types of interactions.

Fermions	Families 1	2	3	electr. charge	color	spin
Leptons	ν_e	ν_μ	ν_τ	0	-	$\frac{1}{2}$
	e	μ	τ	-1		
Quarks	u	c	t	$\frac{2}{3}$	r,b,g	$\frac{1}{2}$
	d	s	b	$-\frac{1}{3}$		

Table 2.1.1: The standard model. Fermions are classified as leptons and Quarks. The 3 lepton families contain a lepton and a lepton neutrino each, the elementary quarks are the up (u), down (d), strange (s), charm (c), top (t) and bottom (b) quark in the order of their weight from he lightest to the heaviest.

Interaction	couples to	particle	mass	spin
strong	color	gluon	0	1
electromagnetic	electric charge	photon (γ)	0	1
weak	weak charge	$W^{\pm}/Z^o$	80/91 GeV	1
gravitation	mass	graviton (hypothetical)	0 (hypothetical)	2

Table 2.1.2: The 4 interaction types in physics. The strong and weak interaction has a very short range. It is most relevant at very short ranges inside a nucleon or in Meson decays, the weak interaction the only one that can cause a change from for example an electron neutrino to an electron or from an up to a down quark. The range of electromagnetic and gravitation forces is not limited but it decreases with the distance. The interaction types are transmitted by the gauge bosons, where only $W^{\pm}$, *and* Z^o bosons are known to be massive.

2.1.1 *The compound nucleon*

Nucleons (protons and neutrons), components of all nuclei, are compound systems build of quarks and bound by gluons. Their main constituents, called valence quarks, are the up (u) and down (d) quarks, the lightest two types. A proton consist of two valence up and one down quark (uud), and neutrons of two valence down and one up quark (udd). In the naive quark model picture the quantum numbers of nuclei are assumed to be a sum of the quantum numbers of the valence quarks. For example the proton's charge can be summed up from the overall charge of two up and one down quark. Same works for the spin, if the two up quarks pair up with opposite spin fulfilling the PAULI principle that forbids for two fermions to have the very same quantum numbers, but this assumption was proven too simple by experiments.

It was shown that a nucleon has far more constituents than the valence quarks. Pairs of quarks and anti quarks and gluons appear and disappear in every moment in the strong interaction between the nucleon's constituents forming the so-called quark sea. The frequentness by which one type of quark and anti quark pairs appears depends on the mass of the quark type and the resolution which is used for probing the nucleon structure in the experimental setup.

2.1.2 *The nucleon structure puzzle*

One of the biggest puzzles in the particle physics of the last decades was the so-called spin puzzle [61]. The EMC experiment [26, 27] showed that the valence quarks carry only $\frac{1}{8}$ the only the nucleon spin. The spin crisis was proclaimed. The HERMES experiment was designed to investigate the spin puzzle and explain how the spin of the nucleon is composed.

Even now, 25 years after the spin crises, the swirling sea of quarks and gluons poses particle physicists a riddle while they step forward describing the structure of the nucleon.

2.2 WIGNER DISTRIBUTIONS

WIGNER [77] was searching for a handy expression for the matrix Q and the HAMILTONian operator H in the NEWMAN formula.

In 1932 he framed a formalism for quantum mechanics that uses a distribution function $W(x;p)$ which unites spatial and momentum properties.

He suggested a projection of a HILBERT space function to a real function

$$\begin{aligned} W(x;p) &= \pi^{-n} \int d^n q \psi^*(\overline{p}+\overline{q})\psi(\overline{p}-\overline{q})e^{i\overline{x}\cdot\overline{q}} \\ &= \pi^{-n} \int d^n q \langle \overline{p}-\overline{q} \mid \hat{\rho} \mid \overline{p}+\overline{q} \rangle \end{aligned}$$

and derived Q and H from there. While WIGNER used n-dimensional functions for a most general formalism, this section will look at the 3-dimensional case for space and momentum each.

$W(x;p)$ are real functions that are not necessary positive definite if they do not describe coherent states or a superposition of these. They can not be interpreted as a

probability distribution themselves but an integration over x or p gives the distribution a separate probability character:

$$\int W(x;p)d^3p = \langle x \mid \hat{\rho} \mid x \rangle \quad \text{and} \quad \int W(x;p)d^3x = \langle p \mid \hat{\rho} \mid p \rangle \tag{2.2.1}$$

and

$$\int W(x;p)d^3p = \mid \psi(x) \mid^2 \quad \text{and} \quad \int W(x;p)d^3x = \mid \phi(x) \mid^2 \tag{2.2.2}$$

for a mixed state ψ.

For every quantum state and a quantity $f(x) + g(x)$ the average is given by [71]

$$\langle f(x) + g(x) \rangle = \int (f(x) + g(x))W(x;p)d^3xd^3p \tag{2.2.3}$$

For their special properties WIGNER functions are used in many fields. In optics to describe "a signal in space and (spatial) frequency simultaneously and can be considered as the local frequency spectrum of the signal" [29]. Also they are used for "multidimensional vector signals, non stationary random processes, linear time-varying systems (deterministic and random), linear signal spaces, and frames" [65].

In the following this section will focus on the application of WIGNER distributions in particle physics, especially centering on the structure of the nucleon. To explore the 3 dimensional picture of the nucleon in spatial and momentum parameters we choose a projection [54][32]

$$\Psi(x) \to W(x,p) = \int \mathrm{d}\eta e^{ip\eta} \langle x + \eta/2 \mid \hat{\rho} \mid x - \eta/2 \rangle \tag{2.2.4}$$

for a state $\hat{\rho} = \mid \psi \rangle\langle \psi \mid$ and $\psi(x + \eta/2) = \langle x + \eta/2 \mid \psi \rangle$

$$\Psi(x) \to W(x,p) = \int \mathrm{d}\eta e^{ip\eta} \psi^*(x - \eta/2)\psi(x + \eta/2) \tag{2.2.5}$$

These functions are reduced via integration to an experimentally accessible number of dimensions as will be described in section 2.3 to the so-called [68] 5-dimensional GTMDs (Generalized Transverse-Momentum Dependant parton Distributions) with two position and three momentum dimensions. These can be reduced [54] even further to the GPDs (Generalized Parton Distributions) or TMDs (Transverse Momentum Distributions). Figure 2.2.1 on page 9 shows the reduction of the GTMDs by three possible methods: Setting of the energy transfer $\Delta = 0$, integration over the space or the perpendicular momentum dimensions. Depending on the method applied, different objects describing the nucleon structure are calculated.

WIGNER functions are a powerful tool that is used in many applications that demand a spatial and momentum description of a state. Such functions were mentioned by Heisenberg [50] and Dirac [43] but they were only seen as an approximation to a quantum mechanical description of a system.

2.3 GPD THROUGH WIGNER DISTRIBUTIONS

The WIGNER distributions have too many dimensions to be accessed completely. No experiment could be developed to measure all degrees of freedom at the same time. For this reason a reduction in dimensions is necessary. Two main ways are the reduction of space or of momentum dimensions.

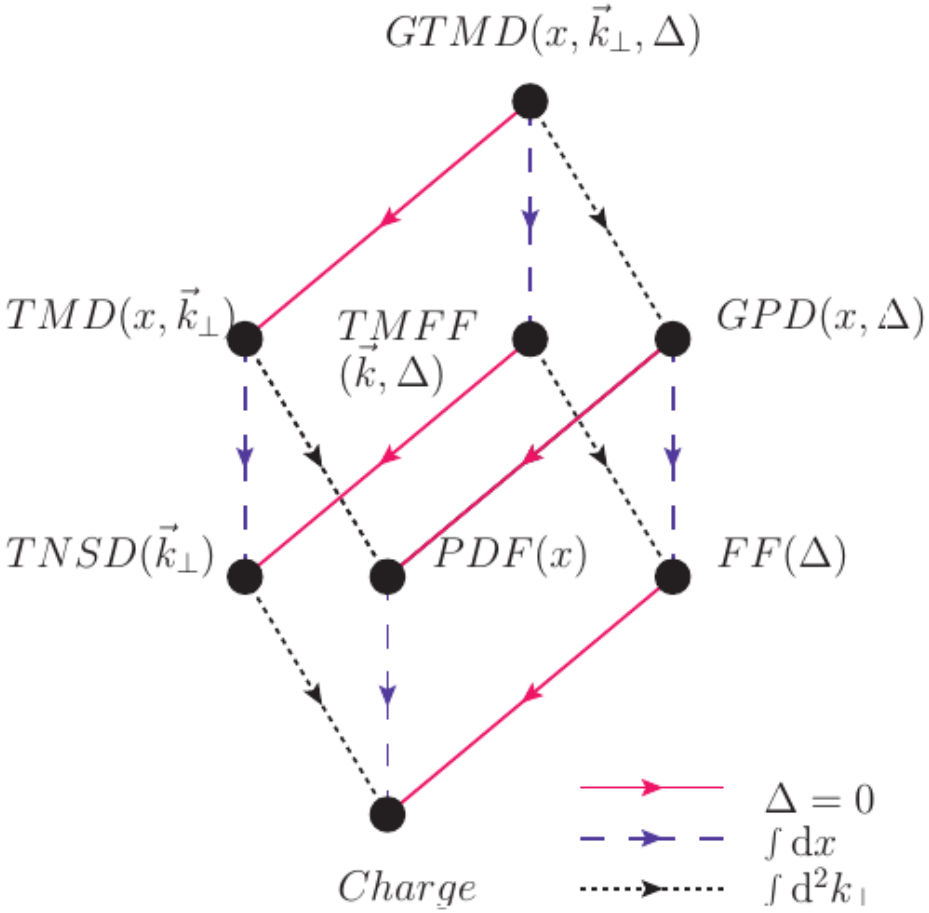

Figure 2.2.1: Connection between GTMDs, GPDs, TMDs, form factors, and particle charge. The lines display transformations between them. Red line means setting Δ to 0. Blue line means integration over x, black line means integration over $k_\perp$

2.3.1 *Wigner functions for parton distributions*

For the WIGNER function

$$\Psi(r) \to W(r,p) = \int \mathrm{d}\eta e^{ip\eta} \psi^*(r-\eta/2)\psi(r+\eta/2) \tag{2.3.1}$$

the WIGNER distribution operator is defined as

$$\hat{\mathcal{W}}_\Gamma(\vec{r},k) = Tr(\Gamma W(r,p)) = \int d^4\eta \; e^{ik\eta} \overline{\Psi}(\vec{r}-\eta/2)\Gamma\Psi(\vec{r}+\eta/2) \tag{2.3.2}$$

Here Γ is a DIRAC matrix defining the type of quark densities for future expansion on the light cone. A nice introduction to the light cone coordinates was written by John C. Collins in 1997 [42].

As the product of two quark fields at different space time points is not automatically gauge-invariant we add a gauge link to space-time infinity along a constant four vector ζ^μ

$$\Psi(\eta) = exp[-ig\int_\eta^\infty \mathrm{d}\bar{t} A_\mu(t)]\psi(\eta) = \underbrace{exp[-ig\int_0^\infty d\lambda\zeta A(\lambda\zeta+\eta)]}_{\text{Wilson line}}\psi(\eta) \tag{2.3.3}$$

although any choice of ζ^μ is possible it is constraint, in real observables, to choose the light-cone vector n^μ by experimental probes. (A brief introduction to WILSON lines can be found in Section A.1.) Now the operator $\mathcal{W}_\Gamma$ is gauge independent but depends on n^μ. The gauge potential only vanishes at the space-time infinity in non singular gauges!

The WIGNER distribution can be written as the expectation value of $\mathcal{W}_\Gamma$ averaging over all possible 3-momentum transfers constructed in the BREIT frame:

$$\begin{aligned} W_\Gamma(\vec{r},k) &= \frac{1}{2}\int \frac{\mathrm{d}^3\tilde{\mathrm{q}}}{(2\pi)^3}\langle \tilde{\mathrm{q}}_2 \mid \mathcal{W}_\Gamma(\vec{r},k) \mid \vec{q}_1\rangle \\ &= \frac{1}{2}\int \frac{\mathrm{d}^3\tilde{\mathrm{q}}}{(2\pi)^3} e^{-i(\vec{q}_2-\vec{q}_1)\vec{r}}\langle \vec{q}_2 = \vec{q}/2 \mid \mathcal{W}_\Gamma(0,k) \mid \vec{q}_1 = -\vec{q}/2\rangle \\ &= \frac{1}{2}\int \frac{\mathrm{d}^3\tilde{\mathrm{q}}}{(2\pi)^3} e^{-i(\vec{q})\vec{r}}\langle \vec{q}/2 \mid \mathcal{W}_\Gamma(\vec{0},k) \mid -\vec{q}/2\rangle \end{aligned}$$

Initial and final state are taken with a different $\vec{q}$, otherwise it would result in a trivial $\vec{r}$ dependence.

The GTMDs mentioned in Section 2.2 are FOURIER transformation of the WIGNER distributions [68].

2.3.2 *Reducing* WIGNER *distributions to GPDs*

The phase space as defined in the last subsection depends on seven independent variables, almost impossible to be accessed in one experiment. For this reason it is of utmost importance to reduce the number of the degrees of freedom.

Using lightcone coordinates to express the vector $\vec{k} = (k^0,k^1,k^2,k^3)$ we get $k^+ = k^0+k^3$, $k^- = k^0-k^3$ and $k^\perp = (k^1,k^2)$.

In high energy experiments we can assume $k^0 \sim k^3$. This in change leads to $k^- \ll k^+$. So we can integrate out k^- without a huge information loss.

$$W_\Gamma(\vec{r},\vec{k}) = \int \frac{dk^-}{(2\pi)^2} \mathcal{W}_\Gamma(\vec{r},k) \tag{2.3.4}$$

To reduce the WIGNER distributions furthermore we can now integrate out the transverse momentum too. We have the 4 dimensional quantum distribution

$$\begin{aligned} \tilde{f}_\Gamma(\vec{r},k^+) &= \int \frac{d^2\vec{k}_\perp}{(2\pi)^2} W_\Gamma(\vec{r},\vec{k}) \\ &= \frac{1}{2}\int \frac{d^3\vec{q}}{(2\pi)^3} e^{-i\vec{q}\vec{r}} \int \frac{d\eta^-}{2\pi} e^{-i\eta^- k^+} \\ &\quad \times e^{-i\vec{q}\vec{r}} \langle \vec{q}/2 \mid \overline{\Psi}(-\frac{\eta}{2})\Gamma\Psi(+\frac{\eta}{2}) \mid -\vec{q}/2\rangle \end{aligned}$$

or rewritten with:
$k^+ = xp^+$, $E_q = \sqrt{M^2 + (\frac{\vec{q}}{2})^2}$ and $\eta^- = \lambda/p^+$

$$\tilde{f}_\Gamma(\vec{r},k^+) = \int \frac{d^3\vec{q}}{(2\pi)^3} e^{-i\vec{q}\vec{r}} F_\Gamma(x,\xi,t) \tag{2.3.5}$$

where the so-called skewness is $\xi = q^3/(2E_q)$, $Q^2 = -q^2$ and n=(1,0,0,-1) pointing the direction of the gauge link along (near) light cone

$$F_\Gamma(x,\xi,t) = \int \frac{d\lambda}{2\pi} e^{i\lambda x} \langle \vec{q}/2 \mid \overline{\Psi}(-\frac{\lambda n}{2})\Gamma\Psi(+\frac{\lambda n}{2}) \mid -\vec{q}/2\rangle \tag{2.3.6}$$

Γ is a vector of the orthonormal basis:

$$\Gamma \in \{\mathbf{1}, \gamma^\mu, \gamma^\mu\gamma_5, i\gamma_5, i\sigma^{\mu\nu}\gamma_5\} \tag{2.3.7}$$

We select for the leading twist $\Gamma = \gamma^+, \gamma^+\gamma_5, \sigma^{+\perp}\gamma_5$.
That gives the leading twist form factors

$$F_{\gamma^+}(x,\xi,t) = \frac{1}{2p^+}\int \frac{d\lambda}{2\pi} e^{i\lambda x} \langle p' = \vec{q}/2 \mid \overline{\Psi}(-\frac{\lambda n}{2})\gamma^+\Psi(+\frac{\lambda n}{2}) \mid p = -\vec{q}/2\rangle \tag{2.3.8}$$

To decompose the expression we use the ansatz that contains every possible vectorial combination of p and p′:

$$\Lambda^+(p,p') = A(q^2)\gamma^+ + B(q^2)p^+ + C(q^2)p'^+ + D(q^2)\sigma^{+\nu}p_\nu + E(q^2)\sigma^{+\nu}p'_\nu \tag{2.3.9}$$

Current conservation requires $q_\mu\Lambda^\mu(p,P') = 0 \Rightarrow C = B;\ E = -D$
Hermeticity requires: A,B are purely real, D purely imaginary

$$\Lambda^+(p,p') = A(q^2)\gamma^+ + B(q^2)\underbrace{(p^+ + p'^+)}_{0} + D(q^2)\sigma^{+\nu}\underbrace{(p_\nu - p'_\nu)}_{q_\mu} \tag{2.3.10}$$

With these constrains $F_{\gamma^+}(x,\xi,t)$ decomposes to

$$F_{\gamma^+}(x,\xi,t) = \frac{1}{2p^+}\overline{U}(\vec{q}/2)[H(x,\xi,Q^2)\gamma^+ + E(x,\xi,Q^2)\frac{i\sigma^{\nu}q_{\nu}}{2M}]U(-\vec{q}/2) \tag{2.3.11}$$

The other F_Γ terms are decomposed in a comparable way which will not be derived here in detail and read as:

$$\begin{aligned} F_{\gamma^+\gamma_5}(x,\xi,t) &= \frac{1}{2p^+}\int\frac{d\lambda}{2\pi}e^{i\lambda x}\langle p' = \vec{q}/2 \mid \overline{\Psi}(-\frac{\lambda n}{2})\gamma^+\gamma_5\Psi(+\frac{\lambda n}{2}) \mid p = -\vec{q}/2\rangle \\ &= \frac{1}{2p^+}\overline{U}(\vec{q}/2)[\tilde{H}(x,\xi,Q^2)\gamma^+ + \tilde{E}(x,\xi,Q^2)\frac{i\sigma^{\nu}q_{\nu}}{2M}]U(-\vec{q}/2) \end{aligned}$$

and

$$\begin{aligned} F_{\sigma^{+j}\gamma_5}(x,\xi,t) &= \frac{1}{2p^+}\int\frac{d\lambda}{2\pi}e^{i\lambda x}\langle p' = \tilde{q}/2 \mid \overline{\Psi}(-\frac{\lambda n}{2})\sigma^{+j}\gamma_5\Psi(+\frac{\lambda n}{2}) \mid p = -\vec{q}/2\rangle \\ &= \frac{1}{2p^+}\overline{U}(\vec{q}/2)[H_T(x,\xi,Q^2)\sigma^{+\mu}\gamma_5^+ + \tilde{H}_T(x,\xi,Q^2)\frac{i\epsilon^{+j\mu\nu}q_\mu p_\nu}{M^2} \\ &\quad + E_T(x,\xi,Q^2)\frac{i\epsilon^{+j\mu\nu}q_\mu\gamma_\nu}{2M} + \tilde{E}_T(x,\xi,Q^2)\frac{i\epsilon^{+j\mu\nu}p_\mu\gamma_\nu}{M}]U(-\vec{q}/2) \end{aligned}$$

The linear factors $H(x,\xi,Q^2)$, $E(x,\xi,Q^2)$, $\tilde{H}(x,\xi,Q^2)$, $\tilde{E}(x,\xi,Q^2)$, $H_T(x,\xi,Q^2)$, $E_T(x,\xi,Q^2)$, $\tilde{H}_T(x,\xi,Q^2)$ and $\tilde{E}_T(x,\xi,Q^2)$ are the so-called GPDs. Their values can not be derived from this theory. For this reason the different terms of F_Γ need to be accessed in experiments and fitted to the experimental data.

2.3.3 *Reducing* Wigner *distributions to TMDs*

An other reduction which is made from the Wigner phase space distribution are the TMDs. In difference to the GPD derivation the spatial degrees of freedom are integrated out.

Starting from the same point as in 2.3.2 we integrate

$$W_\Gamma(\vec{r},\vec{k}) = \int\frac{dk^-}{(2\pi)^2}\tilde{W}_\Gamma(\vec{r},k) \tag{2.3.12}$$

over $\vec{r}$ and obtain for leading twist $\Gamma = \gamma^+, \gamma^+\gamma_5, \sigma^{+\perp}\gamma_5$ [54]

$$\begin{aligned} \int\frac{\mathrm{d}^3\vec{r}}{(2\pi)^2}W_{\gamma^+}(\vec{r},\vec{k}) &= q(x,k_\perp) + q_T(x,k_\perp)(\hat{k}_\perp\times\hat{S}_\perp)\cdot\hat{P} \\ &= \frac{1}{2}\int\frac{\mathrm{d}^2\eta_\perp\mathrm{d}\eta^-}{(2\pi)^3}e^{i(k^+\eta^- - \vec{k}_\perp\cdot\vec{\eta}_\perp)}\langle P \mid \overline{\Psi}(0)\gamma^+\Psi(\eta^-,\vec{\eta}_\perp) \mid P\rangle \end{aligned}$$

$$\begin{aligned} \int\frac{\mathrm{d}^3\vec{r}}{(2\pi)^2}W_{\gamma^+\gamma_5}(\vec{r},\vec{k}) &= \Delta q_L(x,k_\perp)(S\cdot n) + \Delta q_T(x,k_\perp)(\hat{k}_\perp\times\hat{S}_\perp) \\ &= \frac{1}{2}\int\frac{\mathrm{d}^2\eta_\perp\mathrm{d}\eta^-}{(2\pi)^3}e^{i(k^+\eta^- - \vec{k}_\perp\cdot\vec{\eta}_\perp)}\langle P \mid \overline{\Psi}(0)\gamma^+\gamma_5\Psi(\eta^-,\vec{\eta}_\perp) \mid P\rangle \end{aligned}$$

$$\begin{aligned}\int \frac{d^3\vec{r}}{(2\pi)^2} W_{\sigma^{+\perp}\gamma_5}(\vec{r},\vec{k}) &= \delta q_L(x,k_\perp)\hat{S}_T + \delta q_{T'}(x,k_\perp)\hat{k}_\perp(\hat{k}_\perp\cdot\hat{S}_\perp) \\ &+ \delta q_L(x,k_\perp)\hat{k}_\perp(S\cdot n) + \delta q(x,k_\perp)\hat{k}_\perp \\ &= \frac{1}{2}\int \frac{d^2\eta_\perp d\eta^-}{(2\pi)^3} e^{i(k^+\eta^- - \vec{k}_\perp\cdot\vec{\eta}_\perp)} \langle P \mid \overline{\Psi}(0)\gamma^+\gamma_5\Psi(\eta^-,\vec{\eta}_\perp) \mid P\rangle\end{aligned}$$

The linear coefficients $q(x,k_\perp)$, $q_T(x,k_\perp)$, $\Delta q_L(x,k_\perp)$, $\Delta q_T(x,k_\perp)$, $\delta q_L(x,k_\perp)$ and $\delta q_T(x,k_\perp)$ are called TMDs (Transverse Momentum Distributions). They are the momentum counterpart to the GPDs and draw a multidimensional picture of the nucleon in momentum space.

2.4 GPDS THROUGH DVCS

DVCS is the simplest process that is connected to the GPDs. In this section its properties will be explained, how it can be accessed in an experiment and what the experimental limits are.

2.4.1 *Deep inelastic scattering*

In scattering experiments with leptons and nucleons an amount of energy $q = ((E-E'),\vec{q})$ is transferred from e.g. an accelerated lepton with energy E to a fixed target nucleon through a virtual photon. This way the lepton is deflected and can be measured somewhere in the detector setup. Depending on the amount of transferred energy the scattering is more or less elastic. Figure 2.4.1 on page 14 shows the scattering spectrum from elastic to inelastic scattering. Besides of the elastic peak at smaller energies of the scattered lepton several other peaks are visible. They occur from nucleon excitation states. With falling E' the transferred 4-momentum q rises. Its negative square is a common quantity in scattering physics $Q^2 = -q^2$. At even higher q values the inelastic scattering is called deep inelastic scattering (DIS). The elasticity of a scattering reaction is expressed in terms of the lorence invariant BJÖRKEN scaling variable

$$x = \frac{Q^2}{P\cdot q} \tag{2.4.1}$$

with the nucleon 4-momentum P. Figure 2.4.2 on page 14 scratches the scattering reaction at different values of x. A schematic picture of the DIS is displayed in 2.4.3. The incoming lepton with 4-momentum $k = (e_l,\vec{p}_l)$ exchanges a virtual photon (q) with the target ($P = (E_P,\vec{p}_P)$). One of the target quarks absorbs the energy and hadronizes into a reaction product X_q. The other part of the proton reacts to the final state product X_P

2.4.2 *Deeply Virtual* COMPTON *Scattering*

The deep virtual COMPTON scattering (DVCS) is a special case of the DIS. The final state of this process contains the scattered electron, a real photon and the recoiling

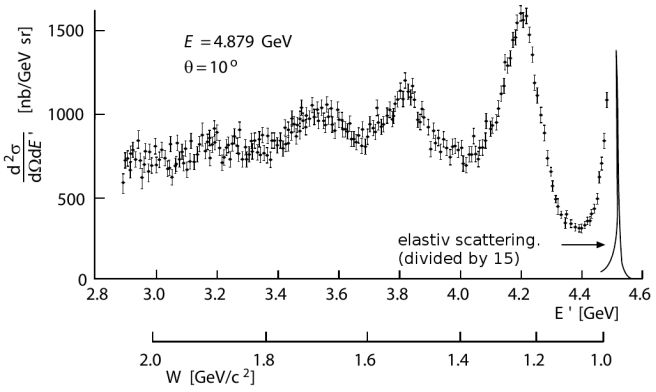

Figure 2.4.1: [70] Spectrum of electron proton scattering at an electron energy of E = 4.9 GeV and a scattering angle of $\theta = 10°$. This spectrum was taken varying the accepted scattering energy in the magnetic spectrometer in small steps.

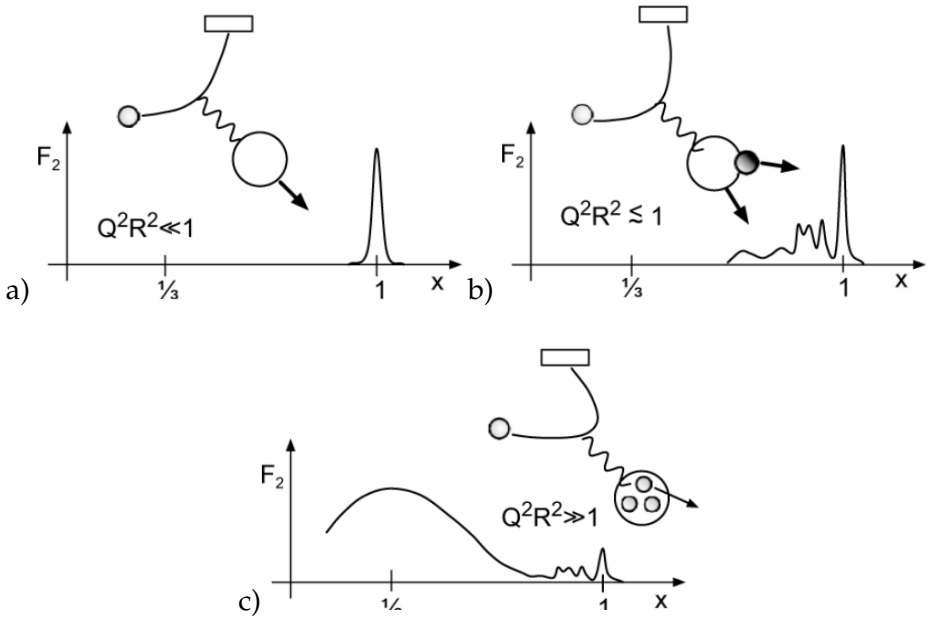

Figure 2.4.2: [70] a) At small Q^2 the wavelength of the virtual photon is much larger then the nucleon radius R. The reaction is completely elastic. b) The virtual photon's wavelength is of the same magnitude as the radius of the nucleon. The inelastic scattering produces exited nucleon states. c) At high Q^2 where $x \ll 1$ the scattering becomes deeply inelastic. The energy is transfered to the nucleons charged constituents, the quarks.

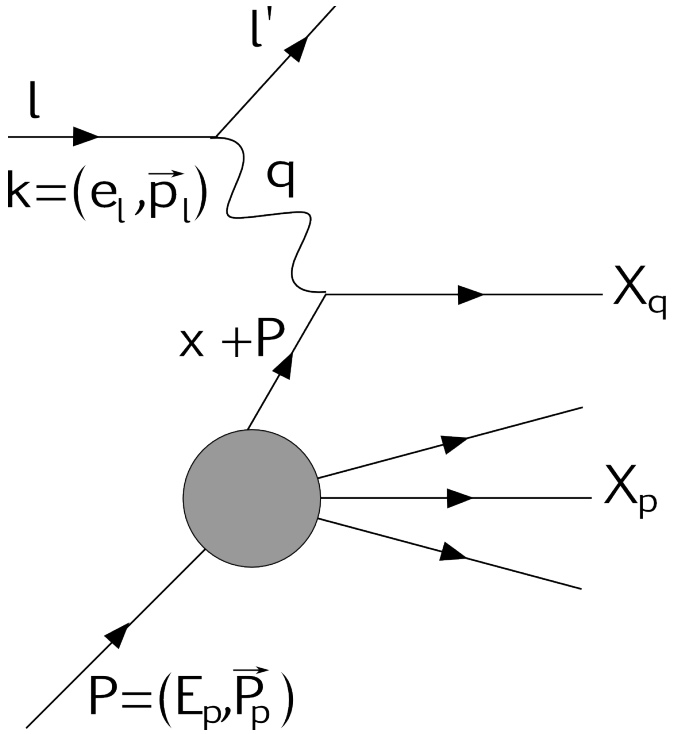

Figure 2.4.3: Deep inelastic scattering. Incoming lepton exchanges a virtual photon with a quark of a target proton and transfers the momentum fraction q. In the final state there is the scattered lepton and the scattering products X_q from the interacting quark and the transferred energy q and X_p from the other quarks of the scattered proton.

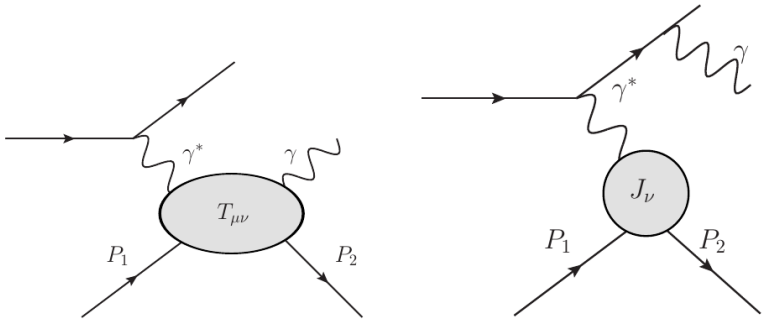

Figure 2.4.4: Deep virtual Compton scattering (l) and Bethe Heitler process (r)

proton visualized in Figure 2.4.4 on page 16. In terms of 2.4.1 the reaction product X_q is a photon and X_P is a proton. In the energy range of the HERMES experiment the DVCS process is dominated by the cross section of the so-called Bethe-Heitler process (BH) by more than one magnitude. Having the same initial and final state as DVCS, but the real photon is not produced in the interaction with the nucleon but comes from bremsstrahlung of the lepton before or after the interaction.

Both processes can be described by their reaction equation

$$l(k,\lambda)N(P_{1,}S_1) \rightarrow l(k',\lambda)N(P_2,S_2)\gamma(q_2,\Lambda) \tag{2.4.2}$$

with the 4-momenta $k = (\vec{k},\omega), k' = (\vec{k'},\omega'),\ P_{1,2} = (\vec{P_{1,2}},E_{1,2}),\ q_2 = (\vec{q}_2,\nu)$ and the spins $\lambda,\ S_{1,2},\ \Lambda$.

According to Fermi's golden rule the cross section reads

$$\begin{aligned} \mathrm{d}\sigma &= \frac{1}{k.P_1} \mid \mathcal{T} \mid^2 (\lambda,S_1)(2\pi)^4\delta(k+P_1-k'-P_2-q_2) \\ &\times \frac{\mathrm{d}^3\vec{k'}}{2\omega'(2\pi^3)}\frac{\mathrm{d}^3\vec{P}_2}{2E_2(2\pi^3)}\frac{\mathrm{d}^3\vec{q}_2}{2\nu(2\pi^3)} \end{aligned}$$

As an overlap of the scattering amplitudes for DVCS and BH $\mid \mathcal{T} \mid^2$ can be written as

$$\mid \mathcal{T} \mid^2 (\lambda,S_1) = \sum_{\lambda',S_2,\Lambda} \left\{ \mid \mathcal{T}_{DVCS} \mid^2 + \mid \mathcal{T}_{BH} \mid^2 + \underbrace{\mathcal{T}_{DVCS}\mathcal{T}^*_{BH} + \mathcal{T}^*_{DVCS}\mathcal{T}_{BH}}_{\text{interference term } \mathcal{I}} \right\} \tag{2.4.3}$$

$\mid \mathcal{T}_{DVCS} \mid^2$ is magnitudes smaller than $\mid \mathcal{T}_{BH} \mid^2$ but in the interference term $\mathcal{I}$ the amplitude of the BH process amplifies the contribution of the DVCS process.

The Bethe-Heithler amplitude is pure real [31] and given by a contraction of the leptonic tensor

$$L_{\mu\nu} = \overline{u}(k',\lambda')[\gamma_\mu(\not{k}-\not{q})^{-1}\gamma_\nu + \gamma_\nu(\not{k}+\not{q})^{-1}\gamma_\mu]u(k,\lambda) \tag{2.4.4}$$

with the hadronic current

$$J_\nu = \bar{U}(P_2,S_2)[F_1(\Delta^2)\gamma_\mu + iF_2(\Delta^2)\sigma_{\nu\tau}\frac{q^\tau}{2M}]U(P_1,S_1) \tag{2.4.5}$$

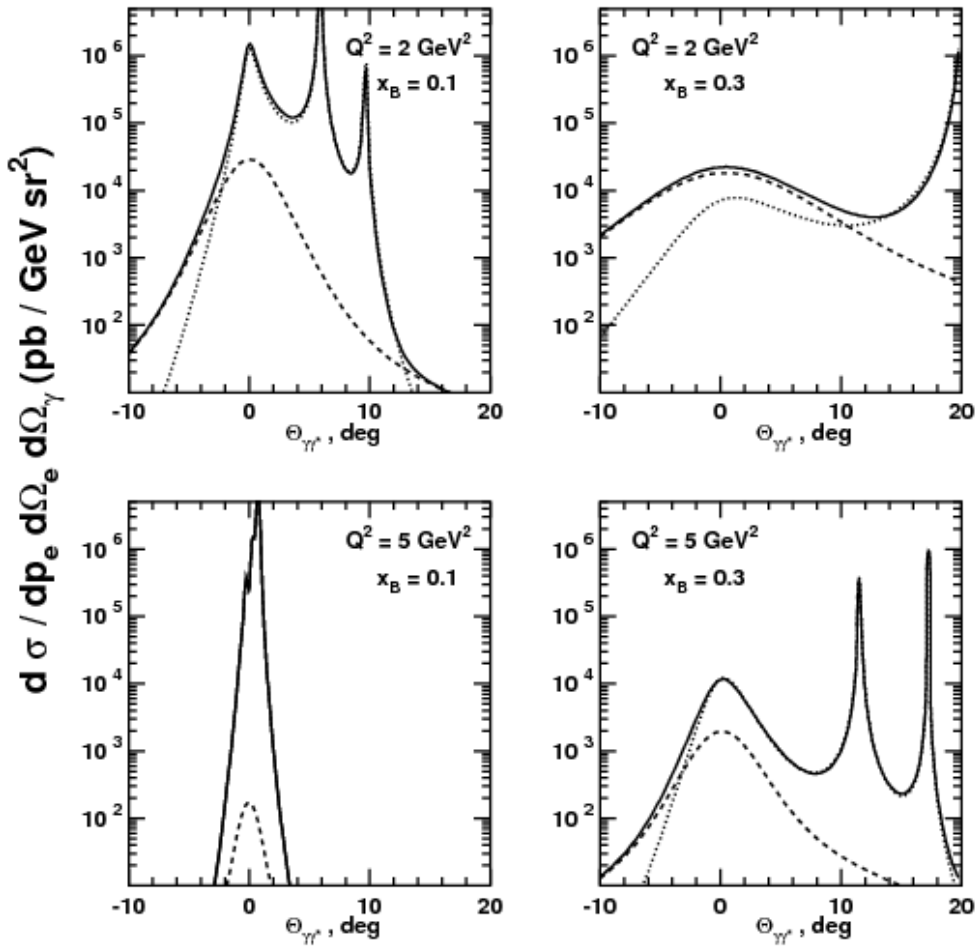

Figure 2.4.5: Illustration of the behavior of the differential cross-sections as a function of the polar angle between the virtual and the real photon for DVCS (dashed lines), Bethe-Heitler (dotted lines) and total γ production (solid lines) in e^+p interactions at HERMES energy $E_e = 27.5GeV$. Different panels are for different values of x_B and Q^2. [59]

where F_1 is the DIRAC form factor and F_2 is the PAULI form factor, both are well known and measured. Section 2.6 will go into more detail about these form factors. The energy transfer is $\Delta = P_2 - P_1 = q_2 - q_1$.

The BH amplitude has the form

$$\mathcal{T}_{BH} = -\frac{e^3}{\Delta^2}\epsilon^*_\mu L^{\mu\nu} J_\nu \tag{2.4.6}$$

with the hadronic current J_ν .

The hadronic tensor for the DVCS process is

$$\mathcal{T}_{VCS} = \pm\frac{e^3}{q_1^2}\epsilon^*_\mu T^{\mu\nu}\gamma_\nu u(k) \tag{2.4.7}$$

with + sign for an electron beam and - sign for a positron beam. We write $T^{\mu\nu}$ as a scalar product of time ordered streams:

$$T^{\mu\nu} = \int \mathrm{d}x e^{ix.q}\langle P_2, S_2 \mid T j_\mu(x/2) j_\mu(x/2) \mid P_1, S_1\rangle \tag{2.4.8}$$

where $q = (q_1 + q_2)/2$.

Its decomposition in its DIRACian parts looks like

$$T^{\mu\nu}(q, P, \Delta) = -\tilde{g}_{\mu\nu}\frac{q_\sigma V_1^\sigma}{P.q} - i\tilde{\epsilon}_{\mu\nu\rho\sigma}\frac{A_1^\sigma}{P.q} + ... \tag{2.4.9}$$

up to the leading twist.

With [33]

$$\begin{aligned} V_{1\mu} &= \overline{U}(P_2, S_2)(\mathcal{H}\gamma_\mu + \mathcal{E}\frac{i\sigma_{\mu\nu}\Delta^\nu}{2M})U(P_1, S_1) \\ A_{1\mu} &= \overline{U}(P_2, S_2)(\tilde{\mathcal{H}}\gamma_\mu + \tilde{\mathcal{E}}\frac{i\sigma_{\mu\nu}\Delta^\nu}{2M})U(P_1, S_1) \end{aligned}$$

$\mathcal{H}$, $\mathcal{E}$, $\tilde{\mathcal{H}}$, $\tilde{\mathcal{E}}$ are the so-called leading twist Compton Form Factors (CFFs) that are a convolution of the already defined GPDs.

$$\{\mathcal{H}, \mathcal{E}\}(\xi) = \int_{-1}^{1} dx C^{(-)}(\xi, x)\{H, E\}(x, \eta) \mid_{\eta=-\xi} \tag{2.4.10}$$

$$\{\tilde{\mathcal{H}}, \tilde{\mathcal{E}}\}(\xi) = \int_{-1}^{1} dx C^{(+)}(\xi, x)\{\tilde{H}, \tilde{E}\}(x, \eta) \mid_{\eta=-\xi} \tag{2.4.11}$$

$C^{(\pm)}$ is implied to be a summation over the quark species as follows

$$C^{(\mp)}F \to \sum_{i=u,d,s} C_i^{(\mp)} F_i \tag{2.4.12}$$

with the perturbative expansion

$$C^{(\mp)} = C^{(\mp)}_{(0)} + \frac{\alpha_s}{2\pi}C^{(\mp)}_{(1)} + \mathcal{O}(\alpha_s^2) \tag{2.4.13}$$

At leading order in α_s it reads as

$$\xi C^{(\mp)}_{(0)i}(\xi, x) = \frac{Q_i^2}{1 - x/\xi - i0} \mp \frac{Q_i^2}{1 + x/\xi - i0} \tag{2.4.14}$$

for the even (-) and odd (+) parity sectors.
[33] also expresses the transverse CFFs as

$$\left\{\mathcal{H}_T, \mathcal{E}_T, \tilde{\mathcal{H}}_T, \tilde{\mathcal{E}}_T\right\}(\xi) = \frac{\alpha_s}{4\pi} \sum_{i=u,d,s} \int_{-1}^{1} dx C^{(+)}_{(0)i}(\xi, x) \left\{H_T, E_T, \tilde{H}_T, \tilde{E}_T\right\}(x, \xi) \tag{2.4.15}$$

2.4.3 *Angular dependence of the DVCS cross section*

The kinematics of the process of interest

$$l(k, \lambda) N(P_1, S_1) \to l(k', \lambda) N(P_2, S_2) \gamma(q_2, \Lambda) \tag{2.4.16}$$

can be described as following:
The incoming lepton l with the 4-momentum k and the polarization λ exchanges a virtual photon with the 4-momentum q_1 with the target nucleon N. The nucleon absorbs the virtual photon, emits a real photon γ and remains in the ground state being scattered and achieving the 4-momentum P_2 and the polarization S_2
The resulting 4-momentum vectors of the involved particles are:

$$\begin{aligned}
\text{incoming lepton} \quad k &= (E, E\sin\theta_l, 0, E\cos\theta_l) \\
\text{virtual photon} \quad q_1 &= (q_1^0, 0, 0, -\mid \vec{q}_1 \mid) \\
\text{resting target proton} \quad P_1 &= (M, 0, 0, 0) \\
\text{recoiled proton} \quad P_2 &= (E_2, \mid \vec{P}_2 \mid \cos\phi \sin\theta_N, \mid \vec{P}_2 \mid \sin\phi \sin\theta_N, \mid \vec{P}_2 \mid \cos\theta_N)
\end{aligned}$$

The angular dependence of the mixed BH/DVCS amplitude

$$\mid \mathcal{T} \mid^2 = \mid \mathcal{T}_{DVCS} \mid^2 + \mid \mathcal{T}_{BH} \mid^2 + \mathcal{I} \tag{2.4.17}$$

reads according to [33] in terms of Fourier factors:

$$\begin{aligned}
\mid \mathcal{T}_{BH} \mid^2 &= \frac{e^6}{x_B^2 y^2 (1+\epsilon^2)^2 \Delta^2 \mathcal{P}_1(\phi) \mathcal{P}_2(\phi)} \\
&\times \left\{ c_0^{BH} + \sum_{n=1}^{2} c_n^{BH} \cos(n\phi) + s_1^{BH} \sin(n\phi) \right\}
\end{aligned}$$

for the BH term, for the DVCS term:

$$\mid \mathcal{T}_{DVCS} \mid^2 = \frac{e^6}{y^2 \mathcal{Q}^2} \left\{ c_0^{DVCS} + \sum_{n=1}^{2} \left[c_n^{DVCS} \cos(n\phi) + s_n^{DVCS} \sin(n\phi) \right] \right\}$$

and for the interference term:

$$\mathcal{I} = \frac{\pm e^6}{x_B^2 y^3 \Delta^2 \mathcal{P}_1(\phi)\mathcal{P}_2(\phi)} \left\{ c_0^{\mathcal{I}} + \sum_{n=1}^{3} \left[c_n^{\mathcal{I}} \cos(n\phi) + s_n^{\mathcal{I}} \sin(n\phi) \right] \right\}$$

with the propagators

$$\mathcal{P}_1 = \frac{1}{y(1-\epsilon)} \{J + 2K\cos(\phi)\} \tag{2.4.18}$$

$$\mathcal{P}_2 = 1 + \frac{\Delta^2}{\mathcal{Q}^2} + \frac{1}{y(1-\epsilon)} \{J + 2K\cos(\phi)\} \tag{2.4.19}$$

where

$$\begin{aligned} K^2 &= \frac{\Delta^2}{\mathcal{Q}^2}(1-x_B)(1-y-\frac{y^2\epsilon^2}{4})(1-\frac{\Delta_{min}^2}{\Delta^2}) \\ &\times \left\{ \sqrt{1-\epsilon} + \frac{4x_B(1-x_B)+\epsilon^2}{4(1-x_B)} \frac{\Delta^2 - \Delta_{min}^2}{\mathcal{Q}^2} \right\} \end{aligned}$$

$$-\Delta_{min}^2 = \mathcal{Q}^2 \frac{2(1-x_B)(1-\sqrt{1-\epsilon}) - \epsilon^2}{4x_B(1-x_B)+\epsilon^2} \tag{2.4.20}$$

and

$$J = (1-y-\frac{y\epsilon^2}{2})(1+\frac{\Delta^2}{\mathcal{Q}^2}) - (1-x)(2-y)\frac{\Delta^2}{\mathcal{Q}^2}, \tag{2.4.21}$$

$$\epsilon \equiv 2x_B \frac{M}{\mathcal{Q}} \text{ and } \Delta_{min} = \frac{-M^2x^2}{(1-x+\frac{xM^2}{\mathcal{Q}^2})} \tag{2.4.22}$$

at the same time they read [31] in terms of CFFs for an unpolarized target ignoring any angle dependence:

$$\begin{aligned} |\,\mathcal{T}_{DVCS,unp}\,|^2 &= \frac{2(2-2y+y^2)}{y^2(2-x)^2\mathcal{Q}^2}[4(1-x)(\mathcal{H}_1\mathcal{H}_1^* + \tilde{\mathcal{H}}_1\tilde{\mathcal{H}}_1^*) \\ &- x^2(\mathcal{H}_1\mathcal{E}_1^* + \mathcal{E}_1\mathcal{H}_1^* + \tilde{\mathcal{H}}_1\tilde{\mathcal{E}}_1^* + \tilde{\mathcal{E}}_1\tilde{\mathcal{H}}_1^*)] \\ &- (x^2 + (2-x)^2\frac{\Delta}{4M^2})\mathcal{E}_1\mathcal{E}_1^* - x^2\frac{\Delta}{4M^2}\tilde{\mathcal{E}}_1^*\tilde{\mathcal{E}}_1] \end{aligned}$$

$$\begin{aligned} |\,\mathcal{T}_{BH,unp}\,|^2 &= \frac{2(2-2y+y^2)}{(1-y)\Delta^2}[4\frac{(1-x)}{x^2}\left(1-\frac{\Delta_{min}^2}{\Delta^2}\right)F_1^2 \\ &- 2(F_1+F_2)^2 + \left(\frac{\Delta_{min}^2}{\Delta^2}-1\right)F_2^2] \end{aligned}$$

$$
\begin{aligned}
|\mathcal{I}_{unp}|^2 &= -\frac{8(2-2y+y^2)\sqrt{1-x}}{\sqrt{1-y}yx\sqrt{-\Delta^2\mathcal{Q}^2}}\sqrt{1-\frac{\Delta^2_{min}}{\Delta^2}}\cos(\phi) \\
&\quad -\mathfrak{Re}\{F_1\mathcal{H}_1+\frac{x}{2-x}(F_1+F_2)\tilde{\mathcal{H}}_1-\frac{\Delta^2}{4M^2}F_2\mathcal{E}_1\} \\
&- \frac{8\lambda(2-y)\sqrt{1-x}}{\sqrt{1-y}x\sqrt{-\Delta^2\mathcal{Q}^2}}\sqrt{1-\frac{\Delta^2_{min}}{\Delta^2}}\sin(\phi) \\
&\quad -\mathfrak{Im}\{F_1\mathcal{H}_1+\frac{x}{2-x}(F_1+F_2)\tilde{\mathcal{H}}_1-\frac{\Delta^2}{4M^2}F_2\mathcal{E}_1\}
\end{aligned}
$$

Comparing the corresponding expressions the FOURIER coefficients can be mapped to terms depending on real or imaginary parts of the CFFs. Depending on the charge and polarization properties of the experimental setup different terms add or cancel out so that different parts of the equation can be accessed as will be explained in the following subsection.

2.4.4 *CFFs through Fourier Coefficients*

Depending on which combination of target nucleon and projectile lepton polarization is chosen in the experiment other CFFs are accessible. For this thesis only data taken with an unpolarized target is used. Furthermore only beam helicity and beam charge asymmetry will be analyzed.

For $|\Delta^2| \ggg |\Delta^2_{min}|$ [31] neglecting terms of $\mathcal{O}(\Delta_{min}/\Delta)$

the cross sections read for unpolarized beam and polarized target:

$$
\begin{aligned}
\Delta_{SL}d\sigma &= d\sigma^{\uparrow}-d\sigma^{\downarrow} \\
&= -\frac{16(2-y)\sqrt{1-x}}{\sqrt{1-y}x\sqrt{-\Delta^2\mathcal{Q}^2}}\sin(\phi_r)\times \\
&\quad \mathfrak{Im}\left\{F_1\mathcal{H}_1+\frac{x}{2-x}(F_1+F_2)\tilde{\mathcal{H}}_1-\frac{\Delta^2}{4M^2}F_2\mathcal{E}_1\right\}d\mathcal{M}
\end{aligned}
$$

and for an unpolarized beam and target but comparing cross sections for different lepton charge

$$
\begin{aligned}
\Delta_C^{unp}d\sigma &= d\sigma^{+,unp}-d\sigma^{-,unp} \\
&= -\frac{16(2-2y+y^2)\sqrt{1-x}}{\sqrt{1-y}yx\sqrt{-\Delta^2\mathcal{Q}^2}}\cos(\phi_r)\times \\
&\quad \mathfrak{Re}\left\{F_1\mathcal{H}_1+\frac{x}{2-x}(F_1+F_2)\tilde{\mathcal{H}}_1-\frac{\Delta^2}{4M^2}F_2\mathcal{E}_1\right\}d\mathcal{M}
\end{aligned}
$$

with $d\mathcal{M}=\frac{\alpha^3xy}{8\pi\mathcal{Q}^2}(1+\frac{4M^2x^2}{\mathcal{Q}})^{-1/2}dxdyd\mid\Delta^2\mid d\phi_r$

From these expressions it is already clear, that DVCS does not give a direct access to the GPDs as only the CFFs' real and imaginary parts can be calculated. They are accessed by measuring asymmetries in cross section comparing cross sections measured with a positively or negatively polarized beam or with different beam spin using an electron and positron beam. This way the dominance of the BH channel loses importance as there is no dependence on beam spin or charge in the $|\mathcal{T}_{BH,unp}|^2$.

2.5 DVCS THROUGH ASYMMETRIES

It has been shown above that the asymmetries in the DVCS cross sections lead to the access to CFFs. To measure asymmetries the charge and polarization of the beam and target are varied.

2.5.1 *Definition of asymmetries*

An asymmetry

$$A_{p_{1/2}c_{1/2}} = \frac{d\sigma_{p_1c_1} - d\sigma_{p_2c_2}}{d\sigma_{p_1c_1} + d\sigma_{p_2c_2}} \tag{2.5.1}$$

is defined as the difference of cross sections with different constellations of polarization p and charge c. Usually in an experiment the cross sections are accessed through event numbers counted by the detector and data acquisition of the experiment.

The measured event number is depended on various parameters as
detector acceptance $a(x, Q^2)$
total detection efficiency $\varepsilon(t, x, Q^2)$
the live time factor $\tau(t) \simeq 0.97$
and the luminosity $L(t)$

$$\begin{aligned} N^{ab} &= a(x,Q^2)\sigma_{UU}(x,Q^2) \times \int \mathrm{d}t\varepsilon(t,x,Q^2)\tau(t)L^{ab}(t) \\ &\times \quad [1 \pm \mid P_B(t)P_z(t) \mid A_{abcd}(x,Q^2)] \end{aligned}$$

N^{ab}stands for the number of events with target polarization b and beam polarization a.

A_{abcd} is the asymmetry between the polarization combination ab and cd.

The measured asymmetry is

$$A^m_{abcd} = \frac{N^{ab}\int \mathrm{d}t\varepsilon\tau L^{cd} - N^{cd}\int \mathrm{d}t\varepsilon\tau L^{ab}}{N^{ab}\int \mathrm{d}t\varepsilon\tau L^{cd}P_BP_T + N^{cd}\int \mathrm{d}t\varepsilon\tau L^{ab}P_BP_T} \tag{2.5.2}$$

In case of charge asymmetries A^m_C we use ± 1 instead of the average beam and target polarization P_B and P_T . It reads

$$A^m_C = \frac{N^+\int \mathrm{d}t\varepsilon\tau L^- - N^-\int \mathrm{d}t\varepsilon\tau L^+}{N^+\int \mathrm{d}t\varepsilon\tau L^- + N^-\int \mathrm{d}t\varepsilon\tau L^+} \tag{2.5.3}$$

To control the luminosity integrals the numbers of DVCS events are usually normalized to DIS numbers with same polarization as they are assumed to be symmetric according to beam charge and polarization.

$$A^m_{abcd} = \frac{\frac{N^{ab}_{DVCS}}{N^{cd}_{DIS}} - \frac{N^{cd}_{DVCS}}{N^{ab}_{DIS}}}{\frac{N^{ab}_{DVCS}}{N^{cd}_{DIS}}P_BP_T + \frac{N^{cd}_{DVCS}}{N^{ab}_{DIS}}P_BP_T} \tag{2.5.4}$$

2.6 PROPERTIES OF THE GPDS

In the flowing, features of the GPDs will be discussed that connect them to already known physical quantities like form factors or charge. Figure 2.2.1 on page 9 shows the connections between the different objects starting with the GTMDs, defined by the FOURIER transform of the WIGNER distributions down to the particle charge. Both GPDs and TMDs can give a tomographic picture of the nucleon in space or momentum as for example described in [63] .

2.6.1 *Useful GPD relations*

In [54] Ji explains that the MELLIN moments [34] of GPD $H^q(x,\xi,t)$ and $E^q(x,\xi,t)$ can be written as

$$\int_{-1}^{1} \mathrm{d}x(x^n - 1)H^q(x,\xi,t) = H_n(x,t) \tag{2.6.1}$$

$$\int_{-1}^{1} \mathrm{d}x(x^n - 1)E^q(x,\xi,t) = E_n(x,t) \tag{2.6.2}$$

The first moments can be identified as the DIRAC and PAULI form factor

$$\int_{-1}^{1} \mathrm{d}x H^q(x,\xi,t) = F_1^q(t) \tag{2.6.3}$$

$$\int_{-1}^{1} \mathrm{d}x E^q(x,\xi,t) = F_2^q(t) \tag{2.6.4}$$

and the axial and pseudo scalar form factor are

$$\int_{-1}^{1} \mathrm{d}x \tilde{H}^q(x,\xi,t) = g_A^q(t) \tag{2.6.5}$$

$$\int_{-1}^{1} \mathrm{d}x \tilde{E}^q(x,\xi,t) = g_P^q(t) \tag{2.6.6}$$

in their expression the ξ dependence drops out [53] .
Another important relation is the quark charge and helicity distribution.
$H_q(x,0,0) = q(x)$ and $E_q(x,0,0) = \Delta q(x)$ for $q = u,d,s$
and also he states his famous sum rule

$$J_q = \frac{1}{2}\int \mathrm{d}x x \left[H_q(x,0,0) + E_q(x,0,0)\right] \tag{2.6.7}$$

relating the GPDs to the proton's spin contribution carried by each quark type, including not only the quark's spin but also its orbital momentum contribution.
They fulfill the symmetry relation in ξ:

$$\begin{aligned} H_q(x,t,\xi) &= H_q(x,t,-\xi) \\ \tilde{H}_q(x,t,\xi) &= \tilde{H}_q(x,t,-\xi) \\ E_q(x,t,\xi) &= E_q(x,t,-\xi) \\ \tilde{E}_q(x,t,\xi) &= \tilde{E}_q(x,t,-\xi) \end{aligned}$$

2.6.2 *Reconstruction of CFFs from measurement*

The access to GPDs from experimental data is not possible in a direct way as only a ξ and t dependence is measurable for cross sections or asymmetries in DVCS as the GPDs enter as a convolution in x.

In 1999 M. Vanderhaeghen, P.A.M. Guichon and M. Guidal published their fitting model for GPDs known as the VGG [76] model. In this publication they give a first estimation on the leading order amplitude of the exclusive photon reactions (BH/DVCS) using a double distribution formalism as a basis.

3

EXPERIMENTS IN THE PAST AND FUTURE

This chapter summarizes former and future experiments about nucleon structure setting focus to the aspect of asymmetry measurement and the HERMES experiment.

3.1 THE HERMES EXPERIMENT

HERMES was one of the pioneering experiments on the nucleon structure sector. It was originally designed to resolve the spin crises [2] by measuring the spin contribution of different quark flavors. The detector started its first measurements in 1995. Since 2000 HERMES was used as a asymmetry machine. The possibility to vary charge and spin of both target and beam allowed reconstruction of a variety of different measurements Table 3.1.1 on page 27. First the measurements where done using only forward spectrometer information and later with the kinetically complete event reconstruction from the recoil detector.

3.1.1 *Asymmetries from meson production*

The asymmetry measurements on meson production began in 2000 [4] with the single spin asymmetry of semi inclusive charged pion production. Varying the spin of the hydrogen target the asymmetry was extracted comparing the cross-sections of the pion production and the dependence on the azimuthal angle ϕ of the pion relative to the lepton scattering plane was inspected. This was the first of a number of asymmetry measurements with mesons varying the target spin and beam spin and charge. In 2001 an analysis of neutral pions was added and compared with the results for the charged pions. [5]

In the next step the hydrogen target was replaced by a deuterium target to measure the single spin asymmetries changing the longitudinal target polarization on pions of every charge and positively charged kaons [6].

Then the measurement of double spin asymmetries on semi inclusive pion and kaon production began with the longitudinally polarized positron beam and a longitudinally polarized deuterium target [7]. In the same publication five helicity distributions for different quark flavors (u_v, d_v, u_s, d_s, s_s) where extracted. These studies were extended to using the hydrogen target for the helicity studies[8].

In 2008 the single spin asymmetry and the azimuthal distribution of $\pi^+\pi^-$ pairs in semi inclusive deep inelastic scattering were measured with the transversely polarized hydrogen target[11].

In [14] meson single-spin asymmetries where connected to the TMDs, [16] showed a $\sin(\phi + \phi_s)$ modulation for charged pions and positive kaons.

Exclusive measurements on π^+ mesons where studied in [18] extracting the transverse target polarization asymmetries as a function of the MANDELSTAM variable t, the BJORKEN scaling variable x_B, and the virtuality Q^2 of the exchanged photon.

The two latest HERMES publications came out in 2013. [24] measured the azimuthal distributions of $\pi^{\pm}, \pi^0$ and $K^{\pm}$ in a four dimensional kinematic space. [25] calculated the multiplicities normalized to the DIS yield for different hadron types.

3.1.2 *Asymmetries DVCS/BH*

All asymmetries extracted on DVCS at HERMES by now are displayed in Figure 3.1.3 on page 30. Since 2007 the HERMES Collaboration is working on the extraction of a huge set of asymmetries varying beam and target polarization and beam spin.

The first publication on this topic was [9] where the beam charge asymmetry A_C was extracted from data taken with an unpolarized hydrogen target. [12] repeated the A_C extraction with higher precision and showed the first result on A_{UT} (unpolarized beam, transversely polarized target).

Later a combined A_C and A_{LU} fit was performed on the complete data set from 1996 to 2005 also taking into account the contribution of the interference term to the BH/DVCS cross-section separately [15]. A_{LU} and A_C where extracted with an unpolarized hydrogen and deuterium target in [17]. After the longitudinally polarized target was available the extraction of A_{LL} and A_{UL} was possible [21], in [20] the combined fit on A_C, A_{LL} and A_{UL} at once was performed with a hydrogen and in [19] with a deuterium target. This means they where measured using a multi parameter fit extracting all amplitudes of the asymmetries at once.

The two newest hermes DVCS publications are the most important for this thesis as in [22] the first asymmetry results with kinetically complete event reconstruction is published and in [21] the latest and most complete measurement of A_C reconstructed in a combined fit with A_{UL} on the unresolved data sample. The results of these experiments will be directly compared with the results of this work.

Figure 3.1.1 on page 28 shows the beam spin asymmetry extracted with the kinetically complete event reconstruction compared to the unresolved (without recoil information) data sample and a reference sample, which is a subset of the unresolved data sample where the recoiling proton is calculated to be in the recoil detector acceptance and have the same kinematic conditions. Figure 3.1.2 on page 29 shows the beam charge asymmetry extracted from the unresolved data sample from the accumulated HERMES data taken with the hydrogen target from 1996-2005 and 2006-2007. The data sample from 2006-2007 is the most important one for the comparison as the kinetically complete event reconstruction only is available for this time period.

3.1.3 *Other HERMES studies*

Other HERMES studies that have been performed are for example a measurement of the spin structure functions of proton and deuteron $g_1^p(x, Q^2)$ and $g_1^d(x, Q^2)$ and the calculation of the neutron spin structure function of the g_1^n[10], the determination of the momentum and helicity density distributions of the strange quark sea in the nucleon [13] and azimuthal distribution studies and asymmetry measurements on unidentified charged hadrons [17] and [24].

beam charge	beam polarization	target polarization	target	measurement type	mesons	publication
+	unpolarized	longitudinal	hydrogen	semi inclusive	π^+	[4]
+	unpolarized	longitudinal	hydrogen	semi inclusive	$\pi^\pm, \pi^0$	[5]
+	longitudinal	longitudinal	deuterium	semi inclusive	$\pi^\pm, \pi^0, K^+$	[6]
+	longitudinal	longitudinal	hydrogen	semi inclusive	$\pi^\pm, \pi^0, K^+$	[8]
+/-	unpolarized	transversal	hydrogen	semi inclusive	$\pi^+\pi^-$ pairs	[11]
+/-	unpolarized	transversal	hydrogen	semi inclusive	$\pi^\pm, \pi^0, K^\pm$	[14]
+/-	unpolarized	transversal	hydrogen	semi inclusive	$\pi^\pm, \pi^0, K^\pm$	[16]
+/-	unpolarized	transversal	hydrogen	exclusive	π^+	[18]
+/-	unpolarized	transversal	hydrogen	semi inclusive	$\pi^\pm, \pi^0, K^\pm$	[24]
+/-	unpolarized	transversal	hydrogen	semi inclusive	$\pi^\pm, \pi^0, K^\pm$	[25]

Table 3.1.1: Overview over HERMES meson production measurements since 2000

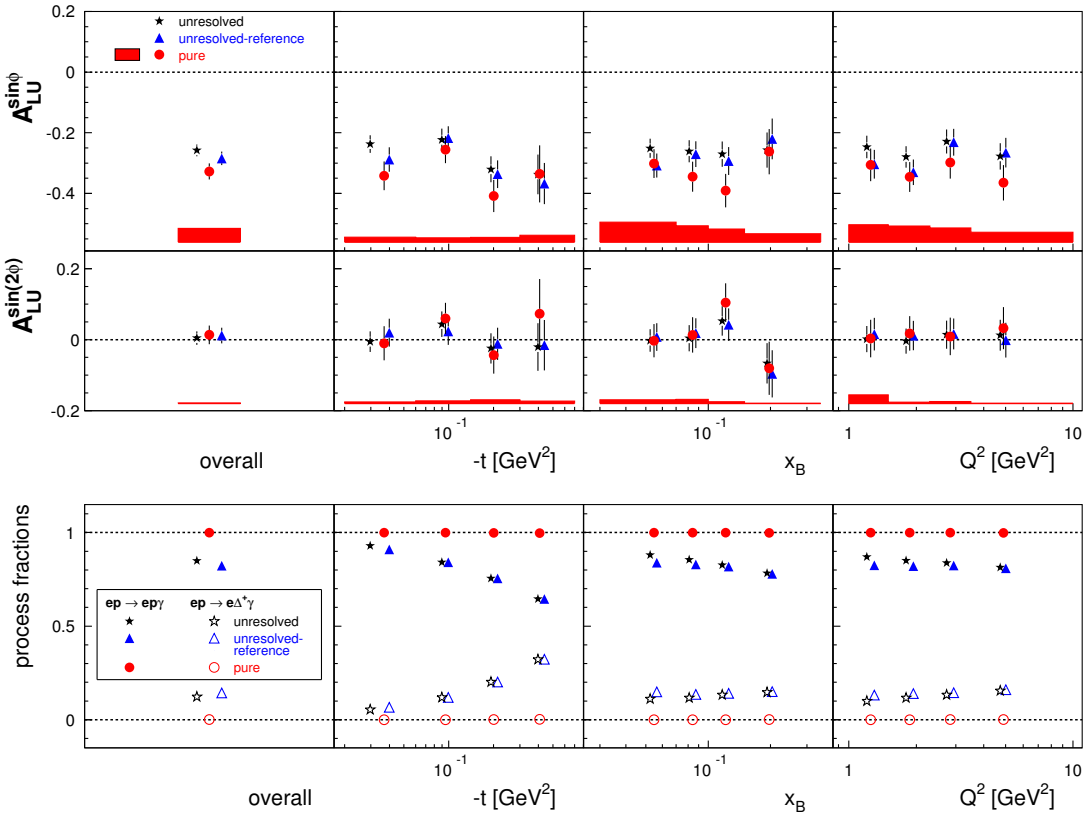

Figure 3.1.1: [23] Amplitudes of single-charge beam-helicity asymmetry in DVCS shown in projections of $-t$, x_B, and Q^2. Statistical uncertainties are shown by error bars. The bands represent the systematic uncertainties of the amplitudes extracted from the pure sample. A separate scale uncertainty arising from the measurement of the beam polarization amounts to 1.96%. Shown are amplitudes extracted from a) the pure sample (red circles, shown at their kinematic values) b) the unresolved-reference sample (blue triangles, shifted to the right for better visibility) c) the unresolved sample (black stars, shifted to the left for better visibility). See 4.4.1 for the exact definition of the data samples. The latter two sets of amplitudes are subject to an average contribution of 14% and 12%, respectively, for associated processes. The lowest plot row shows fractional contributions from the BH process (closed symbols) and associated BH process (open symbols) for each of the exclusive samples.

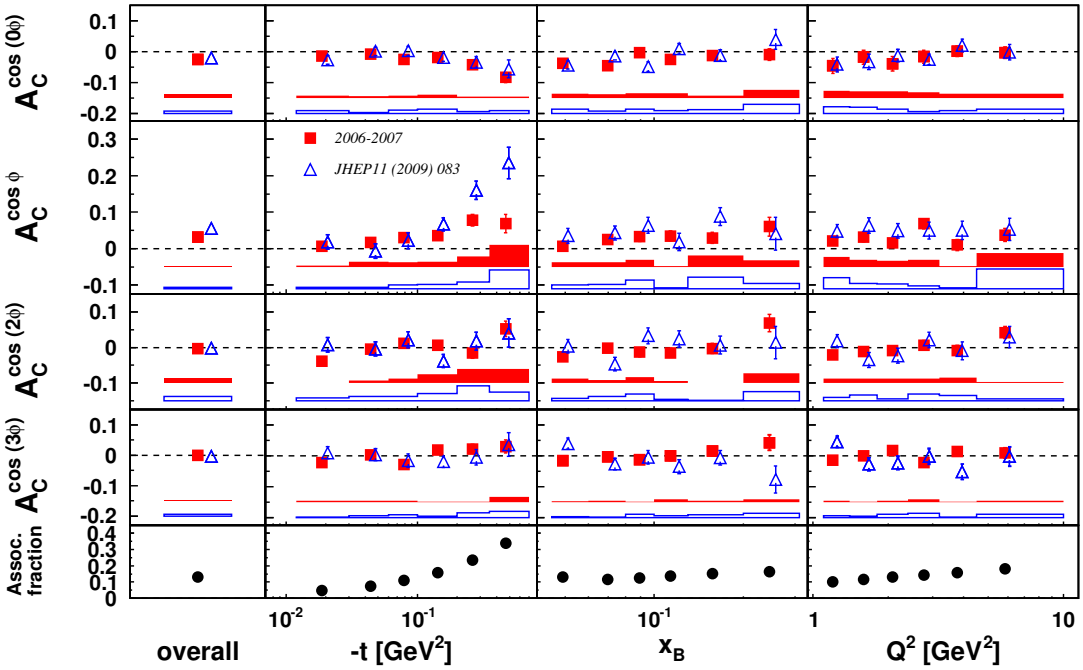

Figure 3.1.2: [21] Beam-charge asymmetry amplitudes extracted separately from the unpolarized 1996-2005 (open triangles) and 2006-2007 (filled squares) hydrogen data. The error bars represent the statistical uncertainties. The error bands represent the systematic uncertainties. The simulated fractional contribution from associated production to the yield in each kinematic bin is shown in the bottom row.

3.2 FORMER EXPERIMENTS

Besides of the HERMES experiment there have been several DVCS experiments in the last decade, especially at DESY and JLAB. Most of them measured beam spin asymmetries on DVCS and DVMP (Deep Virtual Meson Production) but also beam charge asymmetry information was extracted.

The other DVCS experiments at DESY where H1 and ZEUS. They measured the total cross-section of DVCS [72] that can be found in Figure 3.2.1 on page 30 as a function of on the kinematic variables W and Q^2. Also the $t = (p - p')$ dependence is discussed and the beam charge asymmetry is estimated in this publication.

At Jefferson Lab at the CLAS experiment measurements in the kinematic region of $Q^2 = 1 - 4.5GeV^2$, $x_B = 0.1 - 0.5$, and $\mid t \mid$ up to $2GeV^2$ where performed. DVCS cross-sections and beam spin asymmetries where extracted as displayed in Figure 3.2.3 on page 31 and Figure 3.2.4 on page 32.

See also [66],[55],[67],[49] , [69] and [35] for other CLAS results.

3.3 FUTURE EXPERIMENTS

Several experiments are planned for the future to investigate the structure of the nucleon through the access to GPDs. Especially the LHC and JLab are planning a DVCS measurement program. Also at FAIR in Darmstadt/Germany will be studies on GPD related processes.

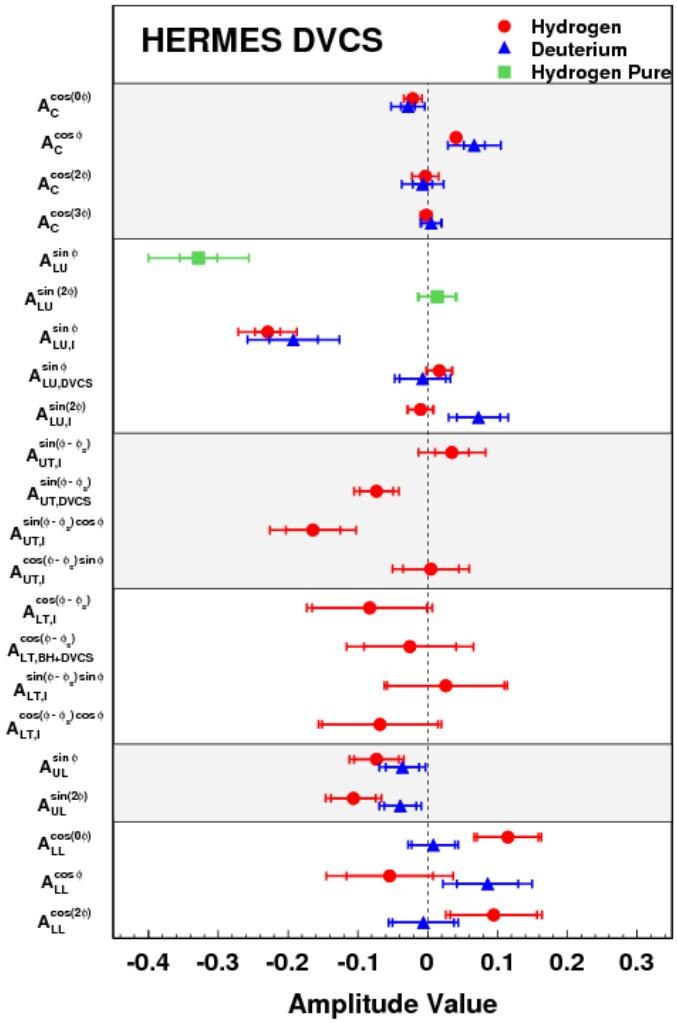

Figure 3.1.3: [3] Overview of all DVCS azimuthal asymmetry amplitudes measured at HERMES with proton and deuterium targets, given at the average kinematics. The inner error bar represents the statistical uncertainty; the full bar the quadratic sum of statistical and systematic uncertainties. Red and blue dots represent the reconstruction using forward spectrometer information only, green dots mean the kinetically complete event reconstruction with the recoil detector.

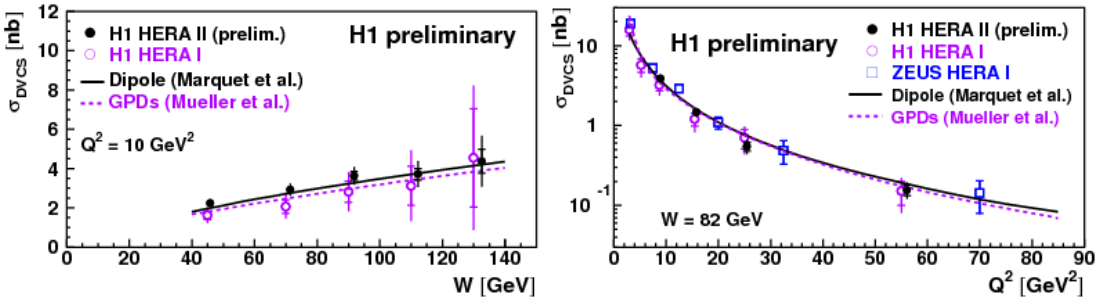

Figure 3.2.1: [72] DVCS cross-section for the full HERA data as a function of W and Q^2 .

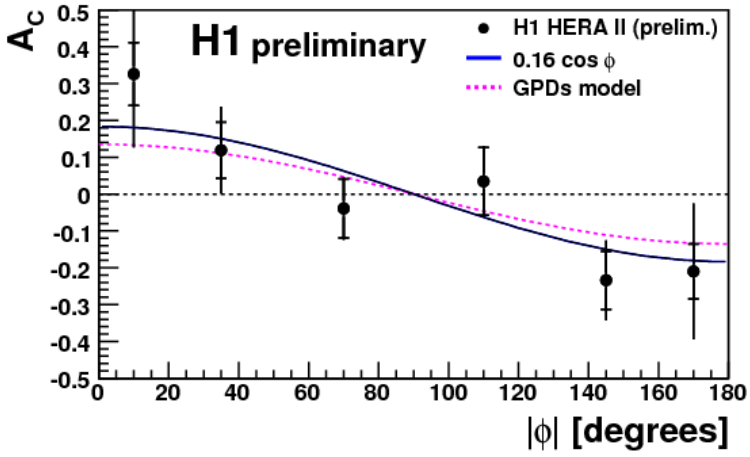

Figure 3.2.2: [72] Beam charge asymmetry as a function of ϕ measured by H1.

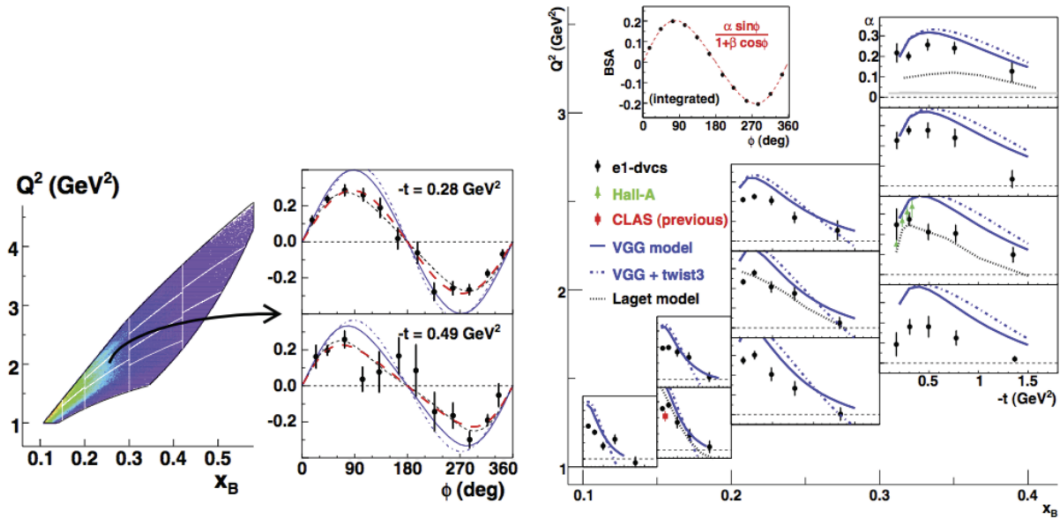

Figure 3.2.3: [60] Beam-spin asymmetry from the CLAS DVCS experiment. Left: the $(x^B\ ,\ Q^2)$ acceptance. Middle: beam-spin asymmetry data at two values of t within one $Q^2\ ,\ x^B$ bin on the left. Right: Extracted beam-spin asymmetry as a function of $-t$ for all kinematic bins. The curves are explained in the graph.

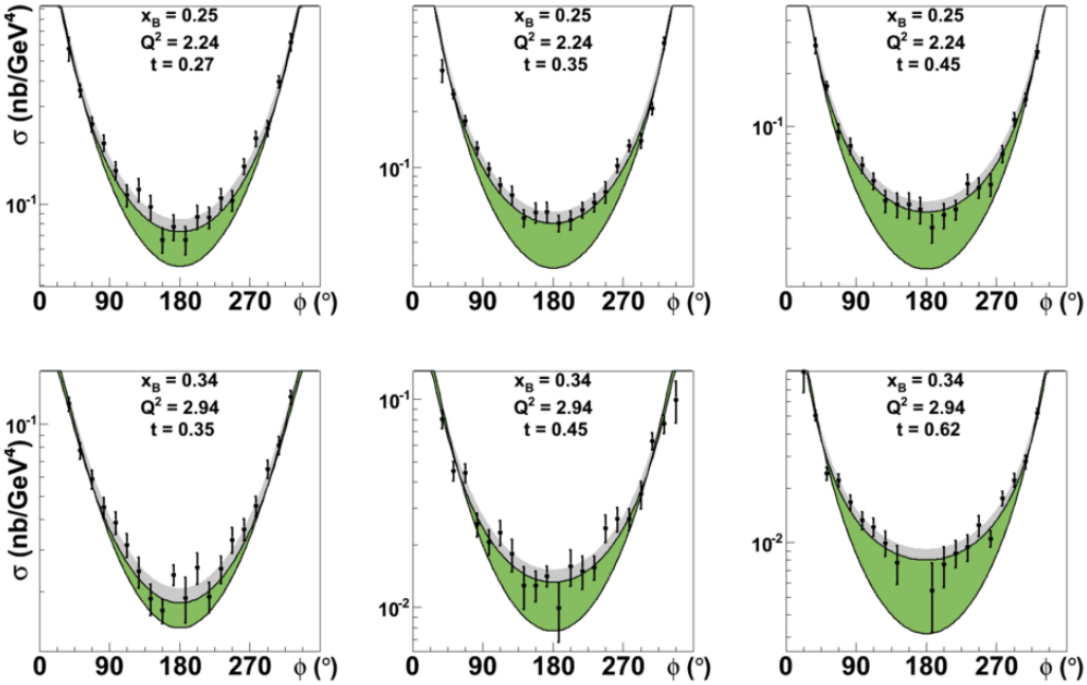

Figure 3.2.4: [60] DVCS cross-section as a function of the angle ϕ for a few of the many kinematic bins in Q^2, x_B and t. The lower black curves are due to a pure BH calculation, the upper curves are fits to the data - the differences are represented in green. Top:$Q^2 = 2.24GeV^2$, $x_B = 0.25$, $-t = 0.27$, 0.35 and $0.45GeV^2$. Bottom: $Q^2 = 2.94GeV^2$, $x_B = 0.34$, $-t = 0.35$, 0.45 and $0.62GeV^2$.

In his talk [67] Kousznetsov explains which measurements are possible at CERN with the COMPASS detector. Depending on the x value the BH/DVCS channel is not dominated by the BH but by DVCS events at COMPASS kinematics, so that the cross-section can be measured directly. Figure 3.3.1 on page 33 displays the comparison between BH and DVCS cross-sections for different x_B values. For $x_B = 0.1$ the BH is suppressed by about one magnitude. For $x_B = 0.01$ the DVCS amplitude is accessible through the interference term ob BH and DVCS and the low x_B regions can be used as a reference yield. [41] also proposes to measure the beam spin and beam charge asymmetries with the muon beam in the same experiment.

JLab is working on the CLAS12 upgrade which is supposed to measure DVCS events at a higher energy than was possible with CLAS. In [45] Eloudrhiri explains the changes to the 6GeV experiment CLAS6 as a higher luminosity and improved PID. A prediction is made for A_{UT}, the spin asymmetry measured with an unpolarized beam and polarized target as can be seen in Figure 3.3.2 on page 33. More information on CLAS12 can be obtained from [55] and [44].

In Darmstadt at the PANDA experiment on the nascent collider FAIR the cross channels $pp \to \gamma\gamma$ to DVCS and $pp \to \gamma M$ to DVMP are suggested for GPD access [64].

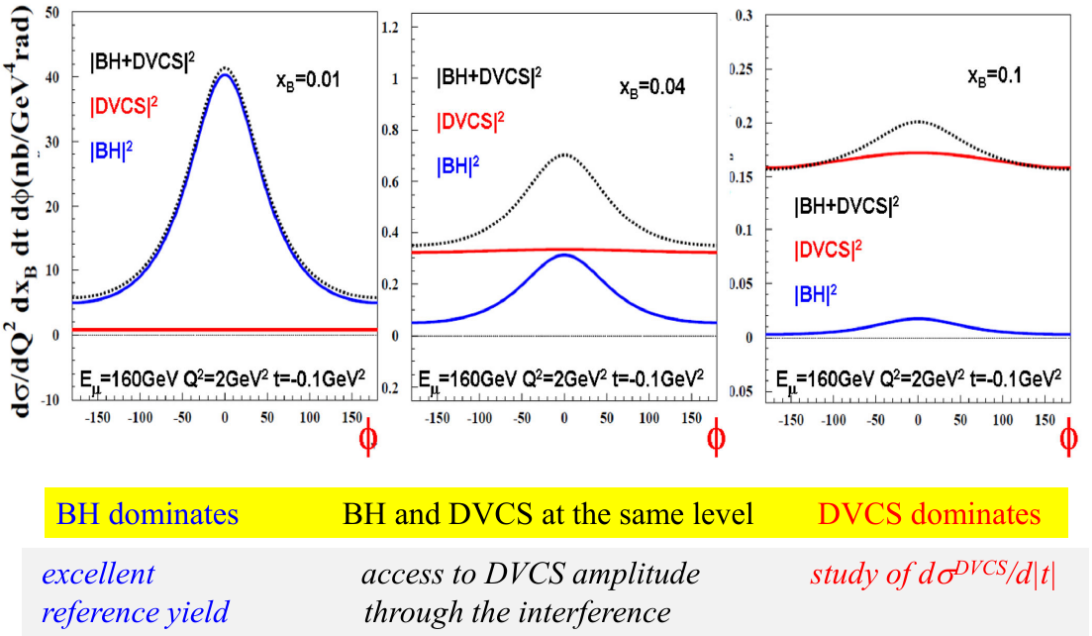

Figure 3.3.1: [67] Comparison between BH and DVCS cross-section at COMPASS kinematics for different x values. BH dominates at $x_B = 0.1$

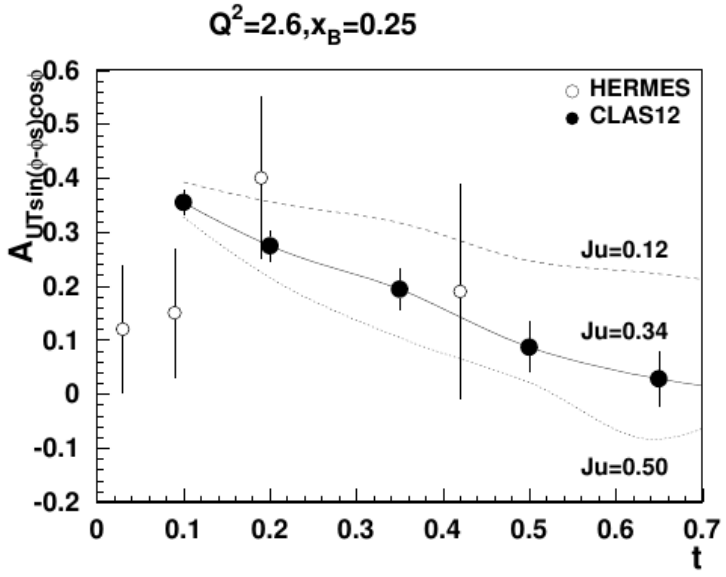

Figure 3.3.2: [45] Projected transverse target asymmetry A_{UT} for DVCS production off protons at 11 GeV beam energy. The curves represent different assumptions on the u-quark contributions to $J(t) = \int_{-1}^{1} \mathrm{d}x\, x\,[H(x,\xi,t) + E(x,\xi,t)]$.

Part II

TECHNICAL IMPLEMENTATION

4

THE HERMES SETUP

4.1 HERA@DESY

The HERA-ring (Hadron-Elektron-Ring-Anlage) was the main accelerator and storage ring at DESY (Deutsches Elektron SYnchrotron) from 1991 to 2007. It had a total length of 6.3 km. In this ring electrons or positrons were accelerated to an energy of about 27.6 GeV and protons to about 920 GeV in separate, parallel pipes. The HERA ring was appointed with 4 interaction points where the experiments H1, ZEUS, HERA-B and HERMES were placed.

HERA was served from a cascade of pre-accelerators. The negatively charged hydrogen atoms (H^-) were sampled from hydrogen gas and after a pre-acceleration injected into the linear accelerator LINAC III which brought them to an energy of 50 MeV. After this they were stripped to plain protons and injected into the DESY III accelerator gaining there 7.5 more GeV. Then they entered the last pre-accelerator. PETRA brought the protons to the injection energy of 40GeV before they finally entered the HERA-ring.

The electrons on the other hand where accelerated to 450 MeV with LINAC II and piped into DESY II where they gained about 9 GeV and at last added 3 more GeV in PETRA II before being piped into HERA. A schematic picture of the HERA ring can be found in 4.1.2 (left).

4.1.1 *Polarization of the lepton beam*

One very convenient fact about HERA is that the lepton beam is self polarizing in a circular accelerator. Synchrotron radiation flips the spin of stored electrons in the bending dipole's magnetic field. The spin aligns parallel or anti-parallel to the magnetic field depending on the beam charge with the transverse magnetic field. By this effect, known as SOKOLOV-TERNOV-effect the polarization builds up gradually. Every time a lepton emits synchrotron radiation its spin flips. Parallel aligned electrons and anti parallel aligned positrons have a higher emission probability than the other charge spin combinations, so electrons align parallel and positrons anti parallel by the time.

4.1.2 *Polarimetry at HERA*

4.1.2.1 *LPOL*

The measurement of the longitudinal beam polarization is performed using a Nd:YAG (neodymium-doped yttrium aluminum garnet) laser with a pulse length of 3 ns and 100 mJ at a frequency of 100 Hz. The initiallylinearly polarized light is converted by a POCKLES cell [1] to right and leftcircularly polarized light. This light hits the electron beam in the tunnel and compton back scattered photons are collected in the

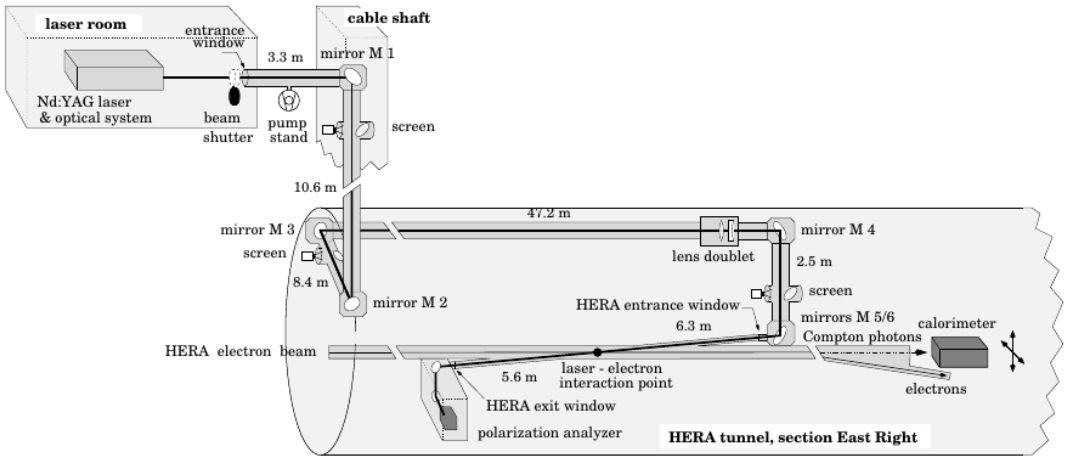

Figure 4.1.1: [30]Layout of the Longitudinal Polarimeter in the HERA East section.

calorimeter. From the laser polarization the beam polarization is reconstructed. A schematic picture of the LPOL detector is displayed in 4.1.1

4.1.2.2 *TPOL*

The traversal polarimeter uses a 10 W continuous waveform Ar-ion laser. After passing the Pockels cell the circularly polarized light is changed in helicity with a frequency of 90 Hz. After every measurement cycle of 40 seconds the the laser is turned off for another 20 seconds to take a background measurement.

4.1.3 *Spin rotators for HERMES*

The Ternov-Sokolov effect polarizes the electron beam in transversal direction. HERMES used a longitudinally polarized beam for a lot of different measurements. For this reason before and after the HERMES interaction region HERA was charged with spin rotators in 1993/1994.

At HERA so called mini-rotators [39] work with a principle similar to from the Siberian Snake. They allowed to adjust [36] "either sign of electron helicity in the longitudinal spin state".

4.2 HERMES@HERA

The acronym HERMES means HERA MEasurement of Spin. The measurement of the nucleon's spin structure is one of the main purposes HERMES was built for. This happens through DIS as discribed in Figure 2.4.3 on page 15 .

HERMES was located in the east hall at the HERA-ring and took its first data in May 1995. It was concepted as a fixed target experiment, therefore most scattering products are expected in forward direction. Until 2005 the detector was a forward angle instrument only and it was upgraded with the recoil detector in 2006 to complete the acceptance and allow a kinematically complete event reconstruction.

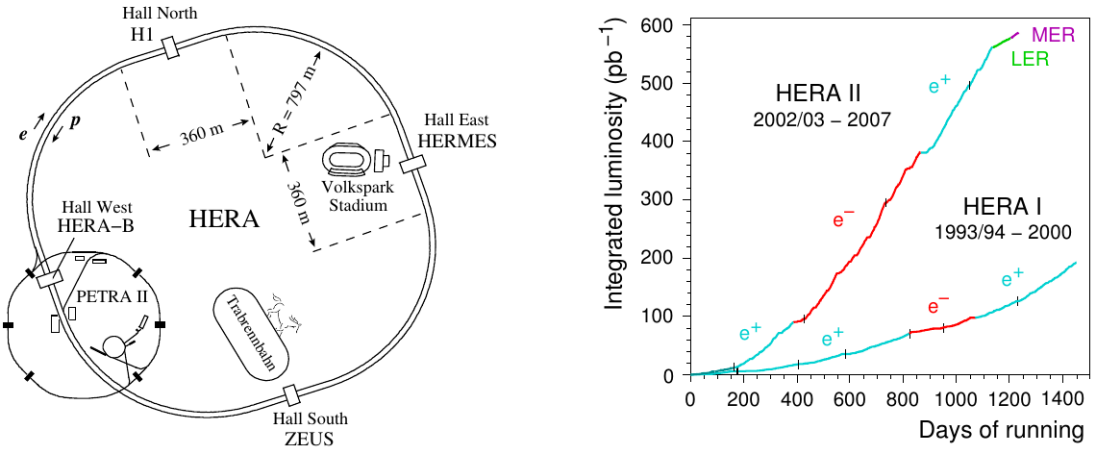

Figure 4.1.2: [36]The HERA accelerator complex (left) and the integrated luminosity at HERA I and HERA II (right). Labels LER and MER: Low and Middle (proton) Energy Runs, black marks: approximate change of year.

4.2.0.1 *Fixed target cell*

HERMES is a fixed target experiment, that only uses the HERA lepton beam while the proton beam is piped through the detector without interaction. It provides its own gas target which is fed into the storage cell from a polarized or unpolarized source. During the HERMES data taking several different target gases where used: H_2, D_2, ^3He, N_2. This data analysis only uses data taken with an unpolarized hydrogen target. Therefor the further explanations will focus on this setup.

As displayed in 4.2.1 the target gas was propagated into the T-shaped tube where the atoms were stored in the vicinity of the lepton beam. In the storage cell the density of the target gas was improved by two magnitudes compared to a free atomic beam. The target cell was open for the gas to leak out and be pumped away. A smoothing of the gas transition to the beam pipe to avoid heating and improve emittance of the beam was reached by a setup of thin perforated tubes called "wake field suppressor" before and after the storage cell. After the installation of the recoil detector the target cell was placed inside it.

4.2.1 *The Forward spectrometer*

4.2.1.1 *The magnetic spectrometer*

The forward spectrometer is symmetric according to its upper and lower part. Initially build with a vertex chamber (VC) and a Cherencov counter it was upgraded with the DVC (Drift Vakuum Chamber) and the by the RICH (Ring Imaging CHerenkov detector) instead. Figure 4.2.2 on page 40 shows the final constellation as was used in the very end of the HERMES live time after the recoil spectrometer was mounted in 2005/2006.

The luminosity monitor is based on the elastic scattering of the target shell inside its $NaBi(W0_4)_2$ (NBW) Cherenkov-cristals. Depending on the lepton beam charge the Bhabha scattering $e^+e^- \rightarrow e^+e^-$ and the $e^+e^- \rightarrow \gamma\gamma$ annihilation in the positron case or the Møller scattering $e^-e^- \rightarrow e^-e^-$ for the electron beam is investigated.

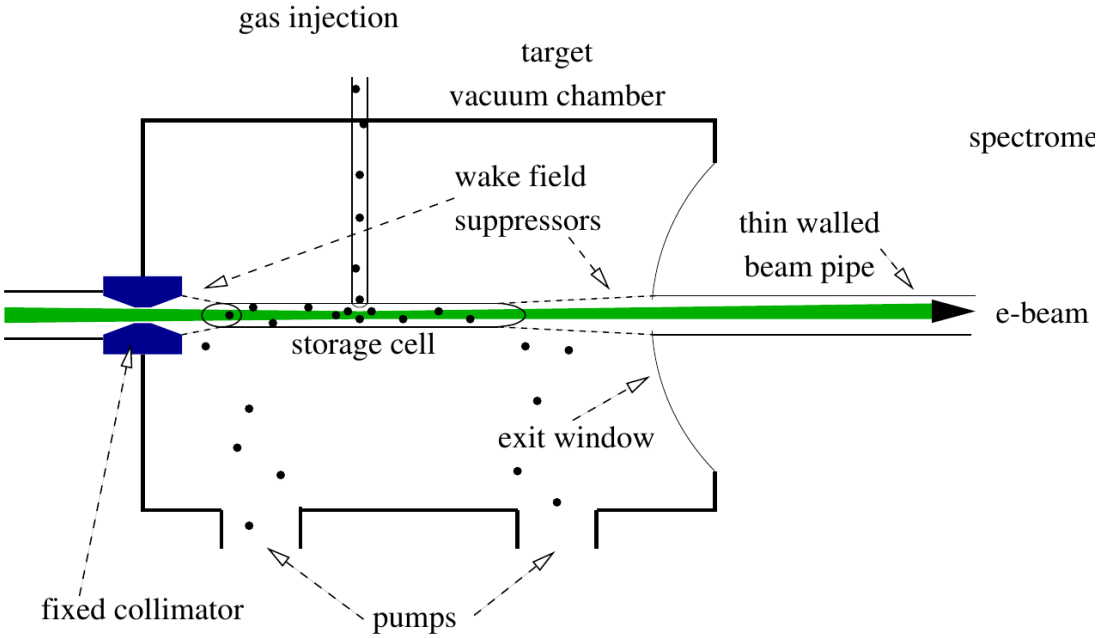

Figure 4.2.1: [2]Schematic of the target region.

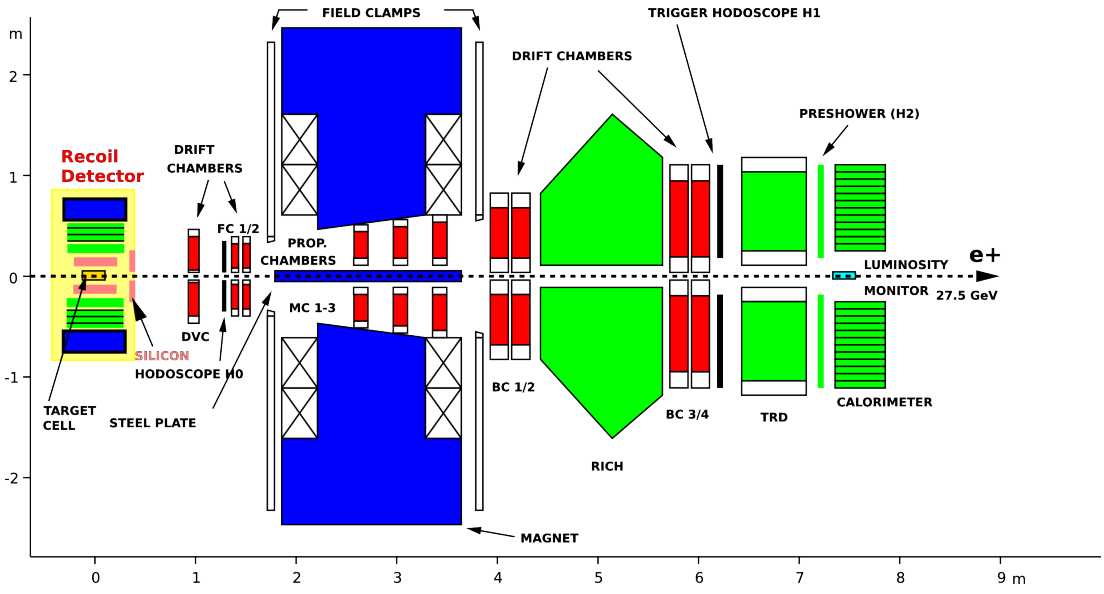

Figure 4.2.2: Schematic side view of the HERMES spectrometer.[2] The lepton beam enters from the left and hits the gas target in the target cell (yellow) inside the recoil detector. The tracking system is colored in red. It consists of DVC, FC, MC and BC. The PID system consisting of RICH, TRD, hodoscope preshower detector and calorimeter is colored in green. The luminosity monitor in light blue can be found after the preshower (H2) at the end of the spectrometer. The yellow underlayed part is the recoil detector added in 2006.

4.2.1.2 *Tracking system*

The tacking system of the forward spectrometer consists of a detector set to measure the momentum polar ϕ and and azimuthal θ angle of incoming particles. The momentum measurement is performed by two sets of drift chambers (BC 1-2 and BC 3-4) behind the magnet. Information from the drift chambers DVC and FC 1,2 allow to determine the angular track coordinates as they are mounted in fron of the spectrometer magnet. For low momentum particles that do not reach the BC inside the magnet three proportional chambers MC 1-3 add more space points to the tracking system and allow to measure tracks that are to short to cross the magnet.

4.2.1.3 *PID system*

The four components of the HERMES forward PID system are a 1) threshold Cherencov, 2) a system of two lead glass hodoskopes, one of which is used as a preshower detector (H2) by adding two radiation lengths of lead to one of the detector plates, 3) a transition radiation detector (TRD) and 4) a scintillator calorimeter at the very end of the detector setup.

4.2.2 *The HERMES recoil detector*

4.2.2.1 *Silicon strip detector*

The silicon strip detector (SSD) consists of 16 vacuum embedded sensors aligned in 2 layers around the target cell. It was used for the particle tracking and energy measurement giving up to two inner space points to a recoiling particle track. Low energy particles, mostly pions, are completely stopped in the SSD. In the beginning of 2006 the SSD was damaged by the deflected lepton beam and unmounted for some time. It provides two of four space points for the recoil tracking system.

4.2.2.2 *Scintillating-fiber tracker*

The other two space points are added by the scintillating-fiber tracker (SFT). This detector part was originally developed at the JLU Gießen. It was placed outside the vacuum chamber in two barrel like layers. Each layer is built of four sublayers of scintillating fibers, two layers where the fibers are parallel to the beam direction and two under an angle of 10°. So a crossing particle can be detected precisely on an intercept point of the parallel and the aslant layers. A schematic picture is displayed in 4.2.3. The detector is build of a number of 4992 scintillating fibers and read out by 64-channel multi-anode PMTs (Photo Multiplier Tubes). A photograph of the yet unmounted detector can be seen in 4.2.4 .

4.2.2.3 *Photon detector*

The third recoil sub detector is the proton detector (PD). Its purpose is the detection of decay photons from neutral particle decays. It completes the RD by the sensitivity for neutral particles.

Consisting of three concentric alternating layered barrels of tungsten radiator and scintillating plastic strips the PD works as an electromagnetic calorimeter.

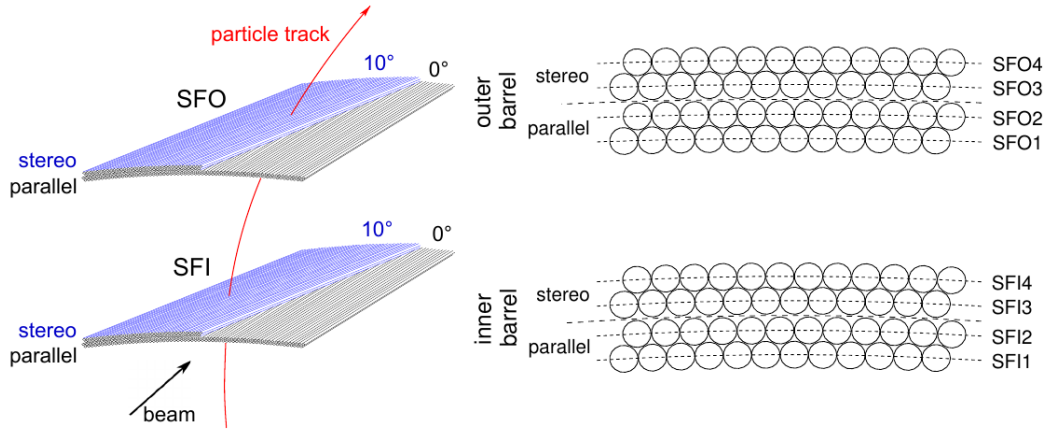

Figure 4.2.3: [46] Schematic view of the scintillating-fiber-tracker (SFT) barrel configuration (left) and the arrangement of fibers in the layers (right).

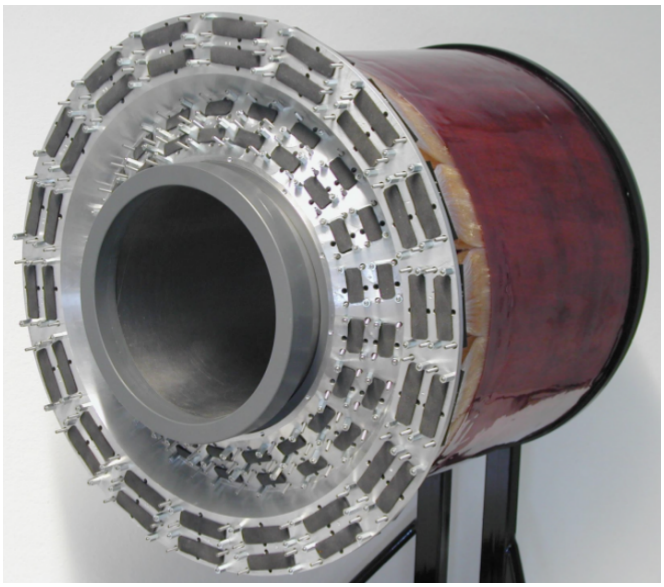

Figure 4.2.4: [46] Picture of the assembled SFT mounted over a mockup scattering chamber.

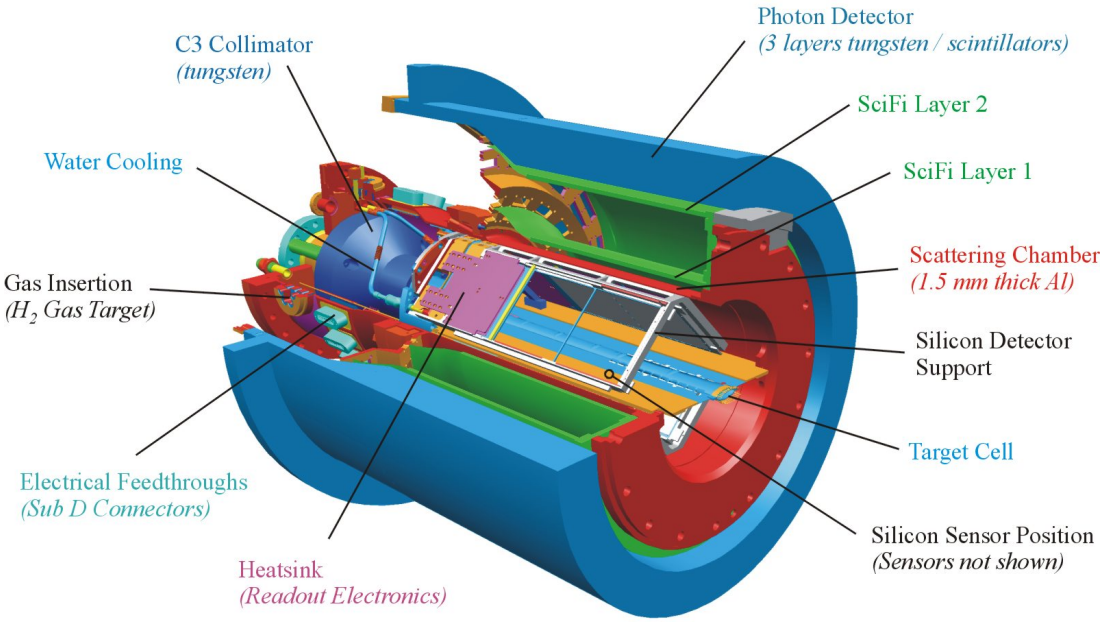

Figure 4.2.5: CAD picture of the HERMES recoil detector

4.3 DATA SELECTION

In this subsection the HERMES data selection mechanisms are introduced. After an overview of the HERMES data storage the data selection criteria for DIS and DVCS events are explained for the different data samples that are relevant to this study.

4.3.1 *The HERMES DAQ*

The acronym DAQ means Data AcQuisition. It is split into a fast (physics data) and a slow (environmental and detector status data) separate read out data flow.

Every triggered event is stored in the fast control and every ten seconds additional information like the accumulated luminosity and trigger dead time is included in the event stream. Every ten second period is called a *burst*, listed in a separate burst list. The slow control data is coded in the so called BadBit which codes different data quality parameter so that every analysis can choose bursts depending on its standards. For example studies that use the forward detector only can ignore the bits that indicate problems in the recoil detector. The data of every burst is spitted in files of 560 MB size, called runs summarizing several events.

4.3.2 *Storage of HERMES data*

Raw data is decoded and the track reconstruction using the later explained HRC or HTC is performed. It takes into account a certain detector calibration depending on the time period of the data taking. The tracking information is stored including the slow control information as HRC and PID information (Figure 4.3.1 on page 45). The HERMES data used for this analysis is organized in so called uDST (micro Data Summary Tape). Micro refers to the small file size. At this stage reconstructed tracks, slow control information and PID information can be accessed.

4.3.2.1 *HRC*

The HRC (HERMES ReConstruction) is the traditional tracking method in HERMES. It collects the hit positions in the wire chambers of the forward spectrometer and fits straight tracking lines to these points separately for the region before and after the spectrometer magnet.. The front and back parts are field free regions without any bending in the trajectories of charged particles. In the region between these two parts the strong vertical magnetic field bends the particle tracks. HRC connects the path in the front part and the back part complementing the unknown part by projecting pairs of front and back tracks into the magnet. By using a lookup table that assigns the momentum to a certain bending and momentum the charge of a particle is determined.

A full track that has been reconstructed from the front and back part is called a long track in difference to the short track that ends in one of the magnet chambers and does not reach the front spectrometer part.

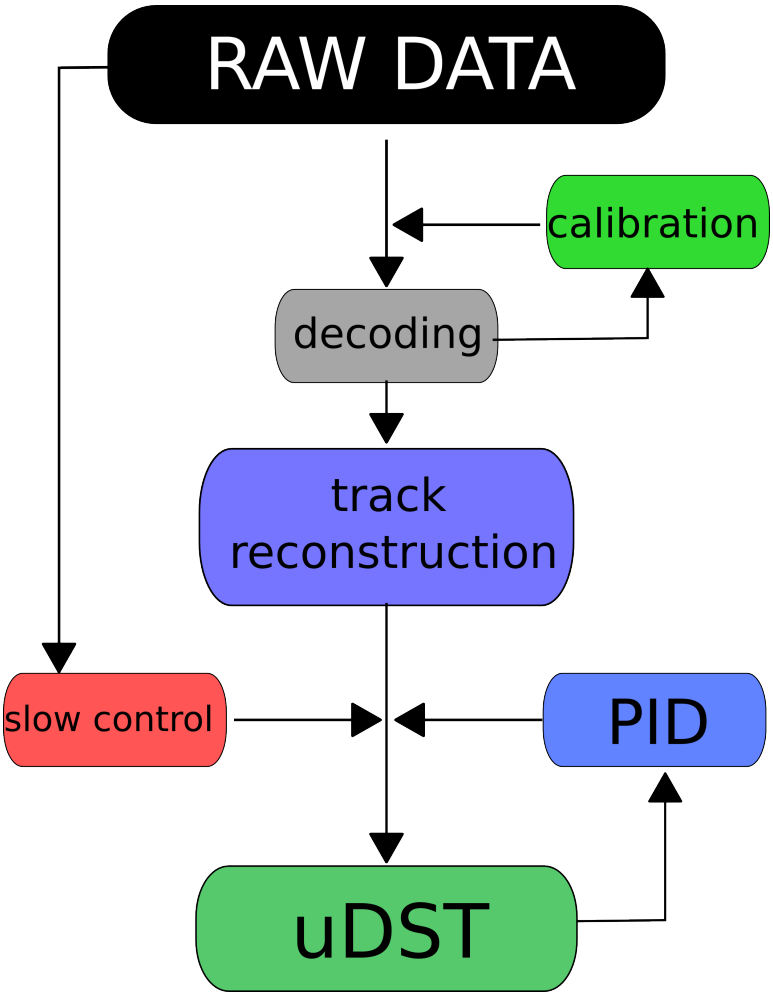

Figure 4.3.1: uDST production. Raw data is decoded and passes the track reconstruction. It is stored in uDSTs along with PID and slow control information.

4.3.2.2 *HTC*

The method [57] that is used for the track reconstruction in the forward spectrometer is called HTC (HERMES Tracking Code). It uses a so called KALMANN filter [56] to model a parametrization of every track at any z position taking into account the target's magnetic field, the particle passage through the detector materials and the beam position.

HTC uses the parametrized HRC tracks and takes into account misalignment, beam tracks and magnetic fields of the target, recoil and spectrometer magnet [73].

4.4 SELECTION OF A DVCS/BH DATA SAMPLE

According to the DAQ levels, the selection of DVCS/BH data works in several steps. Good bursts are selected on general data quality criteria. Then a list of DIS events is selected. Depending on which kind of data sample is being processed other criteria on DVCS/BH candidates are applied. In forward detector analysis DVCS/BH events are selected, in recoil detector analysis multiple recoil tracks can be candidates for each event.

4.4.1 *Burst and event selection*

The following cuts and requirements are applied on the bursts for the data selection:

GENERAL REQUIREMENTS.

- Front Spectrometer tracking: Only 1 forward spectrometer track in the event is required using HTC information.
- Correct z position of the calorimeter hit for photons to avoid misalignment.

BURST LEVEL / DATA QUALITY. As basis for the set of cuts on burst level, [79]is used.

- The beam polarization measurement is valid and within the range accurately recorded by the beam polarimeter: $0 < |p| < 1$.
- The event was not rejected because of malfunctions in the beam polarimeter.
- The TRD was operational in both (top and bottom) parts of the spectrometer.
- The energy of the beam is higher than 27 GeV.
- No unphysical values for the luminosity are accepted.
- A BadBit (4.4.1) cut is applied depending on what type of analysis is going to be used.

The BadBit

The BadBit patterns are hexadecimal transformations of binary numbers, the so called bits that might be set or not set. The encoding is explained in Table 4.4.1 on page 47. Each bit stands for one data quality requirement.

Three different sets of BadBit patterns are applied for three different data samples depending on which part of HERMES is required to be functioning: forward spectrometer (FS), SFT, and SSD:

0X741E1BDC is used to select data with working SFT. Compared to the report of 2011 the bit that indicates a malfunctioning SSD is turned off to conserve the data in the "bad recoil period", the time before run 27934. It requires FS and SFT.

0X7C1E1BDC is used for the cross check with published recoil analysis as it only accepts bursts from the time period when the Recoil detector was fully operational. It is the same BadBit that is used in the publications. It excludes all electron bursts and can therefore not be used for BCA extraction. It requires FS, SFT and SSD.

0X501E1BDC is used for the cross check with published forward analysis. It has no requirements to the recoil detector. Neither the magnet nor SFT or SSD need to be marked working. It requires FS only.

bad bit	meaning	0x7c1e1bdc	0x741e1bdc	0x501e1bdc
2,3,4	dead time, burst length, beam current	x	x	x
6,7,8,9	burst properties	x	x	x
11	recoil magnet OFF	x	x	-
12	no logbook data quality	x	x	x
17,18	dead blocks in calo, H2/Lumi	x	x	x
19,20	bad TRD, HV trips, FC, BC	x	x	x
26	Bad NOVC tracking efficiency	x	x	-
27	bad recoil SSD	x	-	-
28	beam pol measurement to long ago	x	x	x
29	bad Recoil SFT	x	x	-
30	dead time	x	x	x

Table 4.4.1: The different BadBit patterns used in this report. 0x741e1bdc requires "good" FS and SFT. It is used for the main analysis of the pure data sample with method 3. 0x7c1e1bdc requires functioning FS, SFT, and SSD. It is used for BSA cross checks from the pure data sample with method 7. 0x501e1bdc requires FS only. It is used for cross checks with published unresolved data analysis.

EVENT LEVEL DIS CUTS. The following cuts [79] are additionally applied to select Deep Inelastic Scattering (DIS) events. There are fiducial volume cuts to remove events that originate from unphysical regions of the HERMES setup or are detected in positions that contradict the detector geometry.

- Trigger-21 has verified a physics event has occurred in the detector.
- There is one lepton considered to be the "leading" scattered lepton. This means that it is the lepton with the highest energy. It has to fulfill the following criteria or the DIS event is discarded:
  - The scattered lepton has the same charge as the beam lepton.
  - The scattered lepton is a long track 4.3.2.1.
  - Its energy is smaller than the beam energy.
  - A scattered lepton is identified in the recoil PID
- From the leading lepton the following kinematic variables are calculated and cuts applied:
  - $Q^2 > 1\ GeV^2$: for the reaction to be deeply inelastic to ensure the applicability of factorization.
  - $W^2 > 9\ GeV^2$: to exclude resonances.
  - $\nu < 22$ **GeV** corresponding to a $y \lesssim 0.80$ cut to avoid large radiative corrections that will be necessary at high y values.
- Vertex cut on the DIS lepton. Vertex z-position between 5 cm and 20 cm.

- Fiducial volume cuts (FVC) on the DIS lepton to assure an optimal calorimeter performance:

Position	x	y
Front field clamp	$\|x\| < 31$ cm	-
Septum plate	-	$\|y\| > 7$ cm
Rear field clamp (front track)	-	$\|y\| < 54$ cm
Rear field clamp (long track)	$\|x\| \leq 100$ cm	$\|y\| \leq 54$ cm
Calorimeter	$\|x\| \leq 175$ cm	30 cm $\leq \|y\| \leq 108$ cm

EVENT LEVEL EXCLUSIVE CUTS. After the selection of the DIS sample, several event samples are selected. The events are tagged as described in the following.

- SPE: Single Photon Events sample.
  - Exactly one track that is a DIS lepton.
  - Exactly one untracked cluster in the calorimeter for the photon.
  - Cuts on the photon:
    - Calorimeter positions of the untracked cluster: $|x| < 175cm$, $33cm < |y| < 105cm$, in order to make sure the shower is completely contained in the calorimeter.
    - Energy depositions in the calorimeter and the preshower detector. $E_{calo} > 5GeV$, $E_{preshower} > 0.001GeV$ (cutting away non-showering photons)
    - To have a clearly defined kinematic region for the analysis: $Q^2 < 10GeV^2$, $0.03 < x_B < 0.35$. Constrained MANDELSTAM variable: $t_c = t|_{M_x=M} < 0.7GeV^2$ in order to reject non-exclusive background.
    - Angle between virtual and real photons: $5mrad < \theta_{\gamma\gamma^*} < 45mrad$. The lower cut was determined in order to ensure that the azimuthal angle ϕ is properly defined within the spectrometer resolution and cuts away very few events from the data sample. The upper limit on the cut is a result of Monte Carlo studies, which determined that the data set above this upper value is dominated by background from the BETHE-HEITLER process with a resonant state of the proton, and from semi-inclusive meson production.
- Traditional DVCS event sample (unresolved data sample).
  - SPE events inside the exclusive window of the squared missing mass. The determination of the missing mass window is explained in Sec. 3.4.1.
  - Used for the traditional analysis and for cross checks with publications.
- Pure sample: DVCS event sample with the proton remaining in the ground state.
  - All SPE events for which there is a Recoil track reconstructed, and the Recoil track in the event with the smallest $\chi^2_{elastic}$ fulfills $\chi^2_{elastic}$ **< 13.7** (See section 2.4 for definition of $\chi^2_{elastic}$).

  - The cuts on the constrained Mandelstam variable t_c and the angle between the real and virtual photons $\theta_{\gamma\gamma^*}$, both of which improve the exclusivity of the sample, were by intention not modified with respect to the traditional DVCS analysis, for the reason of being better able to compare the results of the new with the old analysis.
  - Still, because the missing mass cut is not applied on the pure elastic sample, it is not a true subset of the traditional DVCS sample.
  - Used for every analysis including the recoil detector

- Reference sample: DVCS event from the traditional sample where the recoiling proton is calculated to be in the acceptance of the recoil detector.
  - Subset of the traditional DVCS event sample.
  - Adapts the unresolved data sample to the kinematics of the pure sample.
  - Used as a reference when the unresolved and pure data sample are compared to match effects of the detector kinematics correctly.

4.5 TRACK FITTING FOR RECOIL TRACKS

Tracking parameters and hypotheses.

Tracking is performed independently for the forward spectrometer (HRC for track finding and HTC for track fitting) and for the recoil detector (XTC). The track parameters are stored in separate uDST-tables, where they are linked to the common quantities on event and burst level. As shown in the cross-section sketch of Figure 4.5.1 on page 50, there are four tracking layers (2×SSD and 2×SFT) providing space points (SP) as input to the track finding algorithm. Charged particles with momentum greater than about 125 MeV/c are tracked (threshold to leave a signal in the outer SSD layer). In short, the logic for the track finding is the following:

Possible particle tracks are composed from one space point in each of the four layers giving a four bit pattern as described in Figure 4.5.2 on page 51. For each space point a detector resolution and a momentum is saved. Every track is marked with suiting reconstruction methods explained below. Then a χ^2 fit is performed as following:

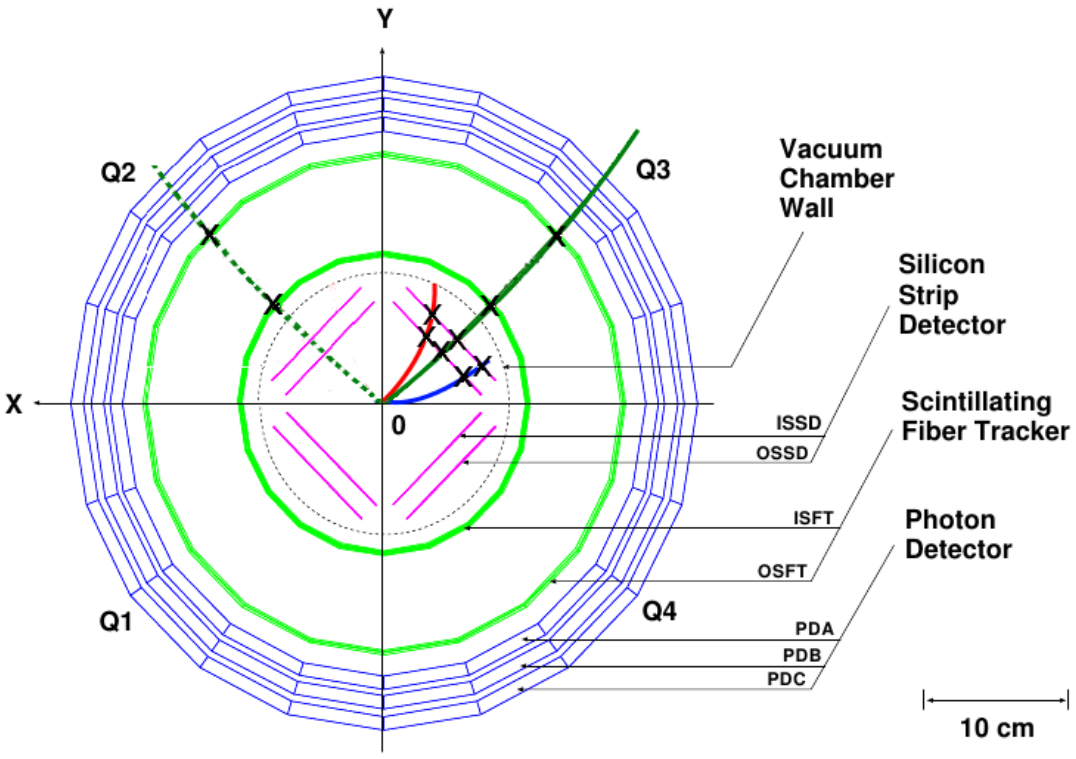

Figure 4.5.1: Recoil detector tracking scheme, cross-section of the detector view. The electron beam is going into the plane (z-direction). The azimuthal ϕ angle is the angle in relation to the negative x-axis. The black crosses mark space points in the available layers. The space point configuration of the solid green track is (1111) , for the blue and red track it is (0011). The dashed green line marks a (1100) track that can only be reconstructed with method 3.

The function to be minimized for a N-space-point-track in case of independent measurement errors and neglecting multiple scattering is [46]

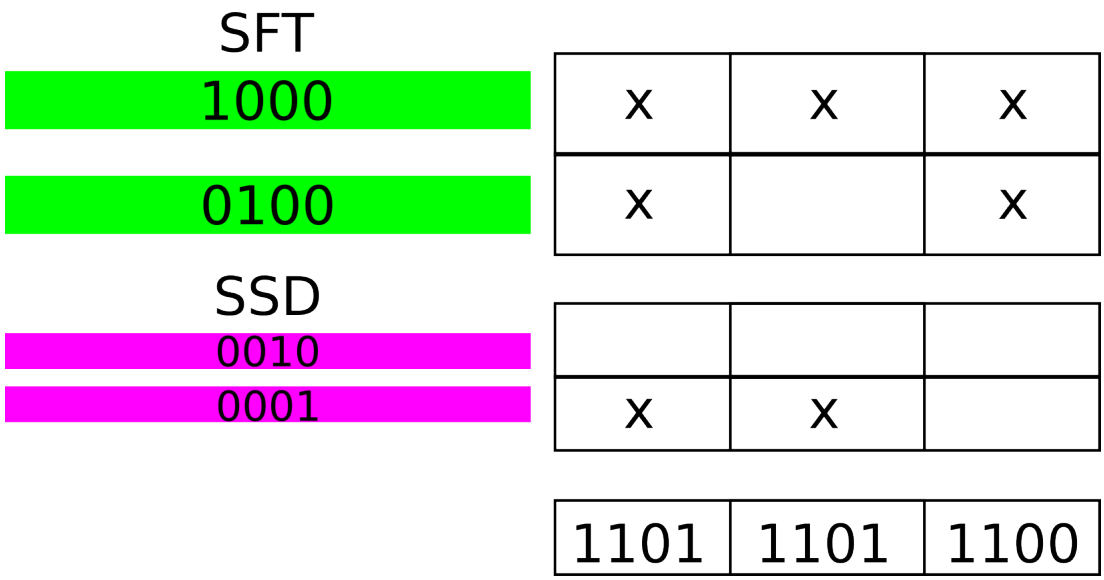

Figure 4.5.2: Space point configuration in SSD and SFT. The two SFT layers match with to the first bins of the binary number, the SSD layers with the last two. A hit (x) sets the according bin to 1. Three examples are displayed in the three raws on the right. The resulting bin pattern is shown at the bottom line of each raw.

$$\chi^2 = \sum_{i=0}^{N-1} \frac{(S_i^{fit}(P) - S_i^{meas})^2}{(\sigma_i^{meas})^2} \tag{4.5.1}$$

S_i^{meas} and σ_i^{meas} are measured coordinates and resolutions.

$S_i^{fit}(P)$ are coordinates to be fitted to the measured coordinates, functions of a kinematic parameter P.

The vertex position is assumed to be equal to the beam position in the xy plane that is determined by a beam-finder code for each run.

The following kinematic parameters are chosen:

$\lambda = 1/p_t = 1/(p \cdot \sin(\theta))$,$\phi_v$ the polar angle, $\cot(\theta_v)$ the azimuthal angle and z_v the z coordinate of the tracks vertex position.

During the minimization of 4.5.1 the coordinates are expressed as following:

$\phi_{\text{det}} = \phi_v - C \cdot R \cdot B \cdot \lambda \cdot \frac{0.3\text{GeV}}{200\text{T cm}}$, $z_{\text{det}} = z_v + R \cdot \cot(\theta_v)$

where C is the particle charge, B is the magnetic field, and R is the distance from a detector layer to the vertex. ϕ_{det} and z_{det} are the detected polar angle and z position.

In order to take multiple scattering into account, equation 4.5.1 can be modified by inclusion of correlation coefficients on the error matrix:

$$\chi^2 = \sum_{i=0}^{N-1} (S_i^{fit}(P) - S_i^{meas}) V_{i,j} (S_i^{fit}(P) - S_i^{meas}) \tag{4.5.2}$$

where V_{ij} are elements of the covariance matrix V. They are determined from Monte Carlo simulation for protons. For pions, multiple scattering can be neglected.

This information and the available analyzing methods are stored in the uDST files and only read out by the analyzers. The two methods relevant to this analysis are the so called method 7 and method 3.

METHOD 7 (M7) First, all tracks with one space point in each sub detector are collected (4-space-point-tracks (1111)). After fitting each track with a circle hypothesis a track is accepted if the χ^2 of the fit is below a threshold of 20. After this the used space points are removed form subsequent track search.

Next, the procedure is repeated with all 3-space-point tracks ((1101), (1110), (1011), (0111)).

Finally the 2-space-point tracks with hits in the inner and outer SSD (0011) are considered. Including those that belong to 3-spacepoint tracks but excluding those that belong to 4-space-point tracks. Here no χ^2-cut is applied. Figure 4.5.2 on page 51 shows the composition of the space-point in the SFT and SSD.

METHOD 3 (M3) Method 3 only considers tracks that have 2 space points in the SFT. Only SFT information is used for the tracking.

2-, 3- and 4-space-point-tracks ((1100), (1101), (1110),(1111)) are treated as (1100) tracks and the fit is only done on the 2 SFT space points.

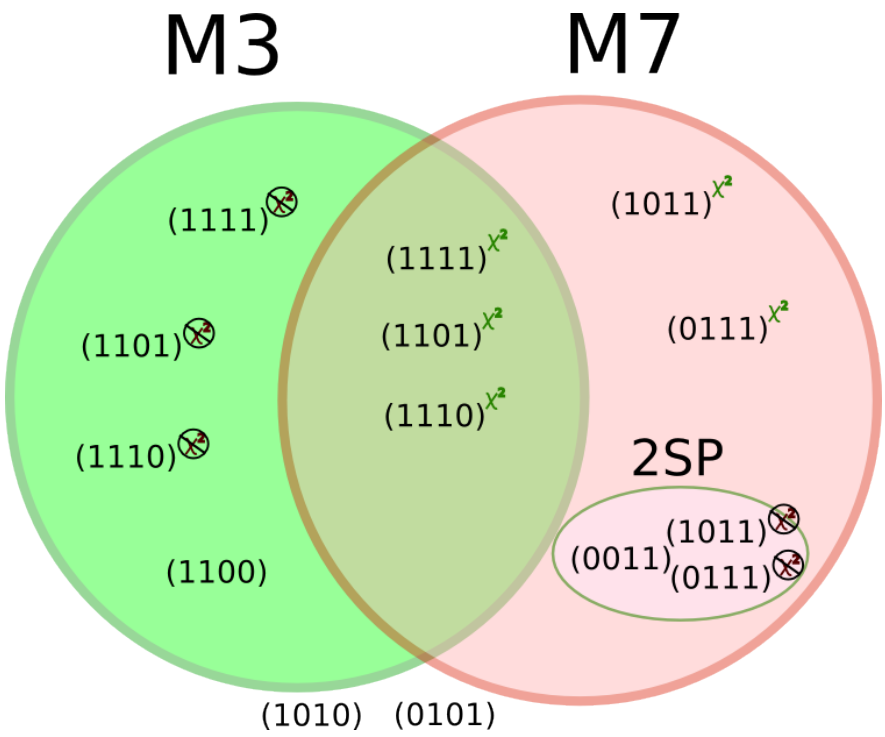

Figure 4.5.3: N-space-point-tracks and Methods. Green χ^2 means that χ^2 is below the threshold, red χ^2 means χ^2 is above a threshold of 20. This χ^2 must not be confused with the χ^2 from kinematic event fitting.

4.5.3 visualizes how which events are fitted by which method.

XTC fits every recoil track using one of the following particle hypotheses:

PROTON. Momentum reconstruction by bending in the magnetic field taking into account energy losses in the whole detector and passive materials assuming the proton mass and using in addition energy deposits in the SSD as fit parameters. To be used if available.

STOPPEDPROTON. Momentum reconstruction by energy deposits in the SSD. To be read if the Proton hypothesis does not exist or if the χ^2 of the fit is >100 (2-5% for M7).

PION. Momentum reconstruction by bending in the magnetic field taking energy losses in the whole detector and passive materials into account assuming the pion mass. Always provided for 3 and 4 space point tracks. To be read if neither Proton or StoppedProton hypothesis exists (<1% for M7).

4.5.1 *Kinematic fitting*

The kinematic event fitting [22] is performed using 9 measured and 9 fitted parameters in the fitting procedure using the recoil detector data of the recoiling on the proton. The quantity

$$\chi^2_{\text{kin}} = \sum_{i=0}^{8} (r_i^{fit} - r_i^{meas})^2 / \sigma_i^2 \tag{4.5.3}$$

is minimized under four constraints f_j from three-momentum conservation and assumed particle masses:

$$f_j(r_0^{fit}, r_1^{fit}, ..., r_8^{fit}) = 0, \quad j = 0, 1, 2, 3 \tag{4.5.4}$$

where r_i^{meas} are measured and r_i^{fit} are fitted kinematic parameters of the positron, photon and the proton candidate and σ_i are the measured uncertainties of these parameters. The minimization is performed using penalty terms:

$$\chi^2_{\text{pen}} = \sum_{i=0}^{8} (r_i^{fit} - r_i^{meas})^2 / \sigma_i^2 + T \cdot \sum_{j=0}^{3} \frac{f_j(r_0^{fit}, r_1^{fit}, ..., r_8^{fit}) f_j(r_0^{fit}, r_1^{fit}, ..., r_8^{fit})^2}{(\sigma_j^f)^2} \tag{4.5.5}$$

where σ_i^f are the propagated uncertainties of f_j and T is a constant number. For sufficiently large T (the value of 10^8 is chosen for this analysis), the constraints are automatically satisfied after convergence of the minimization procedure.

The nine parameters used here are for the scattered electron:

$$\begin{aligned} r_0 &= \tan(p_{x0}/p_{z0}) \\ r_1 &= \tan(p_{y0}/p_{z0}) \\ r_2 &= 1/p_0, \end{aligned}$$

for the photon:

$$\begin{aligned} r_3 &= \tan(p_{x1}/p_{z1}) \\ r_4 &= \tan(p_{y1}/p_{z1}) \\ r_5 &= 1/p_1, \end{aligned}$$

and for the proton:

$$
\begin{aligned}
r_6 &= \phi_2 \\
r_7 &= \theta_2 \\
r_8 &= 1/(p_2 \sin\theta_2)
\end{aligned}
$$

After the fit is performed for every track, the track with the best $\chi^2_{kin} < 13.7$ is selected and the fitted parameters give corrected 3-momentum values for the 3 particles. The corrected kinematic values r_0^{fit} are not used in the analysis for the calculation for composed kinematic variables.

Method 7 is good enough to reconstruct the recoiling proton momentum. But for method 3 without SSD information especially for the low momentum protons the resolution is poor. This results in a large σ that lowers the penalty term drastically. For this reason low momentum tracks are preferred by the χ^2_{kin} fit although they are less reliable.

For this reason a σ adjustment was included in the kinematic event fitting for method 3. The resolutions for the fitted variables were set artificially to a constant term for momenta lower than 0.25 GeV. Figure 4.5.4 on page 54 shows the adapted resolution after this correction. The result of this adaption can be found in Figure 4.5.5 on page 64 .

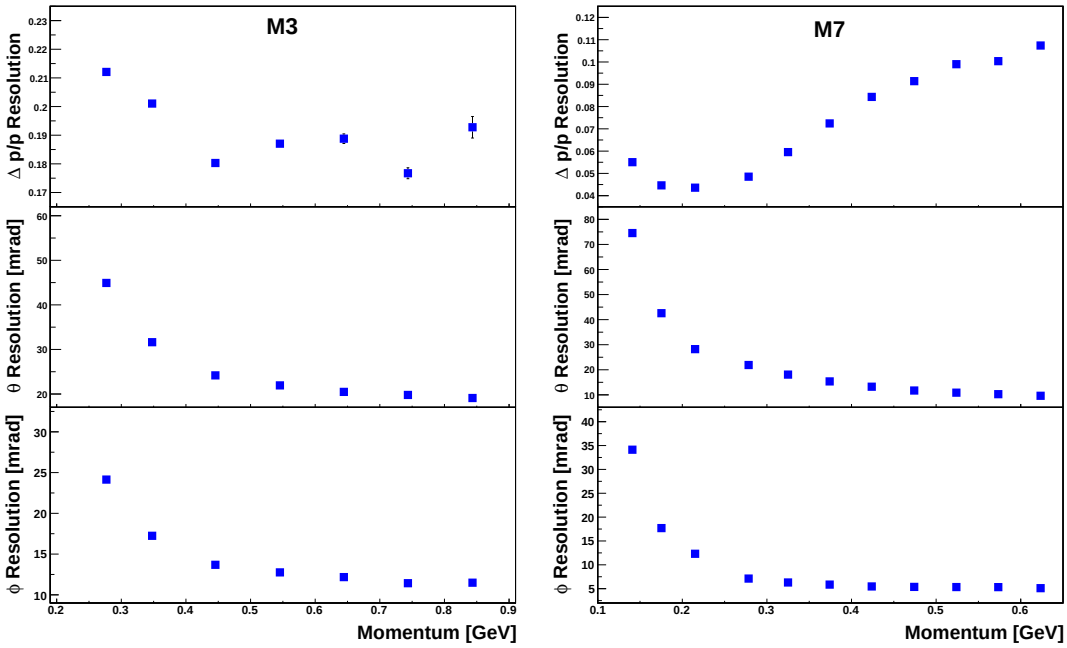

Figure 4.5.4: Resolutions from method 3 tracking (left) and from method 7 (right) for the variables $p, \theta,$ and ϕ.

An equivalent fitting procedure can be performed as well without any information from the recoil detector on only the 6 parameters

$$
\begin{aligned}
r_0 &= \tan(p_{x0}/p_{z0}) \\
r_1 &= \tan(p_{y0}/p_{z0}) \\
r_2 &= 1/p_0
\end{aligned}
$$

$$\begin{aligned} r_3 &= \tan(p_{x1}/p_{z1}) \\ r_4 &= \tan(p_{y1}/p_{z1}) \\ r_5 &= 1/p_1 \end{aligned}$$

Then the momentum of the recoiling proton is calculated from these parameters. This option is used when the reference sample is to be extracted. More about the extraction of the reference sample can be found in Section 4.7.

For method 3 the momentum of the recoiling proton and its angle θ were examined in more detail. Four different momentum sets of momenta p (angles θ) are relevant in this context:

TRUE p_{true}/θ_{true}: true MC values

MEASURED p_{meas}/θ_{meas}: values measured in the recoil detector (MC or real data)

FIT p_{fit}/θ_{fit}: calculated with kinematic fitting , inputing all nine in forward and recoil detector measured particles momenta $p^{part}_{meas}/\theta^{part}_{meas}$ with $part = \{e^{\pm}, \gamma, p\}$ (MC or real data)

EXPECTED p_{exp}/θ_{exp} : calculated from the forward kinematics corrected in a 6 parameter fit as (MC or real data)

$$\begin{aligned} p^{1,p}_{exp} &= -p^{1,e}_{fit_6} - p^{1,\gamma}_{fit_6} \\ p^{2,p}_{exp} &= -p^{2,e}_{fit_6} - p^{2,\gamma}_{fit_6} \\ p^{3,p}_{exp} &= p_{beam} - p^{3,e}_{fit_6} - p^{3,\gamma}_{fit_6} \\ p_{exp} &= \sqrt{(p^{1,p}_{exp})^2 + (p^{2,p}_{exp})^2 + (p^{3,p}_{exp})^2} \\ \theta_{exp} &= \arccos(p^{3,p}_{exp}/p_{exp}) \end{aligned}$$

Figure 4.5.6 on page 65 shows the comparison between p and θ before (p_{meas}/θ_{meas}) and after (p_{fit}/θ_{fit}) kinematic fitting.

4.5.2 *Studies on event reconstruction*

The use of method 3 has some disadvantages compared to method 7. The first one is the inevitable loss of statistics for low momentum protons that can be detected by the SSD but not by the SFT. The second one is the fact that the reconstruction of a track with 2 space points is less exact than a 4-space-point track because fewer constraints are given to adjust the free parameters of the fit. This leads to a shift to higher χ^2_{kin} in the kinematic event fitting (Figure 4.5.7 on page 66) and a worse suppression of the background processes. The background contamination is illustrated in Figure 4.5.10 on page 69. Still, the background suppression is a factor of 10 stronger than in the traditional analysis with an unresolved data sample. Figure 4.5.8 on page 67 displays the M^2_x distribution of MC and pure data. Figure 4.5.9 on page 68 shows the $\theta_{\gamma\gamma*}$ distribution.

4.5.3 *Data quality*

In the first part of 2006 the recoil detector was not completely operational, especially the SSD was unmounted for some time (run 14471-16250 in 2006) and also the SFT showed occasionally a drop of energy deposition. It is possible to find different time periods on the data quality plots [51] some of them show irregularities and some do not. Table 4.5.1 on page 56 shows the statistics in pure and unresolved data samples. As also can be found in the table, there was no data taken with a positively polarized electron beam. Also we find smaller gaps in the method 3 data. It is necessary to decide which time periods need to be excluded from the analysis to make sure that the normalization to the number of DIS events respects the recoil detector gaps.

	time year:run	lepton	pol	DIS unres	DVCS unres	DVCS pure M3	DVCS pure M7
1	06: 700-1040	e^-	↓	6730	13	1	0
2	06: 1040-2154	e^-	↓	373829	587	156	0
3	06: 2155-4630	e^-	↓	34666	55	0	0
4	06: 4631-4795	e^-	↓	74362	115	29	0
5	06: 4796-4875	e^-	↓	0	0	0	0
6	06: 4876-10305	e^-	↓	1861320	2863	740	0
7	06: 10306-10942	e^-	↓	373499	547	163	0
8	06:10942-14470	e^-	↑	2646616	4110	0	0
9	06: 14471-16250	e^+	-	455785	652	146	0
10	06: 16251-44546	e^+	↑	13173629	18892	4010	2902
11	06: 44546-48195	e^+	↓	2091659	3031	730	800
12	07: 3-17980	e^+	↓	7662075	11065	2692	2725
13	07: 17981-24350	e^+	↑	1662533	2544	675	726
14	07: 24351-25200	e^+	↑	374717	561	2	108
15	07: 25201-28500	e^+	↑	1404341	2144	521	530
16	07: 28501-39650	e^+	↑	5138868	7564	1840	1908
17	07: 39650-40515	e^+	↑	102173	178	47	45

Table 4.5.1: Statistics for different time periods in 2006 and 2007 with BadBit 0x741e1bdc

A closer look at the time periods

06: 700-1040, 06: 2155-4630, 06: 4796-4875

An irregularity is seen in the proton energy deposition ΔE of the inner SFT. The mean value of ΔE is lower than in other runs. This time period is excluded from the analysis. All data quality plots are taken from the internal data quality homepage of the HERMES group.

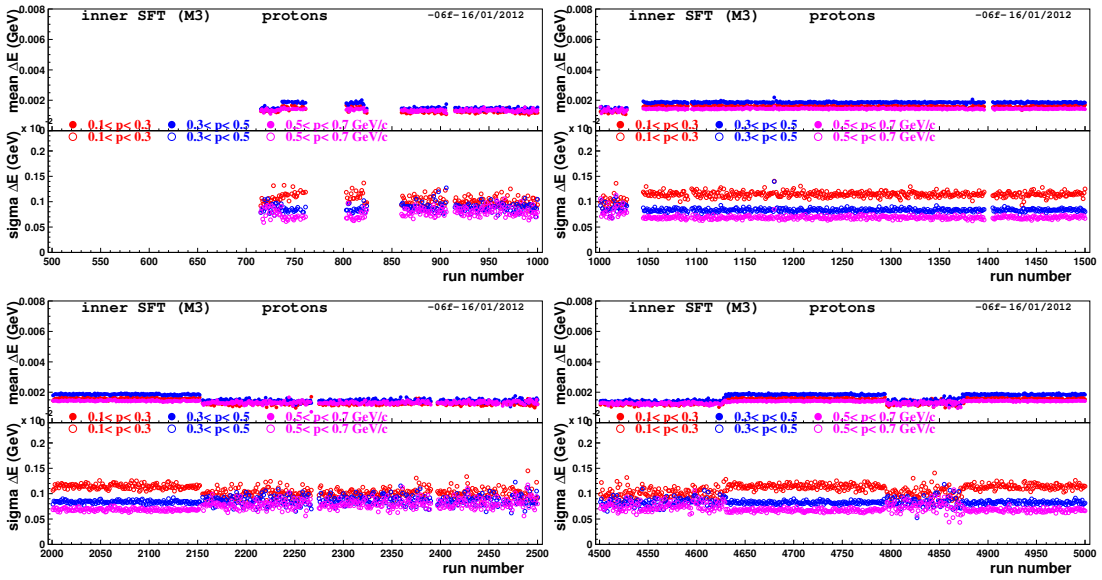

Figure 4.5.11: Energy deposition of space points in the inner SFT used for M3 tracking for 3 different momentum bins ([0.1,0.3], [0.3,0.5], [0.5,0.7]) for the time period 1,3 and 5. The top panel means the energy deposition, the bottom panel the width. Each of the 4 diagrams shows a range of 500 runs.

06: 10306-10942

In this time period the target cell was damaged by the beam. The effect of this accident is not visible in the proton energy deposition but in the energy deposition of pions.

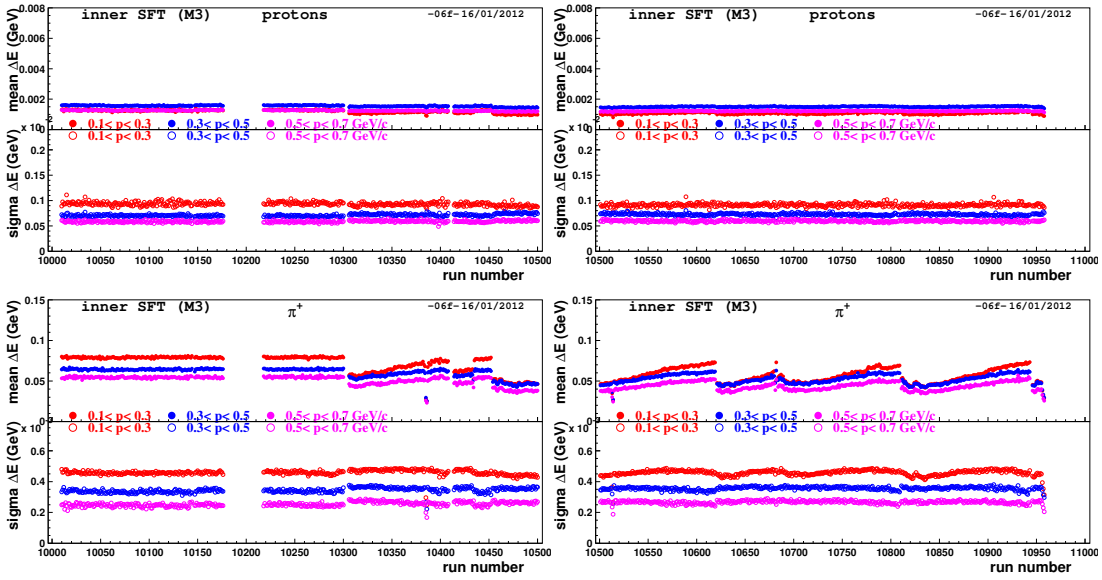

Figure 4.5.12: Energy deposition in the inner SFT for the time period 7. The 2 top pads show energy deposition by protons, the bottom pads show the π^+ energy deposition. Refer to caption of Fig. 4.5.11 for more details.

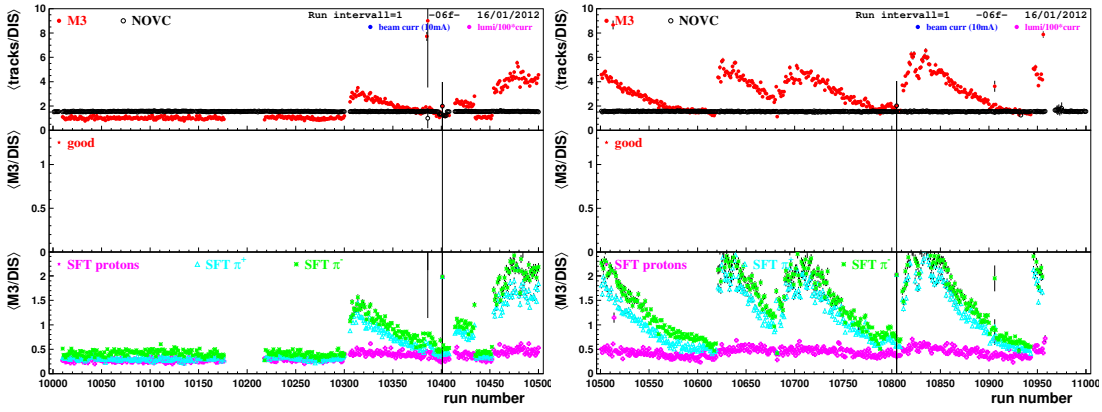

Figure 4.5.13: N_{M3}/N_{DIS} in the time period 7. The top panel shows the ratio of M3 tracks and DIS events compared to the ratio of tracks tracked with the NOVC method. The bottom panel shows how many of the tracks are marked as protons (magenta), π^+ (cyan) or π^- (green)

06:10942-14470

After the accident the recoil detector was partially dismounted. No data is available for method 3 or 7.

06: 14471-16250

After the recoil detector was mounted again HERA was filled with an unpolarized positron beam for some time. For the analysis of BCA this time period not necessarily needs to be excluded. This time period is very short and as it contains only positron events and the statistics are high for the positron data sample. If it is excluded there will be no significant loss in statistics. Therefor it is excluded, too.

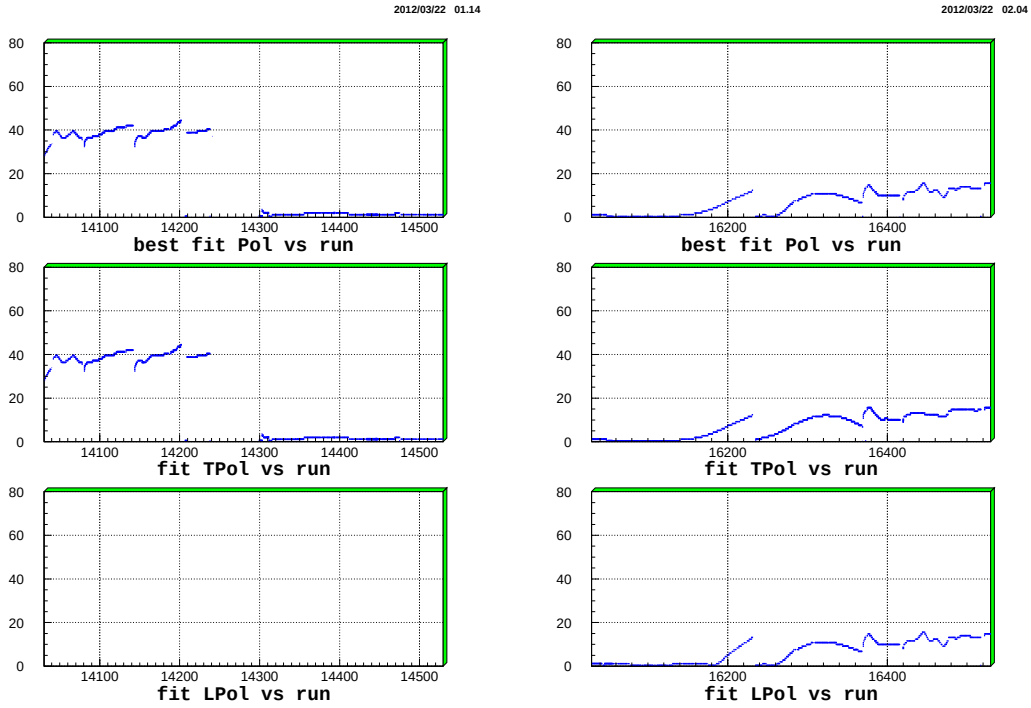

Figure 4.5.14: Beam polarization in the time period 9. The 4 pads show the beam polarization estimated from T Pol and LPol for a range of 500 runs.

07: 17981-24350, 07: 24351-25200, 07: 25201-28500

Here the energy deposition in the recoil detector is following the beam fill (positron beam current). In the time period 07: 24351-25200 additionally the energy deposition of protons drops again like in the beginning of 2006.

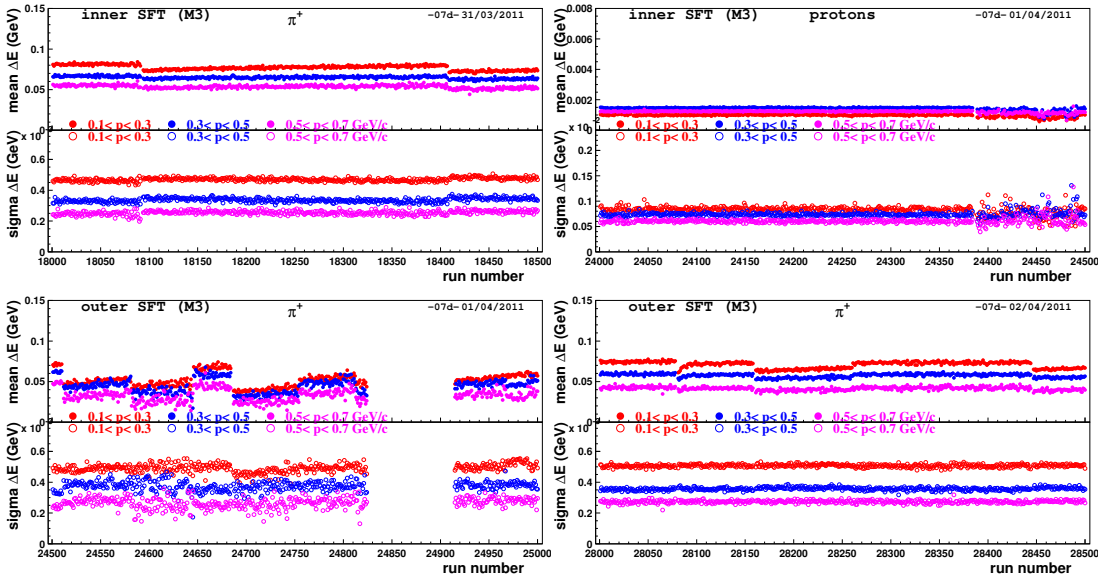

Figure 4.5.15: Energy deposition in the inner SFT for the time periods 13, 14, 15. Refer to caption of Fig. 4.5.11 for more details.

	DIS	DVCS	pure M3	DIS	DVCS	pure M3	0x741e1bdc
	$e^+\uparrow$			$e^+\downarrow$			
2006	13173629	92444	4010	2090559	14902	730	after time period cut
	13173629	92444	4010	2090559	14902	730	all
2007	5137726	36802	1840	7662075	54596	2692	after time period cut
	8947519	64392	3085	7662075	54596	2692	all
	$e^-\uparrow$			$e^-\downarrow$			
2006	0	0	0	2026762	16836	925	after time period cut
	2644172	19008	0	2309161	19762	1089	all
2007	0	0	0	0	0	0	after time period cut
	0	0	0	0	0	0	all

Table 4.5.2: The change in event numbers after the time period cut. The cut especially affected events taken with electron and negative helicity.

07: 39650-40515

The very end of 2007 is excluded too. There are some irregularities in the energy deposition and after run 40000 no data quality plots are available to make sure the runs give reliable information.

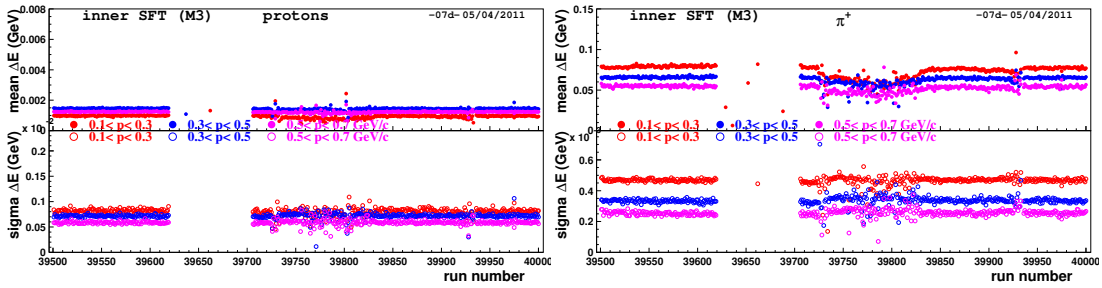

Figure 4.5.16: Energy deposition in the inner SFT for the time period 17. Left for protons, right for π^+. Refer to caption of Fig. 4.5.11 for more details.

Statistics of the data after extra quality cuts

To validate the selected run numbers a cross check on DIS numbers, method 3 tracks and pure method 3 events was performed. The goal to archive a disagreement lower then 1% was met for all samples (see 4.5.3).

0x741e1bdc	DIS	M3 tracks	pure M3
2006	21092095	73909	7179
2007	16614184	72890	6153
2006/2007	37696720	146799	11752
selected time 06	17573349	69532	6850
selected time 07	12799801	54596	4822
selected time	30373150	124128	11672

Table 4.5.3: Overview of all selected event and track numbers.

4.6 THE FOUR QUADRANTS OF THE SFT DETECTOR

In 4.2.2 the geometry of the SFT is described. The 4 parts of the detector have different performances. Especially the so called quadrant 2 covering a region $0 < \phi < \pi/2$ had a malfunction known by the HERMES collaboration. Figure 4.6.1 on page 61 shows the ϕ distribution for method 3. The gap in quadrant 2 leaves almost no electron events for evaluation of this detector part.

In previous analyses where method 7 was used it was never excluded because the SSD information saved a lot of data in quadrant 2 as shown in Figure 4.6.2 on page 62 but will be in this analysis.

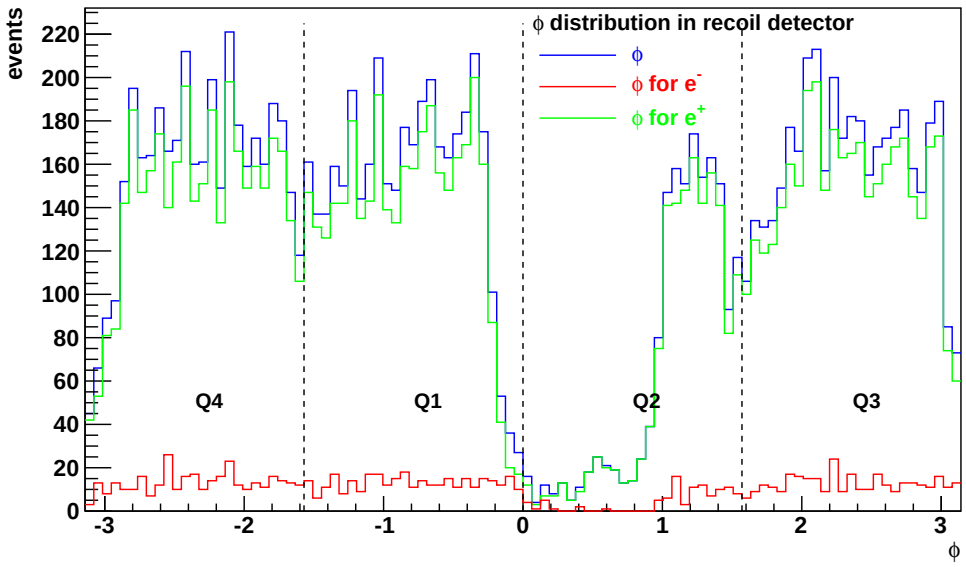

Figure 4.6.1: ϕ distribution of protons detected in the recoil detector with method 3.

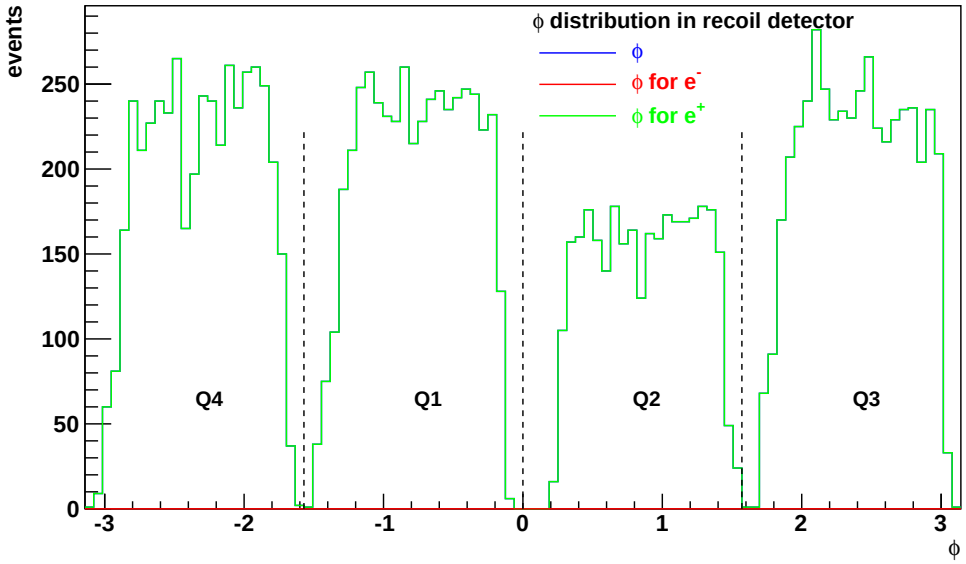

Figure 4.6.2: ϕ distribution of protons detected in the recoil detector with method 7.

4.7 SELECTION OF THE UNRESOLVED REFERENCE SAMPLE

For the selection of the unresolved reference sample unresolved events are processed though an acceptance examination. The expected kinematics (p_{exp}/θ_{exp}) of the recoiling proton calculated from the kinematics of the lepton and the photon are compared with the acceptance of the SFT. Events outside this acceptance are rejected from the unresolved reference sample. In this way a subset of the unresolved reference sample is selected.

In [38] it was shown that the distributions of p_{exp}/θ_{exp} and p_{meas}/θ_{meas} where shifted by a small value. To analyze this effect for method 3 the p/θ values as explained in 4.5.1 where compared. Figure 4.7.1 on page 70 shows the distributions for p_{exp}/θ_{exp} and p_{meas}/θ_{meas} in the Monte Carlo data and Figure 4.7.2 on page 70 in the real data sample. The right row on the figures shows Δp and $\Delta\theta$. These histograms where fit by a GAUSSian function and the mean value of the fit from the MC was used to shift the expected values before they where compared with the recoil acceptance.

4.8 MAXIMUM LIKELIHOOD FIT OF ASYMMETRIES

The extended maximum likelihood (EML) [28] method is used to extract different asymmetry amplitudes from the experimental data. This method abdicates any binning and fits the individual data points one by one. The fitting describes the theoretical dependence of the asymmetry on ϕ.

For the set of N measured events the data quantities $x_i \in \{-t, x_B, Q^2, \phi\}$ from a probability density function (p.d.f.) $p(x,\theta)$, the EML function reads:

$$\mathcal{L}_{EML}(\theta) = \frac{[\mathbb{N}(\theta)]^N e^{-\mathbb{N}(\theta)}}{N!} \prod_i^N p(x_i;\theta) \tag{4.8.1}$$

The POISSON distribution in the EML makes the difference to the standard Maximum Likelihood function. It pays tribute to the fact that the observed number of events can have a POISSON fluctuation about its expectation value $\mathbb{N}(\theta)$.

To avoid rounding differences instead of maximizing the EML the negative log-likelihood function is minimized:

$$-ln\mathcal{L}_{EML}(\theta) = \sum_{i}^{N} ln\left[1 + P_i \mathcal{A}_{LU}(x_i;\theta)\right] + \mathbb{N}(\theta), \tag{4.8.2}$$

$$-ln\mathcal{L}_{EML}(\theta) = \sum_{i}^{N} ln\left[1 + C_i \mathcal{A}_{C}(x_i;\theta)\right] + \mathbb{N}(\theta). \tag{4.8.3}$$

The non-combined expected distribution for the beam spin asymmetry is:

$$\mathcal{A}_{LU}(x_i;\theta) = A_{LU}^{cos(0\phi)} + A_{LU}^{sin(\phi)} \sin(\phi) + A_{LU}^{sin(2\phi)} \sin(2\phi) \tag{4.8.4}$$

and for the beam charge asymmetry:

$$\mathcal{A}_{C}(x_i;\theta) = A_{C}^{cos(0\phi)} + A_{C}^{cos(\phi)} \cos(\phi) + A_{C}^{cos(2\phi)} \cos(2\phi) + A_{C}^{cos(3\phi)} \cos(3\phi) \tag{4.8.5}$$

with the asymmetry amplitudes $A^{f(\phi)}$.

For the beam spin asymmetry the normalization term $\mathbb{N}(\theta)$ reads:

$$\mathbb{N} = \frac{L}{L_{P_\rightarrow}} \frac{\sum_{i,P}(1 + \langle P\rangle \mathcal{A}_{LU}(x_i;\theta))}{1 - \frac{\langle P\rightarrow\rangle}{\langle P\leftarrow\rangle}} + \frac{L}{L_{P_\leftarrow}} \frac{\sum_{i,P}(1 + \langle P\rangle \mathcal{A}_{LU}(x_i;\theta))}{1 - \frac{\langle P\leftarrow\rangle}{\langle P\rightarrow\rangle}}. \tag{4.8.6}$$

For the beam charge asymmetry:

$$\mathbb{N} = \frac{L}{2 \cdot L_{C^+}} \sum_{i,C}(1 + \langle C\rangle \mathcal{A}_{C}(x_i;\theta)) + \frac{L}{2 \cdot L_{C^-}} \sum_{i,C}(1 + \langle C\rangle \mathcal{A}_{C}(x_i;\theta)) \tag{4.8.7}$$

To compare the results with already published amplitudes it is necessary to introduce the combined 13-parameter fit used in former publications that needs all four charge-helicity combinations. The combined 13-parameter fit is done minimizing the function

$$\begin{aligned} -ln\mathcal{L}_{ELM} &= -\Sigma_i^N ln[1 + \eta_i A_C(x_i;\theta) + P_i A_{LU}^{DVCS}(x_i;\theta) \\ &+ \eta_i P_i A_{LU}^{I}(x_i;\theta)] + \mathbb{N}(\theta) \end{aligned}$$

with the beam polarization P_i and the beam charge η_i for each event i fitting the harmonics

$$A_{LU,DVCS} = A_{LU,DVCS}^{\cos(0\phi)} + A_{LU,DVCS}^{\sin(\phi)} \sin(\phi) + A_{LU,DVCS}^{\sin(2\phi)} \sin(2\phi) \tag{4.8.8}$$

$$A_{LU,I} = A_{LU,I}^{\cos(0\phi)} + A_{LU,I}^{\sin(\phi)} \sin(\phi) + A_{LU,I}^{\sin(2\phi)} \sin(2\phi) \tag{4.8.9}$$

$$A_{C} = A_{C}^{\cos(0\phi)} + A_{C}^{\cos(\phi)} \cos(\phi) + A_{C}^{\cos(2\phi)} \cos(2\phi) + A_{C}^{\cos(3\phi)} \cos(3\phi) \tag{4.8.10}$$

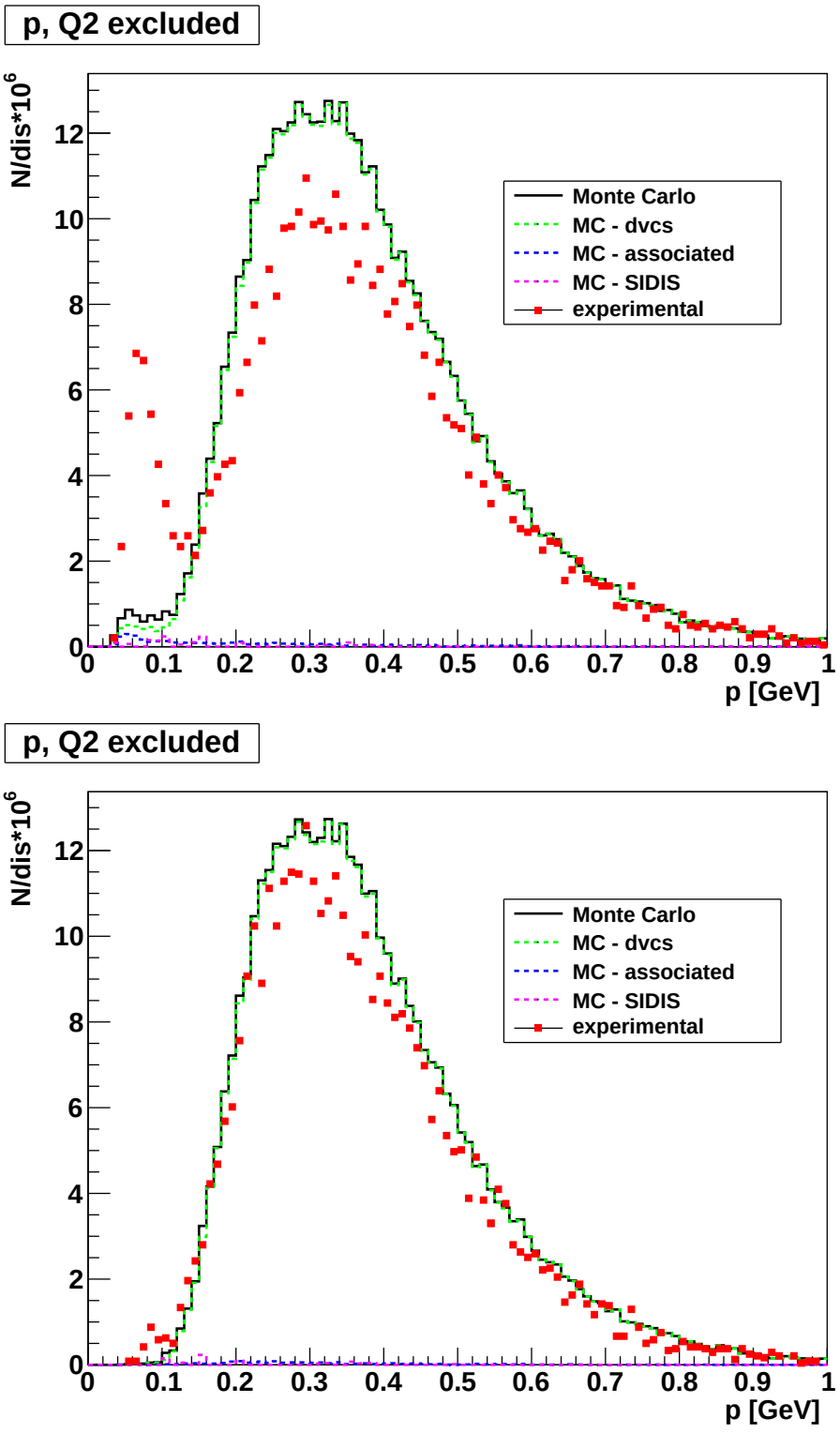

Figure 4.5.5: Momentum distribution for M3 recoil tracking compared to MC before (top) and after (bottom) constant σ adjustment for small momentum values. Presented in [48].

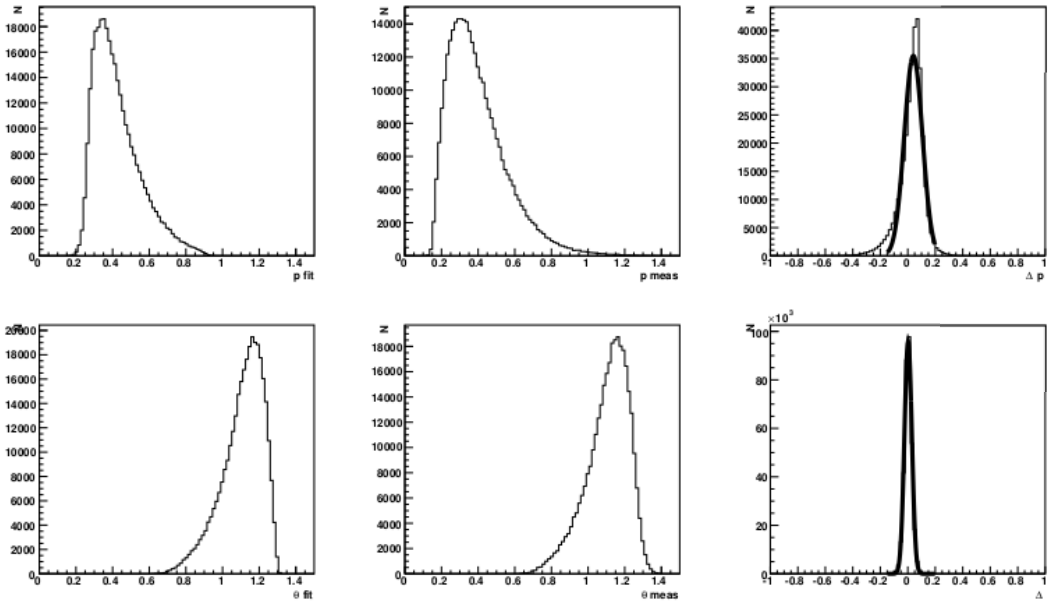

Figure 4.5.6: top: p_{meas} (left) and p_{fit}(center) and $\Delta p = p_{meas} - p_{fit}$ from MC, bottom: θ_{meas} (left) and θ_{fit} (center) and $\Delta\theta = \theta_{meas} - \theta_{fit}$ from MC

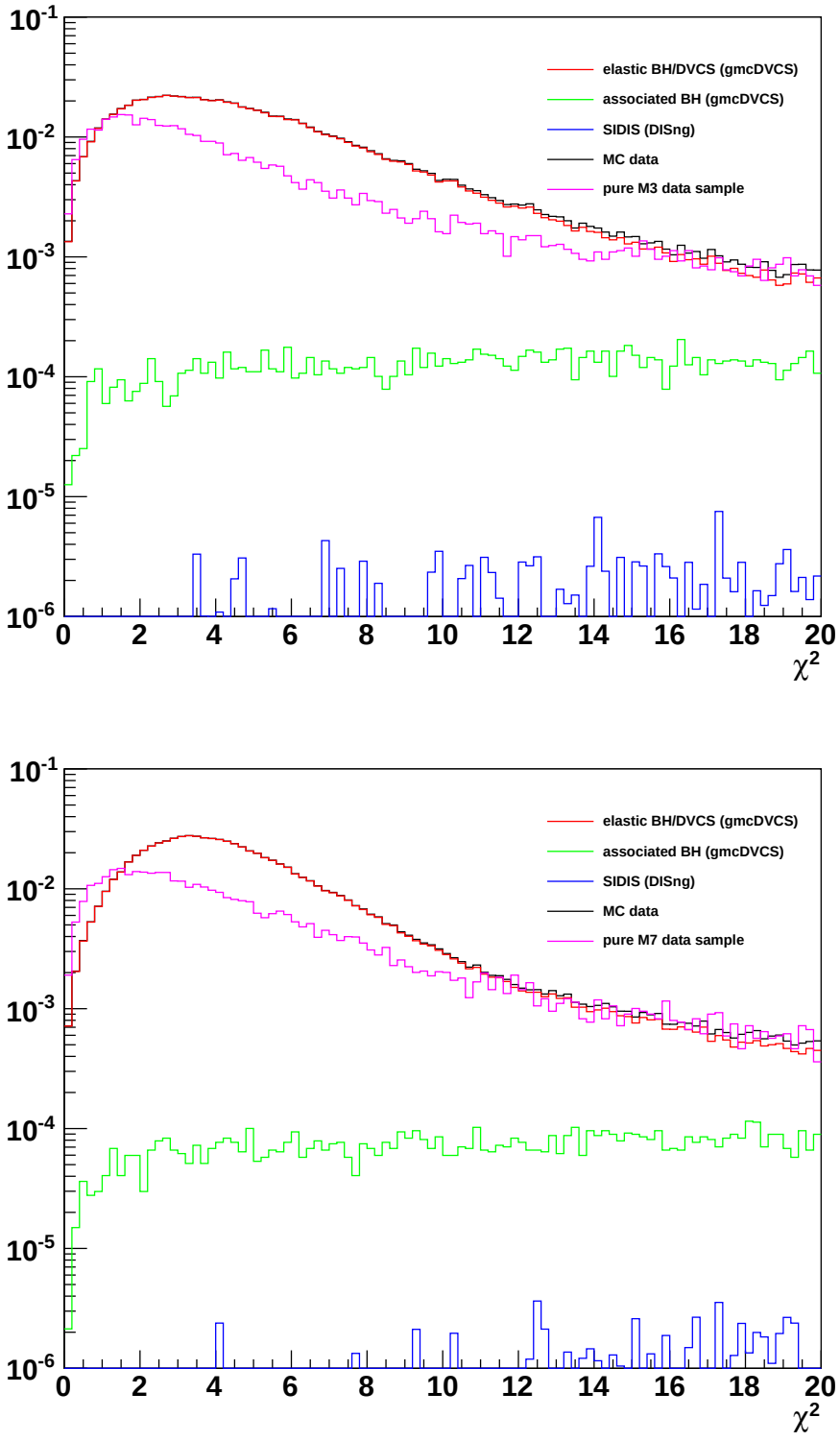

Figure 4.5.7: χ^2_{kin} distribution of the tracks with best χ^2_{kin} in an event for method 3 (top) and method 7 (bottom) in Monte Carlo. For method 3 the χ^2_{kin} values are shifted to higher values. The contamination with background processes is slightly higher, still the background is suppressed by several magnitudes.

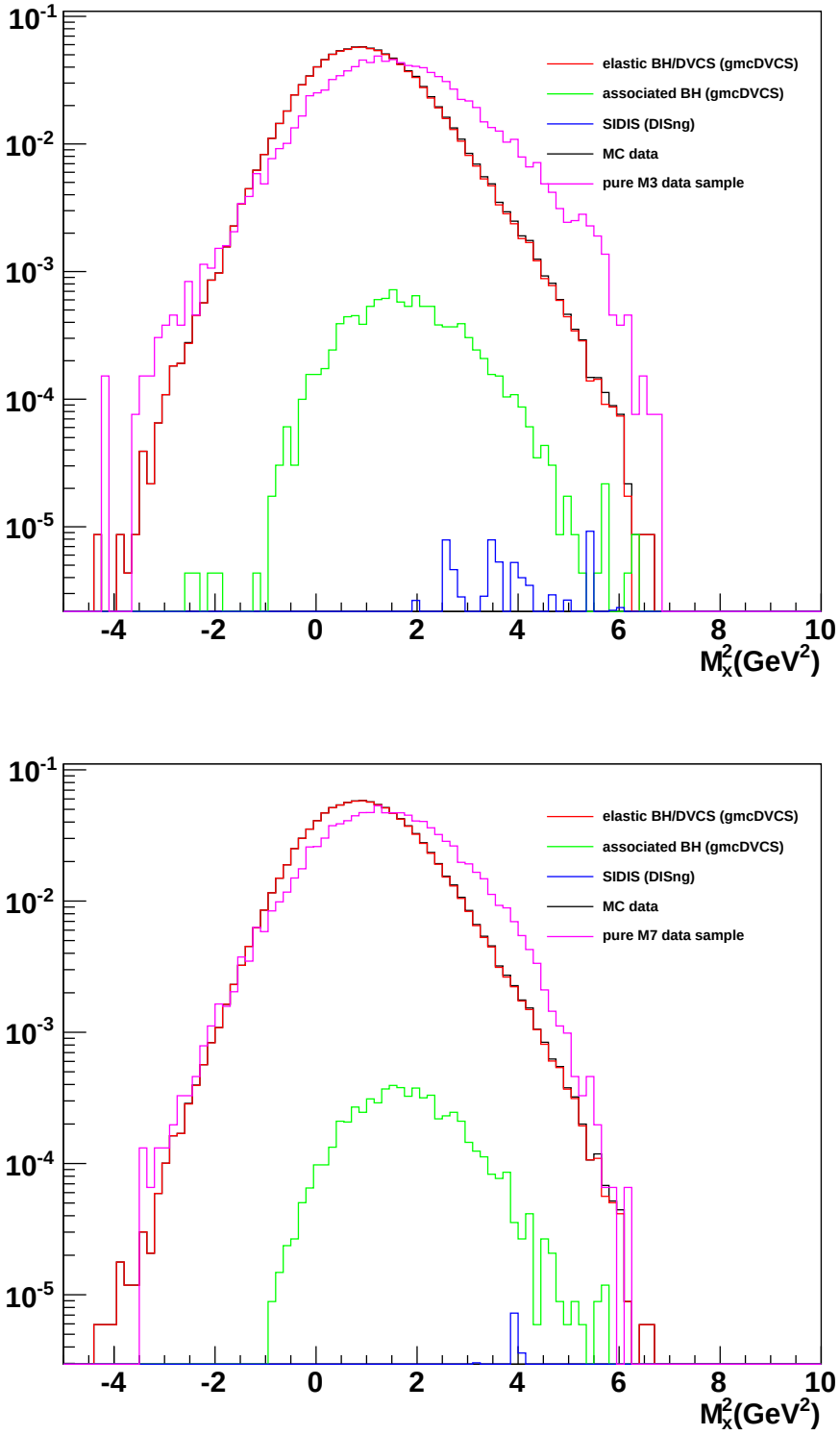

Figure 4.5.8: M_x^2 distribution of the tracks with best $\chi^2_{kin} < 13.7$ a in an event for method 3 (top) and method 7 (bottom) in Monte Carlo. This plots show that the MC M_x^2 distribution agrees for the most part with the measured one but is slightly shifted to higher values. For method 3 this effect is larger than for method 7.

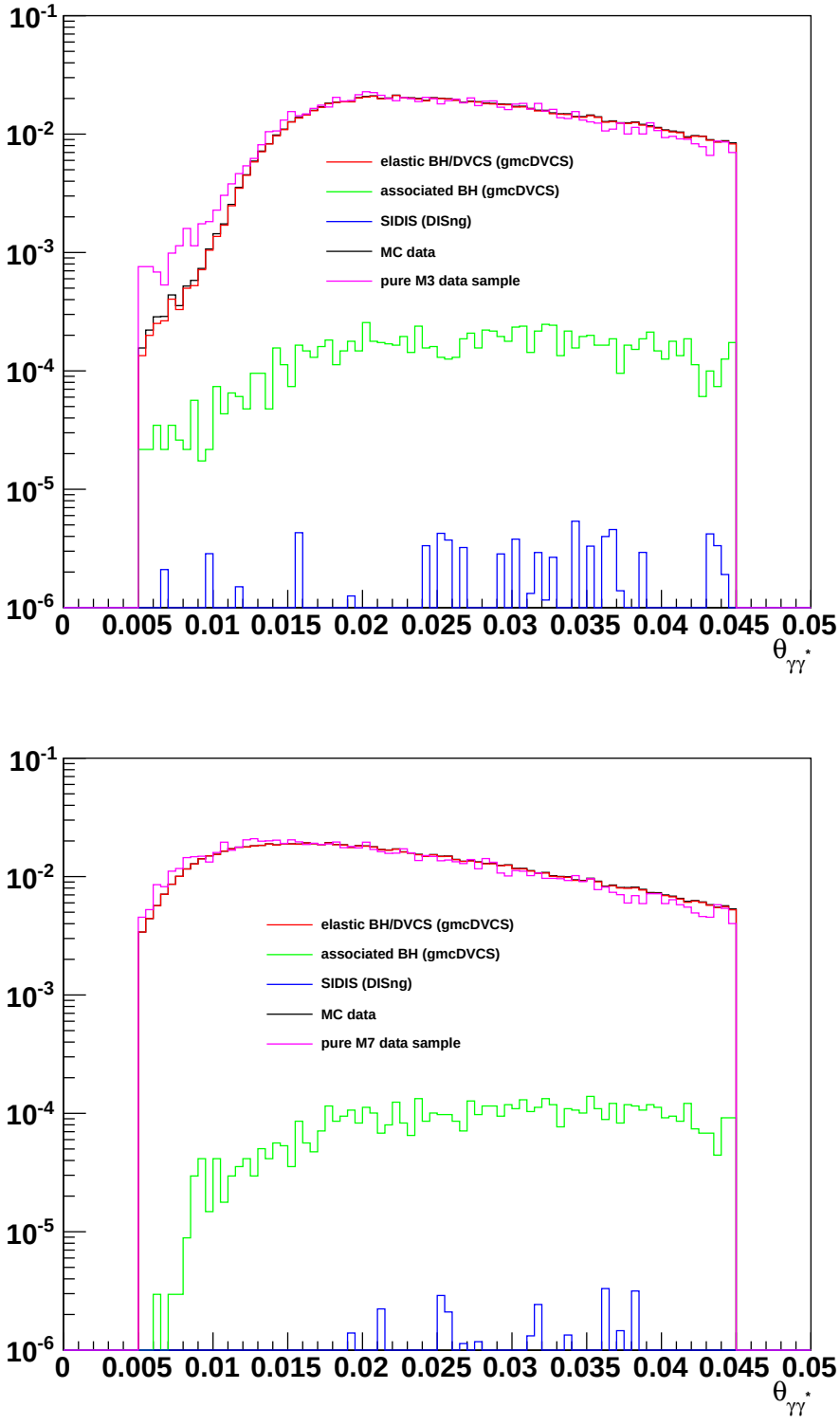

Figure 4.5.9: $\theta_{\gamma\gamma^*}$ distribution of the tracks with best $\chi^2_{kin} < 13.7$ a in an event for method 3 (top) and method 7 (bottom) in Monte Carlo. For both methods the $\theta_{\gamma\gamma^*}$ distribution is in good agreement between real data and MC.

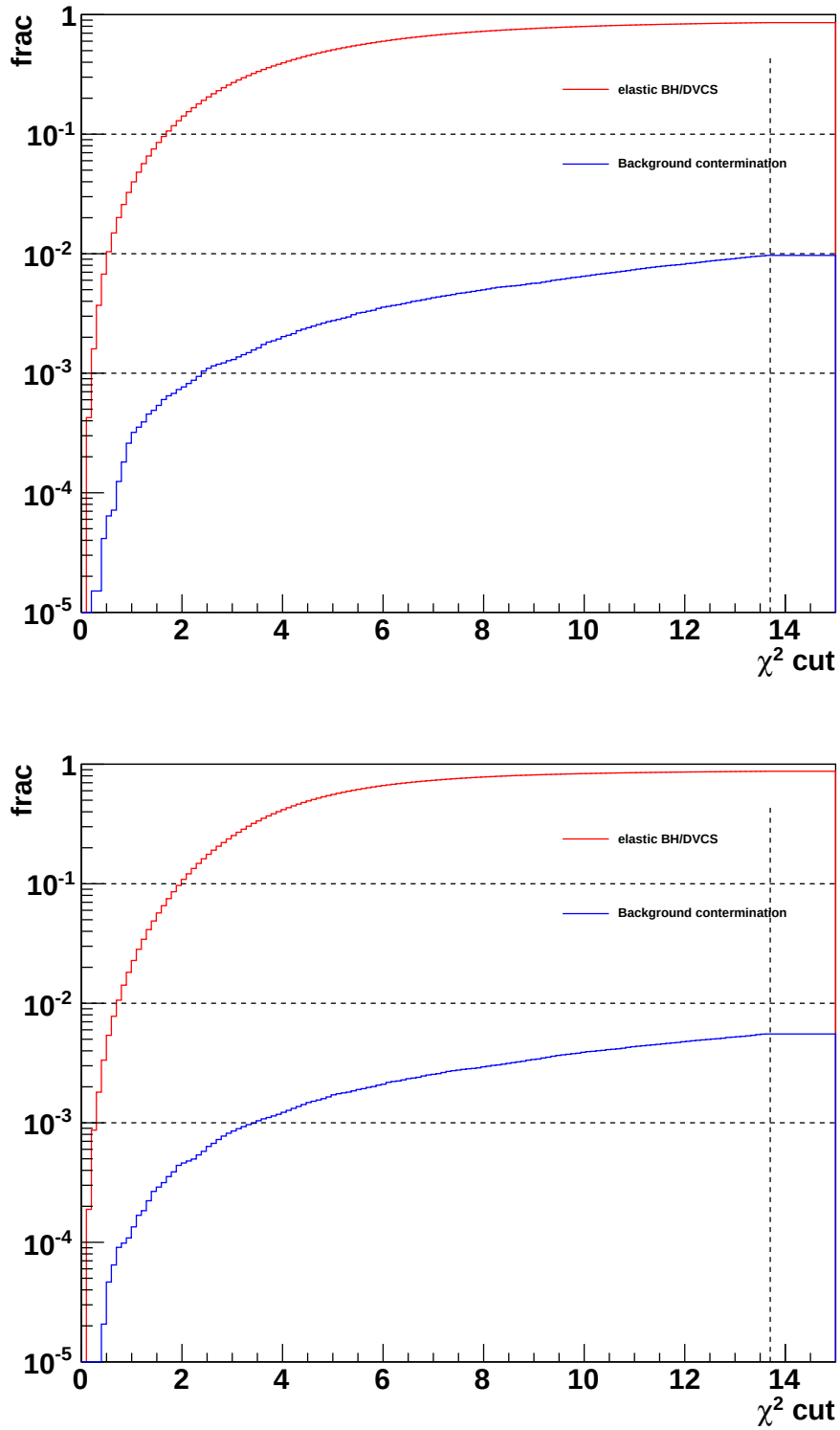

Figure 4.5.10: Fraction of elastic BH/DVCS and background contamination after a cut on χ^2_{kin} from MC data. Method 3 (top), method 7 (bottom).

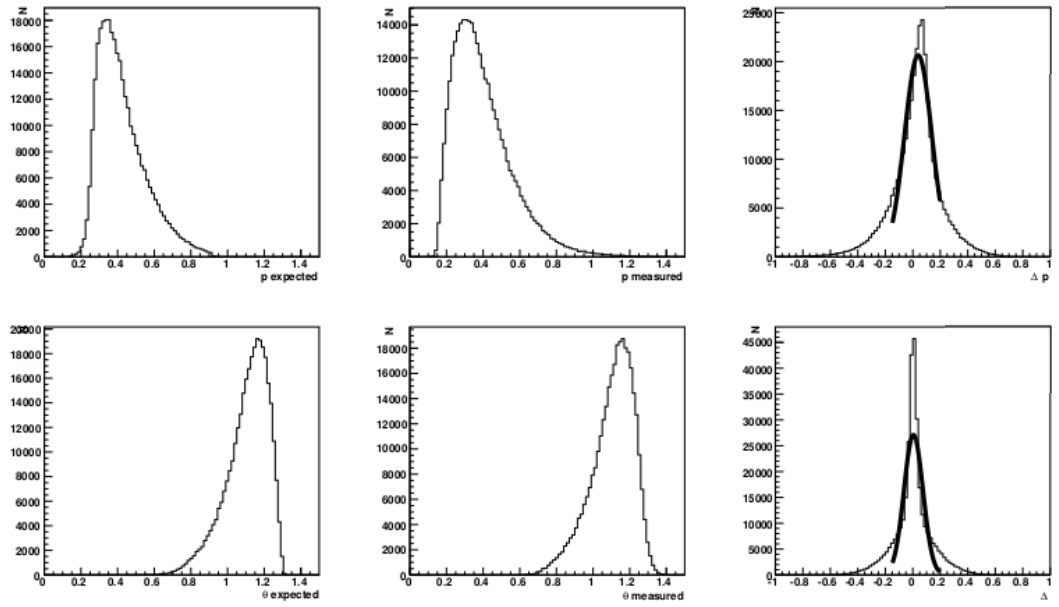

Figure 4.7.1: top: p_{exp} (left) and p_{meas} (center) and $\Delta p = p_{exp} - p_{meas}$ from MC, bottom: θ_{exp} (left) and θ_{meas}(center) and $\Delta\theta = \theta_{exp} - \theta_{meas}$ from MC. Peak value for Δp is 0.0392 and for $\Delta\theta$ 0.00497

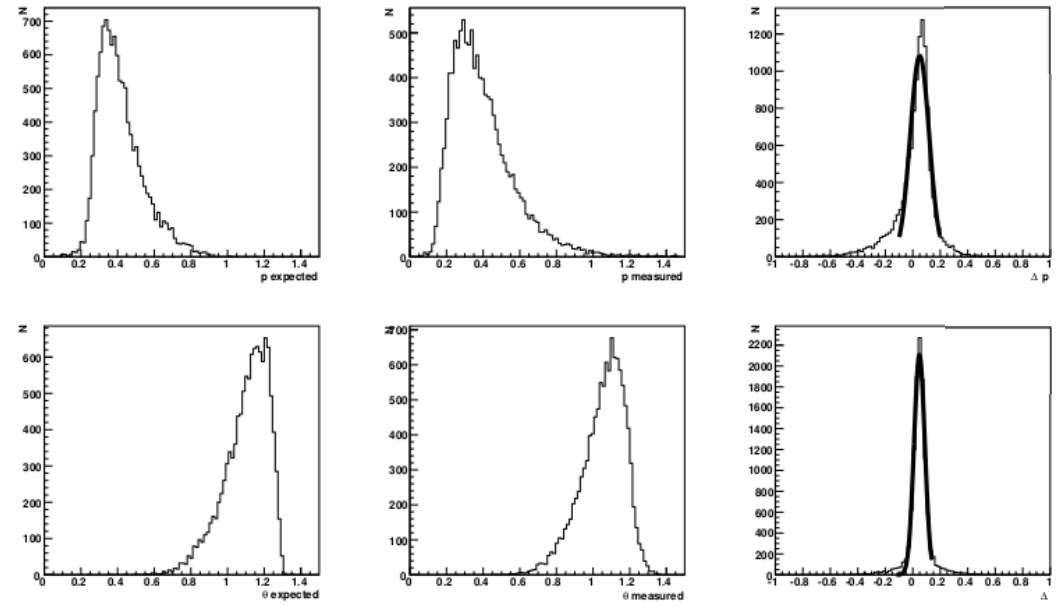

Figure 4.7.2: top: p_{exp} (left) and p_{meas}(center) and $\Delta p = p_{exp} - p_{meas}$ from real data, bottom: θ_{exp} (left) and θ_{meas} (center) and $\Delta\theta = \theta_{exp} - \theta_{meas}$ from real data. The peaks of Δp and $\Delta\theta$ are shifted to higher values 0.0503 and 0.0484. The shift of the peak is used as a correction during the data sample extraction.

Part III

ANALYSIS

5 BEAM CHARGE ASYMMETRY

5.1 VALIDATION OF THE ANALYSIS METHOD

The available data set restricts the choice of analysis methods. Only the extraction of method 3 is available for electron data, that is necessary for the fit of BCA. Additionally the electron data has only negative helicity.

It will be shown that method 3 produces asymmetries that are comparable with those obtained with method 7. The second step is to approve a 4 parameter fit that will be used instead the 13 parameter fit, which is impossible without positively polarized electron data.

$$-ln\mathcal{L}_{BCA} = -\Sigma_i^N ln[1 + \eta_i A_C(x_i;\theta)] + \mathbb{N}(\theta) \tag{5.1.1}$$

and

$$A_C = A_C^{\cos(0\phi)} + A_C^{\cos(\phi)}\cos(\phi) + A_C^{\cos(2\phi)}\cos(2\phi) + A_C^{\cos(3\phi)}\cos(3\phi) \tag{5.1.2}$$

reproduces similar amplitudes in beam charge asymmetry.

5.1.1 *Validation of method 3*

A validation on beam charge asymmetry fitting is not possible because no data taken with an electron beam is available for method 7.

Method 3 and method 7 data sets are not disjoint, also neither of the sets is the subset of the other. As Figure 4.5.3 on page 52 shows the methods serve different combinations of space points in the recoil detector.

The kinematic range in the variables
$t_c = \frac{-Q^2 - 2\nu(\nu - \sqrt{\nu^2+Q^2}\cos\theta_{\gamma\gamma^*})}{1+\frac{1}{M}(\nu - \sqrt{\nu^2+Q^2}\cos\theta_{\gamma\gamma^*})}$,
$x_B = (Q^2)/(2Pq) = Q^2/(2M\nu)$
and $Q^2 \equiv -q^2 := -(k-k')^2 \overset{\text{lab}}{\approx} 4E_B E' \sin^2(\theta/2)$
is effected by this fact and differs between the data sets selected by method 3 or method 7. Figure 5.1.1 on page 74 shows the distributions in comparison of method 3 and 7. Without the SSD the loss of statistics for low $-t_c$ is obvious and in the lowest $-t_c$ bin are only few events left, a reasonable analysis for this bin with method 3 is arguable. Figure 5.1.2 on page 75 verifies the distributions through a comparison of real and Monte Carlo distributions.

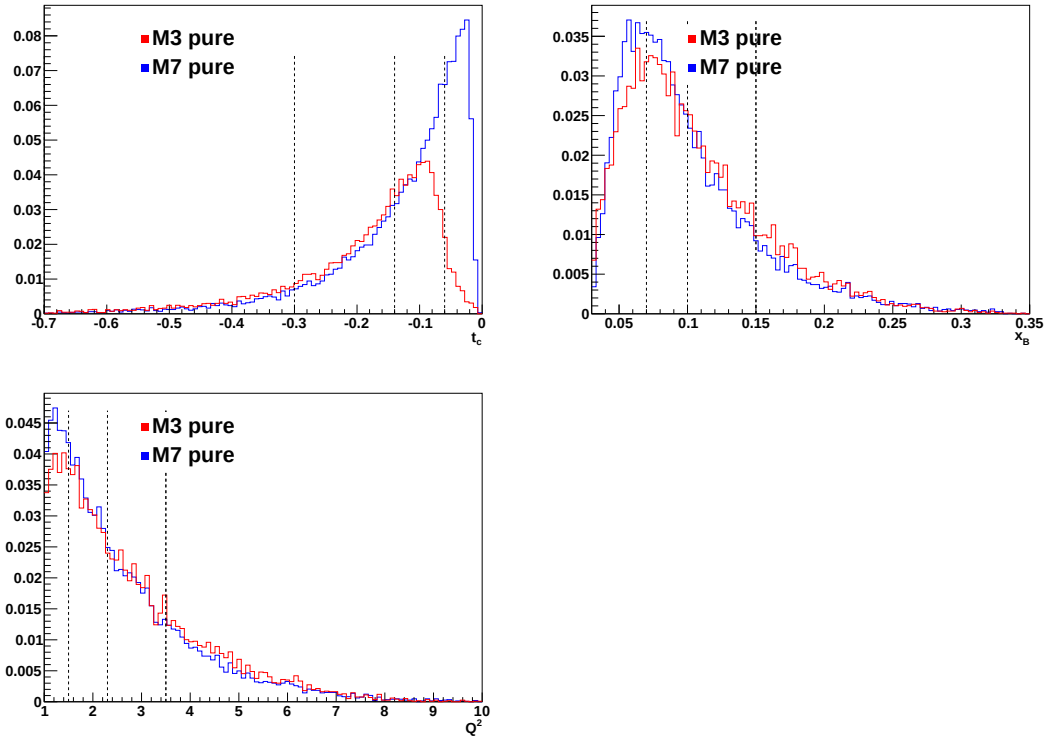

Figure 5.1.1: Distributions of the kinematic variables t_c, x_B and Q^2 in the pure data sample for method 7 and method 3. Dashed lines mark the 4 bins used for the asymmetry amplitude fits. The x_B and Q^2 histograms where normalized to the number of entries of the histogram and the t_c histogram was normalized to the number of entries for $-t > 0.06$.

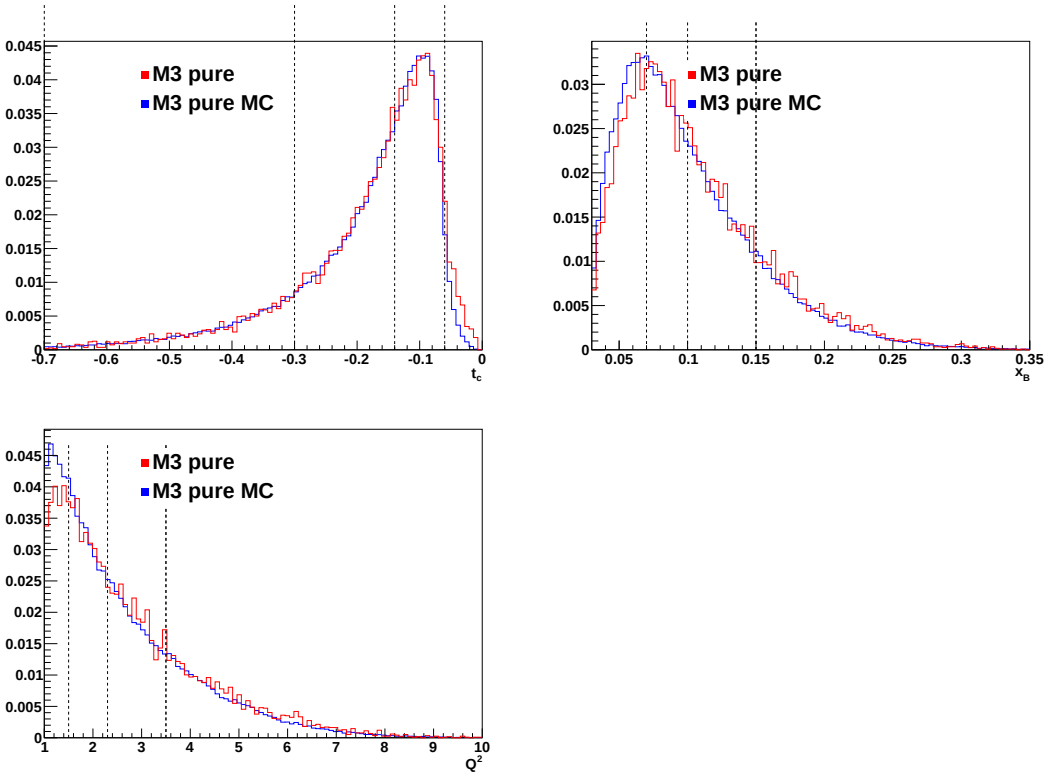

Figure 5.1.2: Distributions of the kinematic variables t_c, x_B and Q^2 in the pure data sample for method 3 Monte Carlo and real data. Dashed lines mark the 4 bins used for the asymmetry amplitude fits. The histograms where normalized to the number of entries of the histogram.

To prove that method 3 analysis is still possible and similar results can be expected for method 3 and 7 a beam charge asymmetry fit was performed with both methods and compared. The fit was done with a non combined maximum likelihood function

$$-ln\mathcal{L}_{BSA} = -\Sigma_i^N ln[1 + P_i A_{LU}^{DVCS}(x_i;\theta)] + \mathbb{N}(\theta) \tag{5.1.3}$$

with

$$A_{LU,DVCS} = A_{LU}^{\cos(0\phi)} + A_{LU}^{\sin(\phi)} \sin(\phi) + A_{LU}^{\sin(2\phi)} \sin(2\phi) \tag{5.1.4}$$

The result of this comparison can be viewed in Figure 5.1.3 on page 76. The method 3 results are compatible with the method 7 results, however the statistical precision of the method 3 result is smaller due to a reduced reconstruction efficiency, especially at small t_c as expected from the distributions of the kinematic variables.

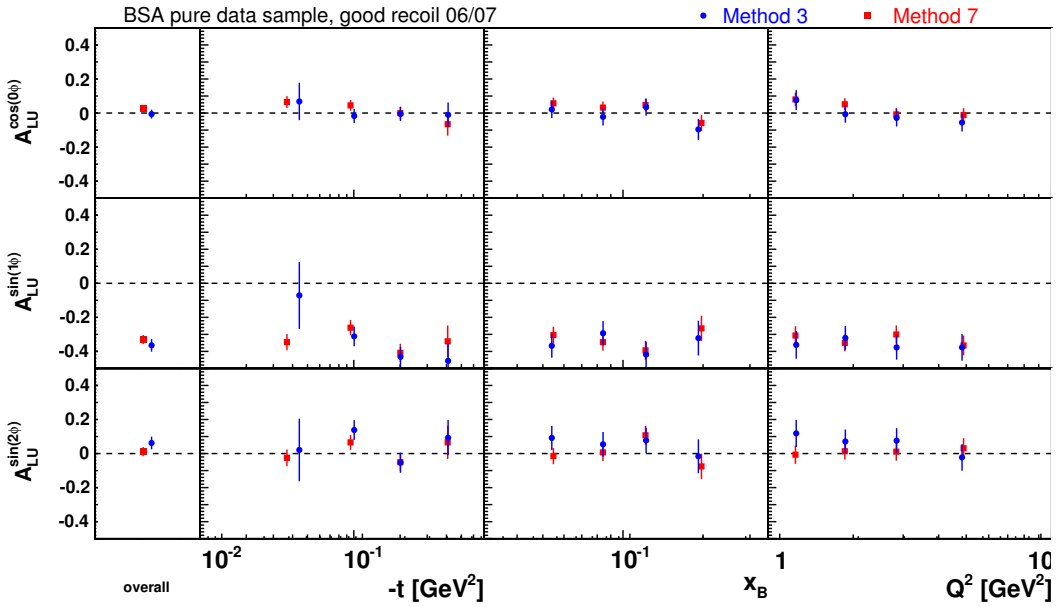

Figure 5.1.3: Comparison between method 7 and method 3.

5.2 VALIDATION OF 4-PARAMETER FIT

For the validation of the 4-parameter fit compared to the 13-parameter fit it is necessary to perform a fit on beam charge asymmetry and beam spin asymmetry at the same time.

The only data sample that allows this is the unresolved data sample as every combination of beam charge and spin is available there.

In the first stage of this undertaking a cross check with the published asymmetries was performed.

For the following crosscheck an unresolved data sample was used to compare this analysis with the published data.

- BSA unresolved: comparison to publication [22], used bit pattern 0x7c1e1bdc (good recoil period), (Figure 5.2.1 on page 77)
- BCA unresolved: comparison to publication [21], used bit pattern 0x501e1bdc (all 2006/2007 data) (Figure 5.2.4 on page 79).

For each comparison, the respective same data set was used, as selected by data quality cuts.

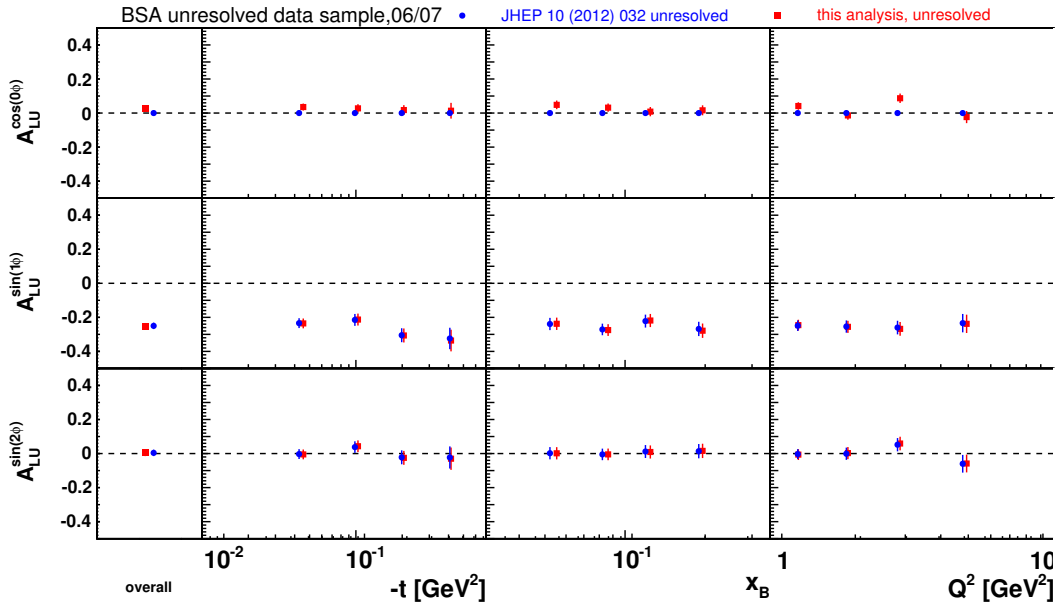

Figure 5.2.1: Amplitudes of BSA. Comparison between the publication and this analysis.

5.2.1 M_x^2 window adjustment for electron and positron data

At the moment when electron events are included into the analysis of the unresolved data sample an adjustment of the M_x^2 window is necessary as the M_x^2 distribution has a shift in the exclusive peek between electron and positron data. This is known from the previous analysis [78, 75, 40] and can be attributed to a detector misalignment.

For this the M_x^2 distribution for the positron data sample is plotted and fitted with a Gaussian distribution (Figure 5.2.2 on page 78). The window of $[-3\sigma, 1\sigma]$ gives an accepted range (in [GeV^2]) of [-2.25, 2.89] for the positron data. For the electron data the window is shifted to the mean value of the electron M_x^2 distribution that leads to a range of [-2.47, 2.67] [78].

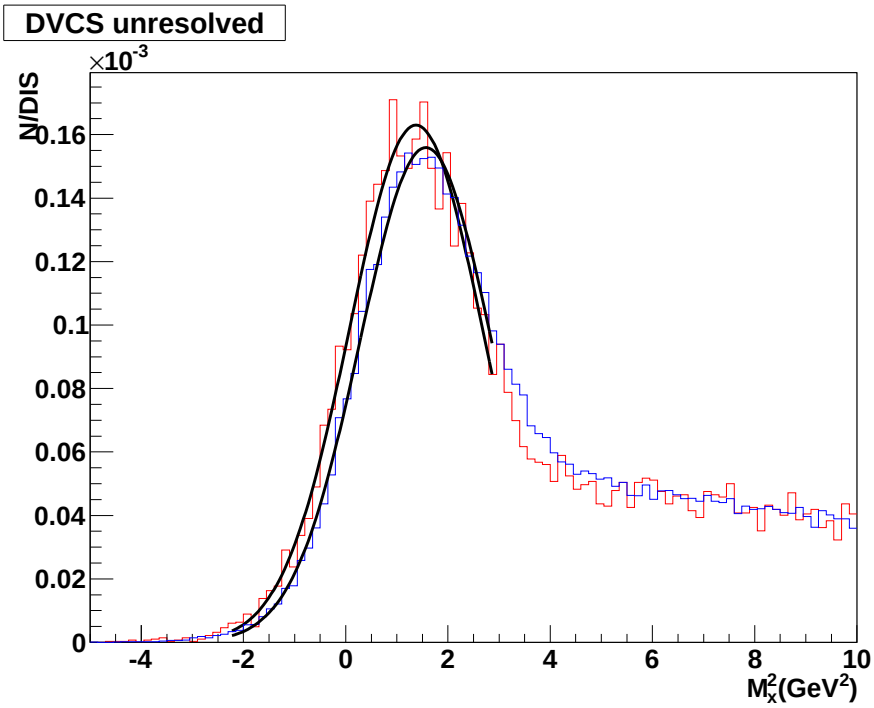

Figure 5.2.2: Gaussian fit to the M_x^2 distribution of electron (blue) and positron (red) data. For a better comparison the amplitudes are normalized to the number of DIS events.

5.2.2 *Unresolved sample: comparison with publication*

To compare BCA amplitudes with the publication (5.2.3) the same 13 parameter fit on BSA and BCA was performed on the unresolved data sample without using recoil-detector information as was used in the publication. A recalibration of the calorimeter since the publication can be charged with the small differences in the amplitudes.

Minor differences can be attributed to a fix on a problem with calorimeter pedestals between the publication [38] as described in [37] and this analysis.

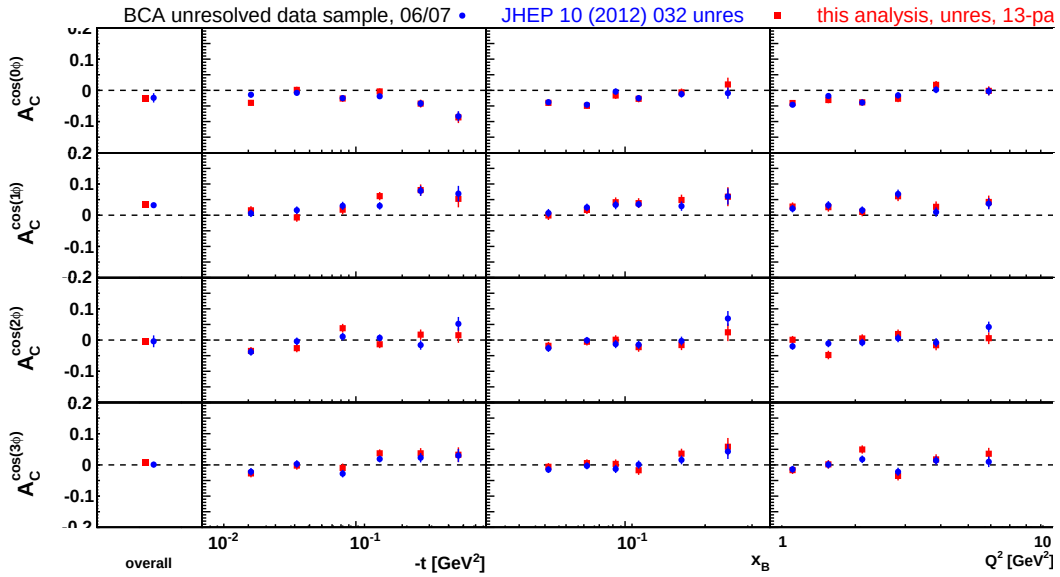

Figure 5.2.3: Amplitudes of BCA from unresolved data sample of 2006 and 2007 data, combined 13 parameter fit. Comparison between the publication and this analysis.

A comparison in Figure 5.2.4 on page 79 between the combined 13 parameter fit on BCA and the 4 parameter fit shows only minor differences. This shows that the non-combined 4 parameter fit is not adverse and can be used for the analysis of the data that was taken using the kinematically complete event reconstruction.

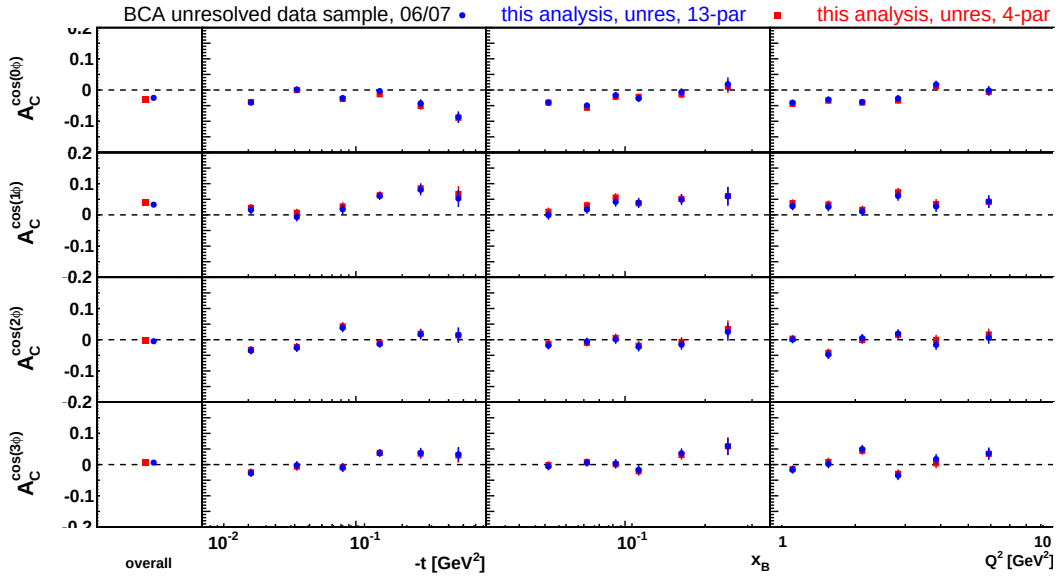

Figure 5.2.4: Amplitudes of BCA from unresolved data sample of 2006 and 2007 data. Comparison between the combined 13 parameter fit and the non-combined 4 parameter fit.

5.3 EXTRACTION OF BEAM CHARGE ASYMMETRY

The steps of the extraction of BCA amplitudes are the selection of the pure data sample, the cut to a sub sample usable for the analysis, and finally the maximum likelihood fit on the selected data subset.

Selecting the data subset for the beam charge asymmetry fit the following cuts are applied on the list of tracks as discussed before:

- data selection cuts for the pure data sample (4.4)
- exclusion of the quadrant 2 of the recoil detector (Section 4.6)
- $\chi^2 < 13.7$ cut on the track with smallest χ^2 per event (4.5.1)
- data quality cut to valid time periods (Table 4.5.1 on page 56)

After this selection the maximum likelihood fit is performed as described in Section 4.8 as a 4 parameter fit on BCA. This first plot is shown in Figure 5.3.1 on page 80

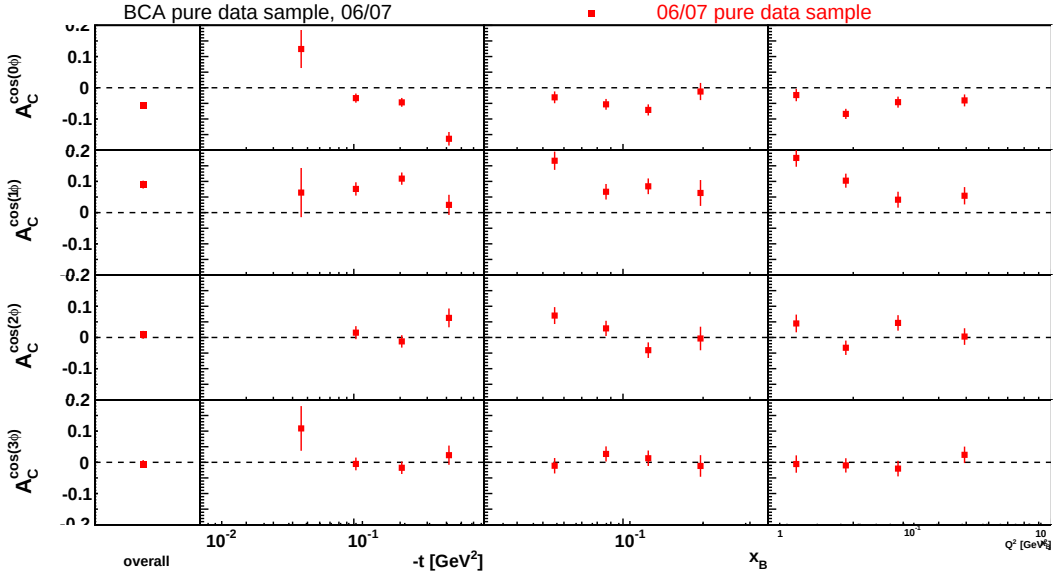

Figure 5.3.1: Amplitudes of beam charge asymmetry from pure data sample extracted with BadBit 0x741e1bdc.

5.4 COMPARABILITY OF THE RESULT

It is obvious from Figure 5.3.1 on page 80 that the information in the first t_c bin is not very reliable as the statistics are low. In a comparison with the amplitudes estimated with the unresolved data sample. Especially for the constant term ($A_C^{\cos(0\phi)}$) and the $A_C^{\cos(\phi)}$ term the amplitudes are much larger (Figure 5.4.1 on page 81).

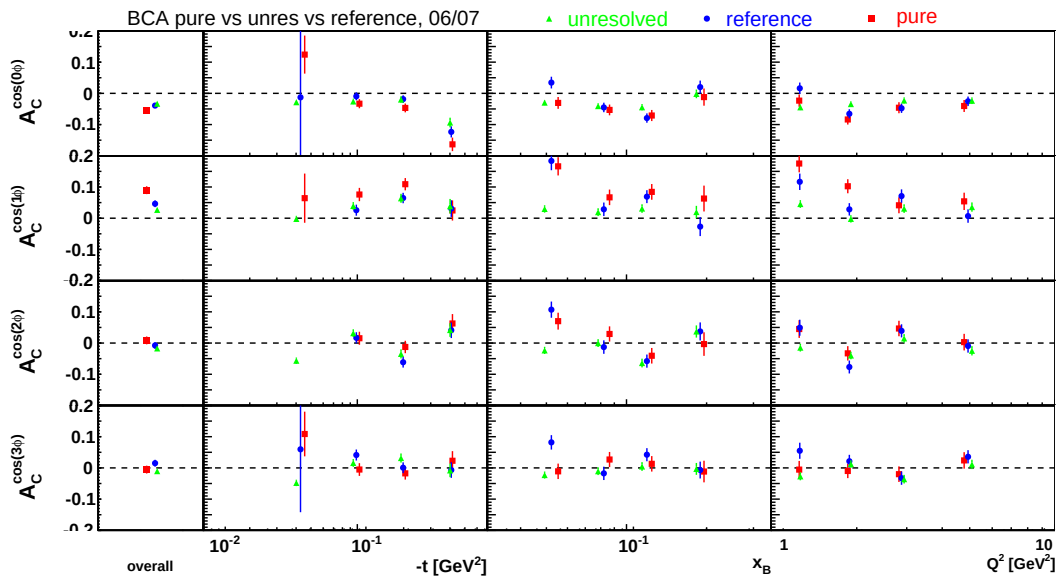

Figure 5.4.1: Red Squares: Amplitudes of BCA of the pure sample extracted with recoil-tracking method 3, the BadBit 0x741e1bdc. The blue circles represent the results extracted from the 2006/2007 data set with BadBit 0x501e03dc in the unresolved data sample and the green triangles mark the asymmetries extracted from the unresolved reference sample from the same data set. All three samples where cut to the same time period.

Especially in the lower x_B and Q^2 bins there is a large discrepancy between the pure and reference data sample. To investigate the reason for this difference three possible sources where identified. First of all the pure data set is cut on a distinct time period in contrast to the reference sample. Secondly the data samples have a slightly different kinematic due to the acceptance of the SFT detector and finally the pure data sample is almost devoid of background from associated processes.

The second question is if a cut to the same kinematics could bring the two samples closer together. Particles with low momentum are not able to reach the SFT part of the recoil detector, which changes the distribution of the kinematic variables. Figure 5.1.1 on page 74 shows that in the pure method 3 data sample the first t bin is very low in statistics while the reference sample is unaffected of the momentum acceptance of the recoil detector. To equalize the samples in this aspect the lowest t_c bin was excluded from the asymmetry fit displayed in Figure 5.4.2 on page 82. This adjustment brings the lower x_B and Q^2 bins slightly closer together. A separate cut on the first t_c bin the complete data set without an additional time selection is shown in Figure 5.4.3 on page 83.

Finally the influence of the associated processes is studied. For this purpose the fraction of the associated events [47] in each bin was multiplied with the asymmetry amplitude value for associated events from [47]. The pink points in 5.4.4 symbolize the asymmetry amplitudes of the reference sample corrected by the contribution of the associated events. These shifted amplitudes are not meant to be a correction but a test how much of the shift is possibly attributed to the associated events. The fractions of associated events in each bin are taken from gmcDVCS Monte Carlo and the shifted reference sample amplitudes are calculated as following:

$$A_{ref}^{shift} = A_{ref,DVCS} + F_{asso} \cdot A_{asso}$$
$$\Delta A_{ref}^{shift} = A_{ref,DVCS} + F_{asso} \cdot \Delta A_{asso}$$

with fraction F_{asso} of associated events for each bin from MC and amplitudes A_{asso} for associated events from [47].

After this corrections the differences between the pure reference sample become a little clearer. The strongest effect is coming from the different kinematics in the samples but even with all corrections the difference in the first Q^2 is not fully resolved. For this reason the amplitudes from the pure sample can be regarded as a real physics effect.

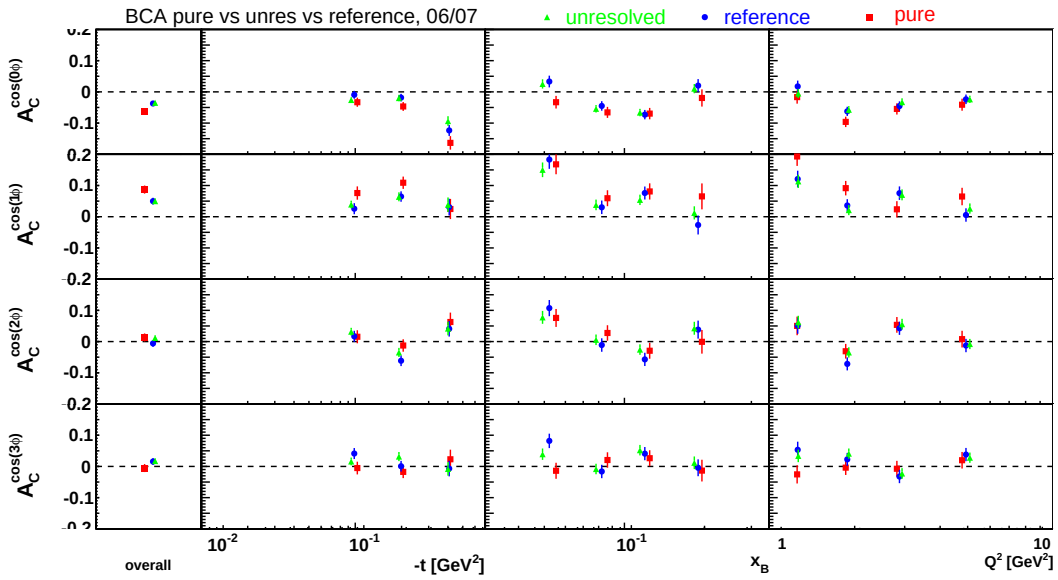

Figure 5.4.2: Three data samples where cut to the same time period and without the lowest t_c bin. Red Squares: Amplitudes of BCA of the pure sample extracted with recoil-tracking method 3 and the BadBit 0x741e1bdc. The blue circles represent the results extracted from the 2006/2007 data set with BadBit 0x501e03dc in the unresolved reference data sample and the green triangles mark the asymmetries extracted from the unresolved sample from the same data set.

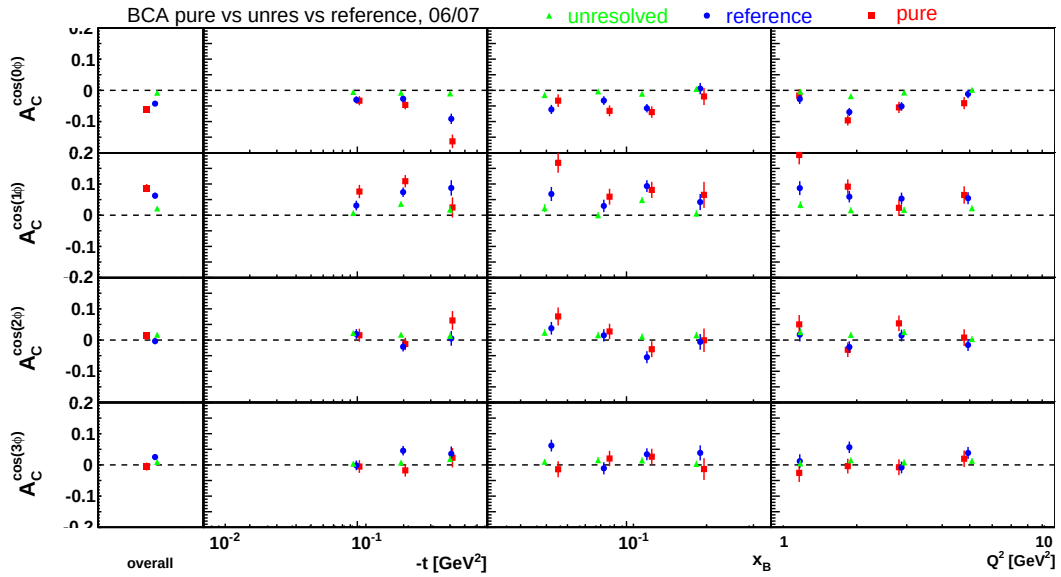

Figure 5.4.3: Three samples are fit without the lowest t_c bin. Red Squares: Amplitudes of BCA of the pure sample extracted with recoil-tracking method 3 and the BadBit 0x741e1bdc. The blue circles represent the results extracted from the 2006/2007 data set with BadBit 0x501e03dc in the unresolved reference data sample and the green triangles mark the asymmetries extracted from the unresolved sample from the same data set.

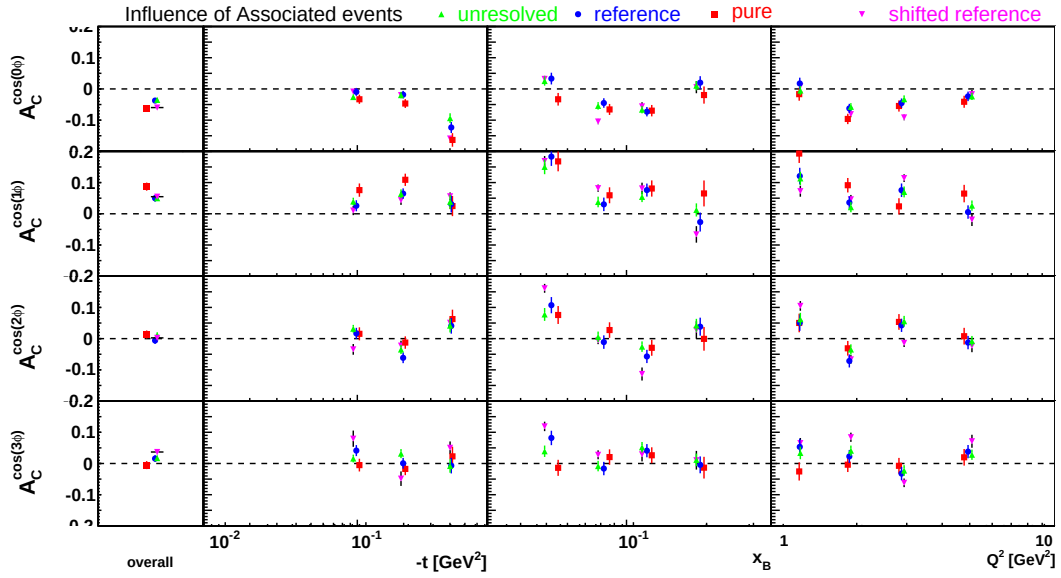

Figure 5.4.4: All three data samples cut on the same time period without the lowest t_c bin. The pink markers symbolize the asymmetry amplitudes of the unresolved reference sample corrected by the contribution of the associated events.

5.5 TIME STABILITY

The most difficult question to prove is the time stability of the data included in this study. The data set is split by the Hermes shut down and has slightly different conditions for electron and positron data. The charge of the beam was not altered in short time periods but only changed once and small time periods have been removed by hand regarding the recoil detector data quality. The forward detector data is assumed to be time consistent even though the year 2006 was excluded from some ongoing not yet published HERMES studies.

5.5.1 *Influence of charge/helicity combination in the unresolved data sample*

From the comparison of Figure 5.4.2 on page 82 and Figure 5.4.3 on page 83 we can see that some significant differences appear in the unresolved and reference data sample only according to the selected time period. To prove that this difference can be attributed to the charge-polarization combination in this time period Figure 5.5.1 on page 85,Figure 5.5.2 on page 85 and Figure 5.5.3 on page 86 where produced. 5.5.1 shows the selected vs. the excluded time period. 5.5.2 shows the unresolved fit without $e^- \uparrow$ and 5.5.3 without $e^- \downarrow$. Finally Figure 5.5.4 on page 86 adds the $e^- \uparrow$ data to the selected time period. These plots show that especially for low x_B and high t_c values the beam charge asymmetry varies significantly depending on the charge and polarization constellation. This is not a phenomenon explained by theoretical considerations inside the VGG model. Comparing a VGG Monte Carlo simulation with all charge/helicity combinations equally represented with its subset where each charge/helicity combination is represented proportionally to the event numbers in the unresolved data sample the difference is small. Both MC samples Figure 5.5.5 on page 87 do not image the raise of $A_C^{\cos(0\phi)}$ and $A_C^{\cos(1\phi)}$ in the first x_B bin or the fall of $A_C^{\cos(1\phi)}$ in the last t_C bin.

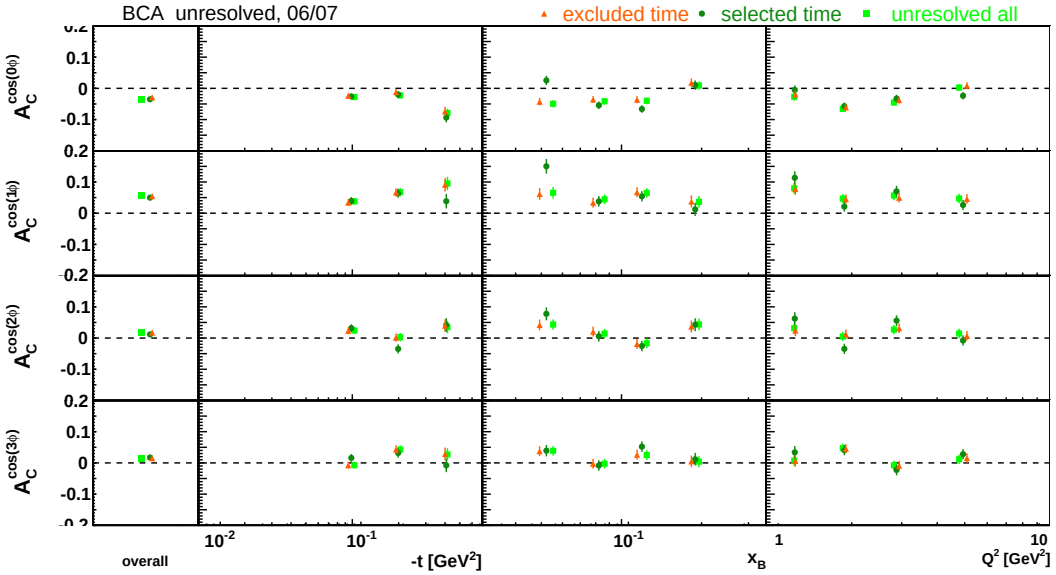

Figure 5.5.1: Comparison between the complete unresolved data sample (green), the selected data sample (dark green) that corresponds to the selected time in the pure data sample (blue in Table 4.5.1 on page 56). and the excluded unresolved data sample subset (orange) which contains all unresolved data but the selected time periods (black in 4.5.1).

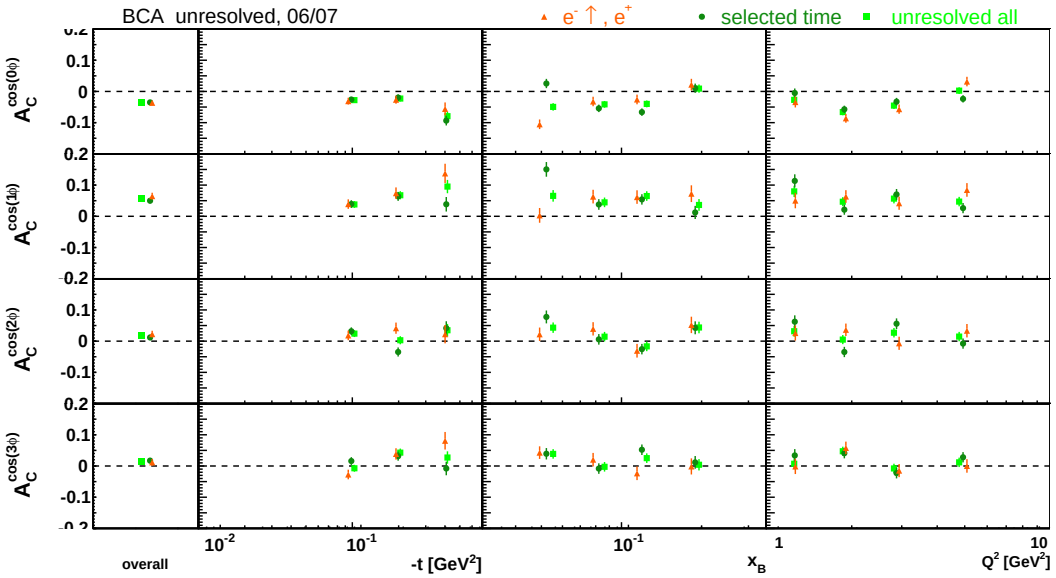

Figure 5.5.2: Complete (green) and selected(dark green) unresolved data sample as in 5.5.1, only positively polarized electron and complete positron data sample (time period 8 in 4.5.1) in orange.

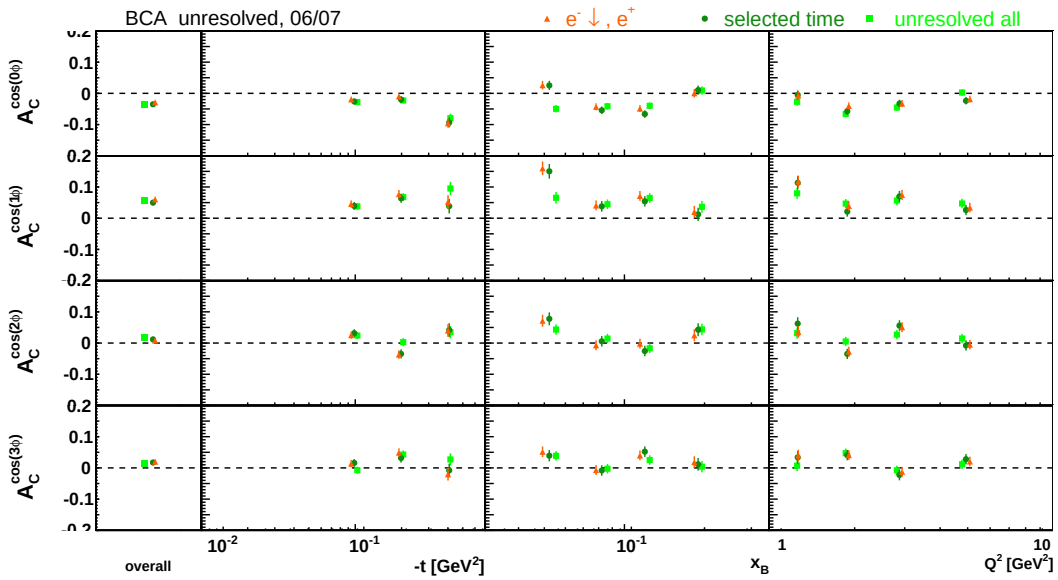

Figure 5.5.3: Complete (green) and selected (dark green) unresolved data sample as in 5.5.1, only negatively polarized electron data sample: (Time period 2, 4 and 6 in 4.5.1) in orange.

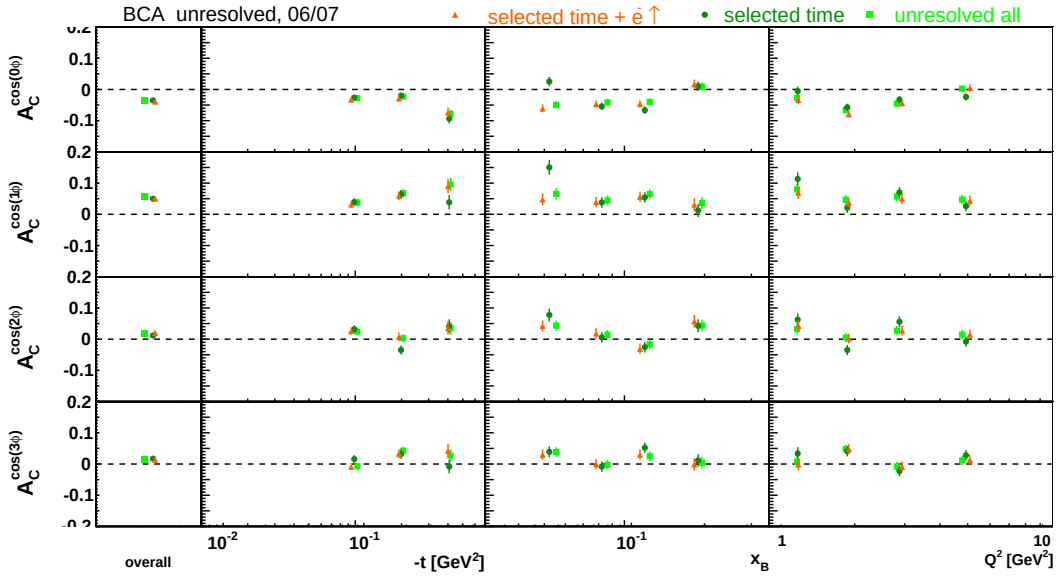

Figure 5.5.4: Comparison between the complete unresolved data sample (green), the selected data sample (dark green) that corresponds to the selected time in the pure data with positively polarized electron data added (orange) (blue in 4.5.1 and time period 8).

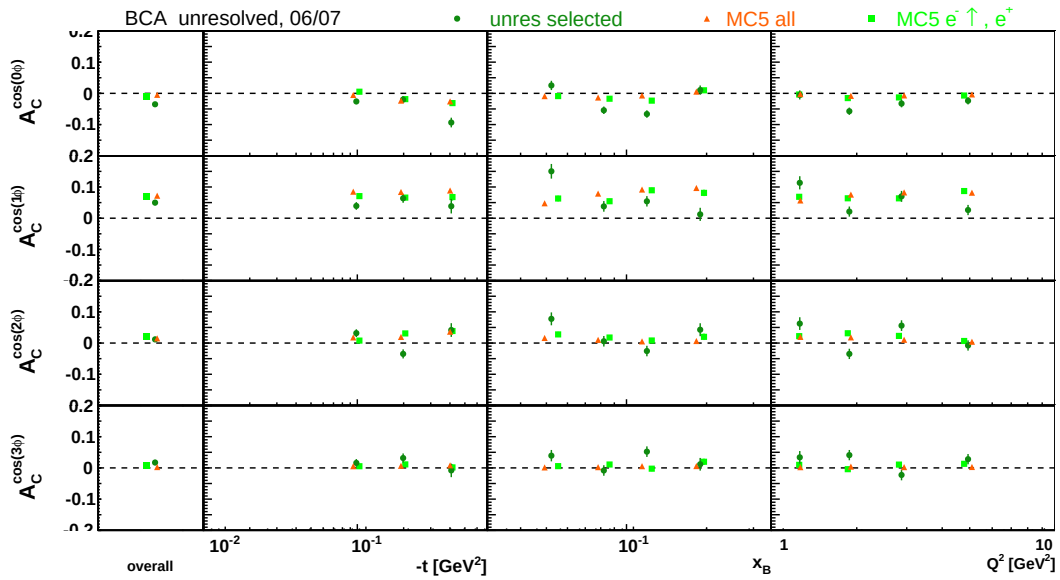

Figure 5.5.5: Selected time periods of the unresolved data sample (dark green) compared to a complete MC (VGG model 5, see 6.1.1) data set where all 4 charge/polarization combinations are represented equally and a MC data subset where the combinations are represented proportionally to the DIS numbers in the selected time period.

At this point it is not possible to say if the difference occurs from a physical phenomenon or a time inconsistency in the data. If the last option is true this would affect not only the unresolved data sample but also the pure and reference data sample.

5.5.2 *Time dependence studies on all charge/polarization combinations*

After receiving the hint that there might be some kind of charge/polarization combination dependence of the BCA the selected time periods in Table 4.5.1 on page 56 are examined in detail on time consistency. Each of the time periods: 2, 4 and 6 (Figure 5.5.12 on page 91,Figure 5.5.13 on page 91), 10 (Figure 5.5.6 on page 88,Figure 5.5.7 on page 88), 11 and 12 (Figure 5.5.10 on page 90,Figure 5.5.11 on page 90) and 16 (Figure 5.5.8 on page 89,Figure 5.5.9 on page 89) was split in 8 parts of equal size each. For every set one of the eight parts was excluded from the analysis and the sets are displayed in two plots for a better readability for every time period. While the positron time periods look totally consistent there are some discrepancies in the electron time periods (2, 4 and 6)

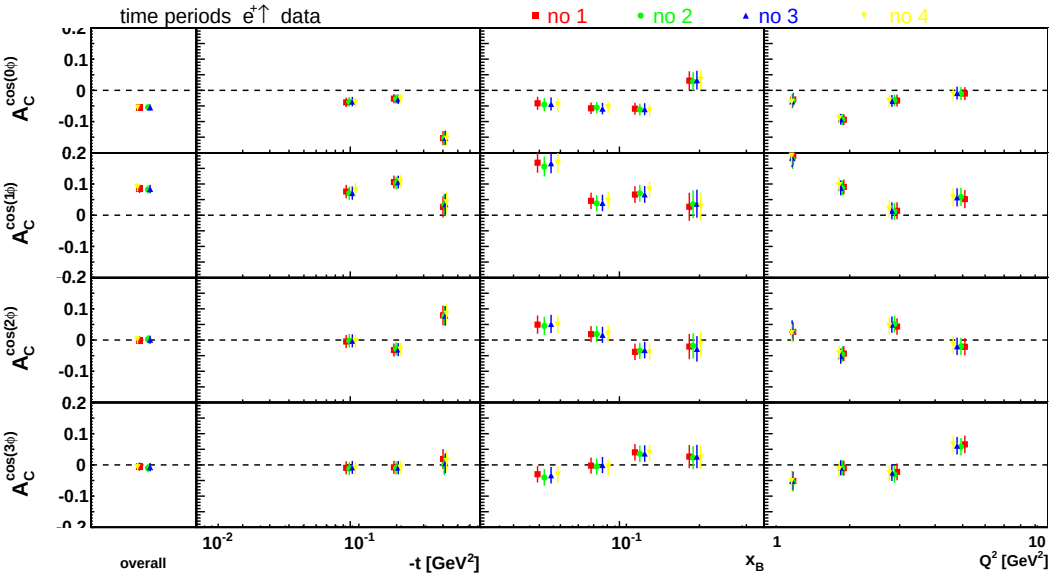

Figure 5.5.6: Time period 10, under exclusion of one of the first 4 parts.

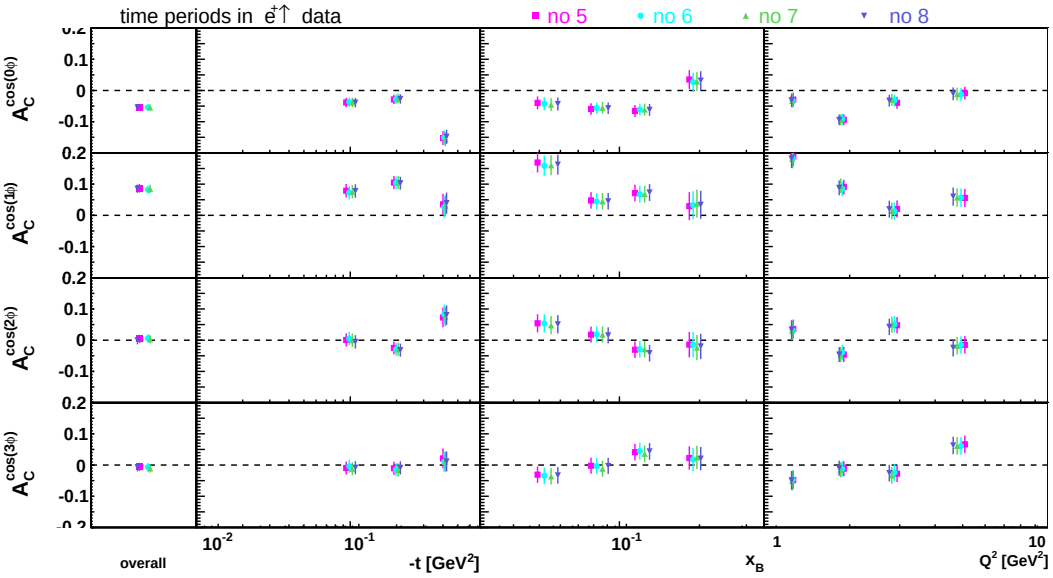

Figure 5.5.7: Time period 10, under exclusion of one of the last 4 parts.

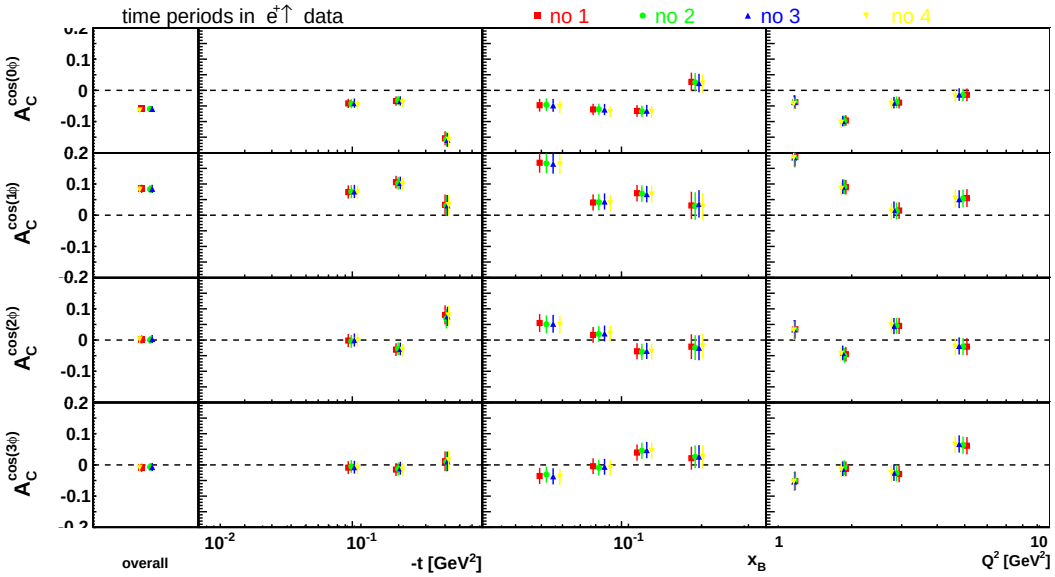

Figure 5.5.8: Time period 11 and 12, under exclusion of the one of the first 4 parts.

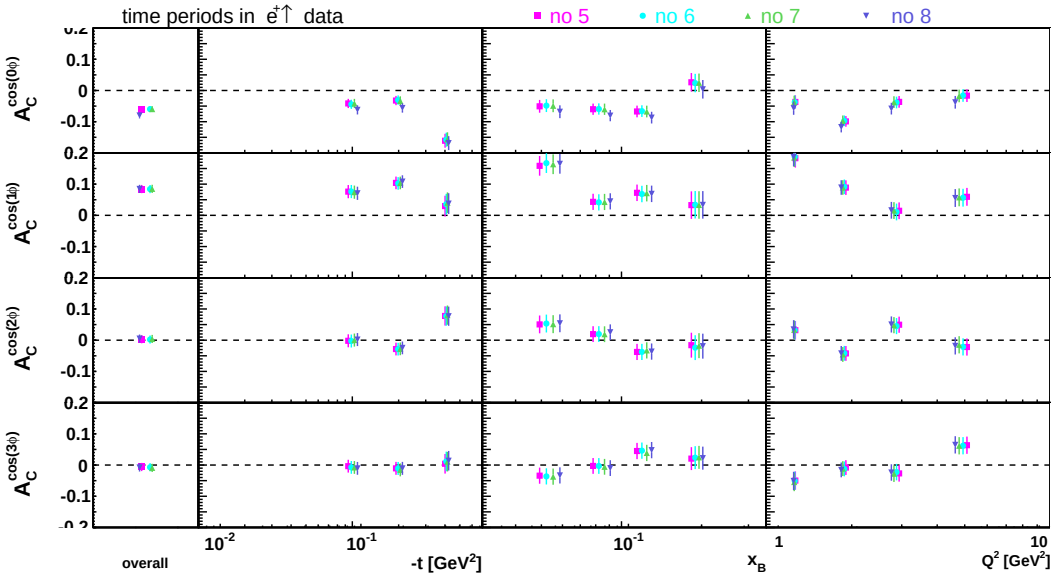

Figure 5.5.9: Time period 11 ans 12, under exclusion of the one of the last 4 parts.

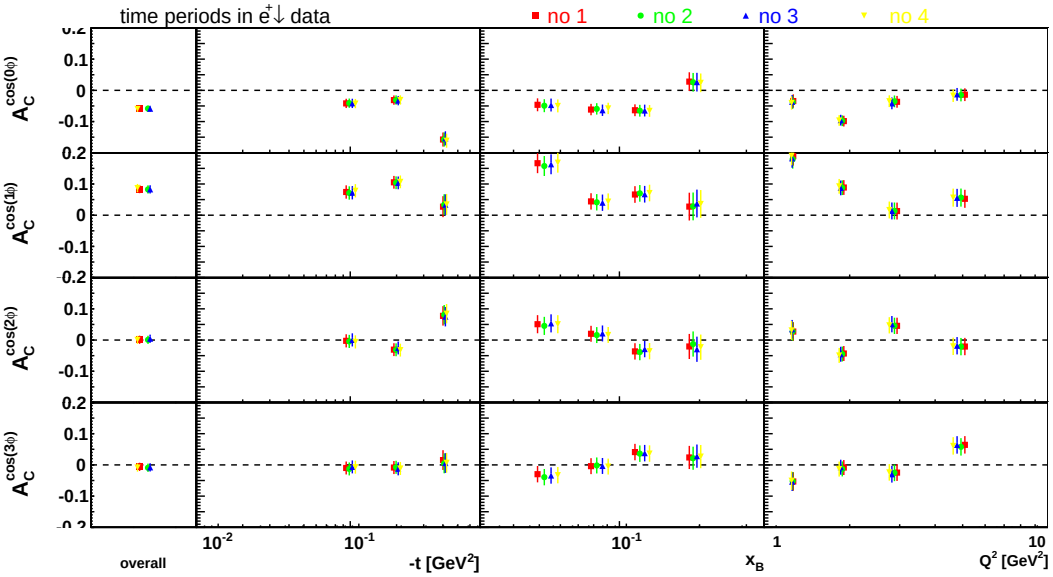

Figure 5.5.10: Time period 16, under exclusion of one of the first 4 parts.

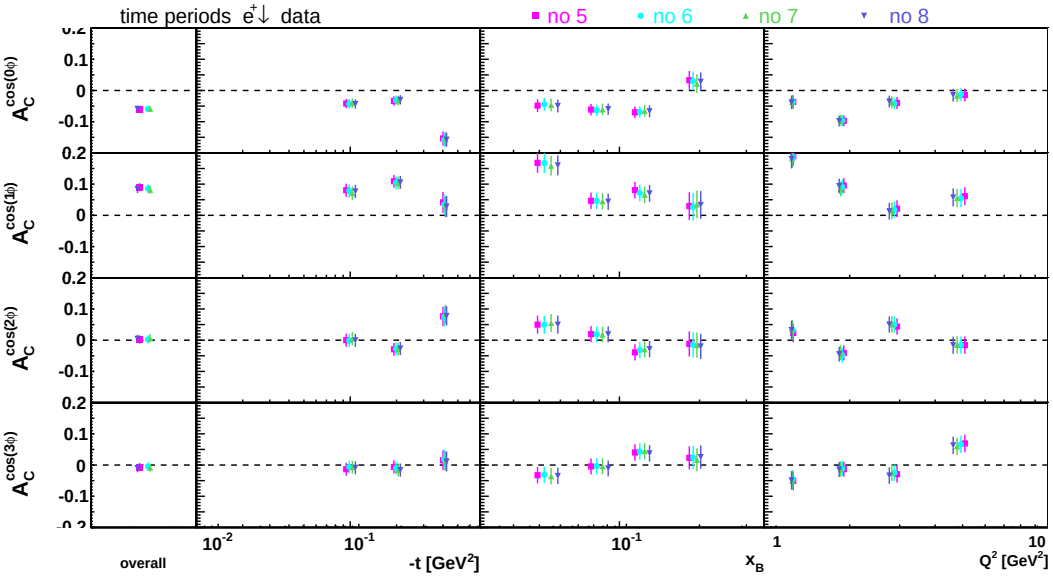

Figure 5.5.11: Time period 16, under exclusion of one of the last 4 parts.

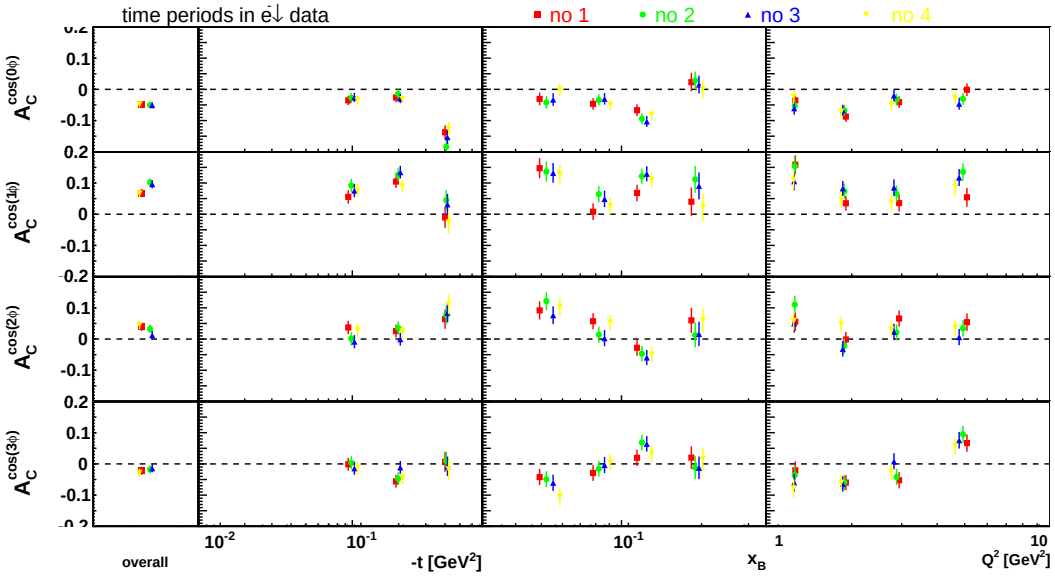

Figure 5.5.12: Time period 2, 4 and 6, under exclusion of the one of the first 4 parts.

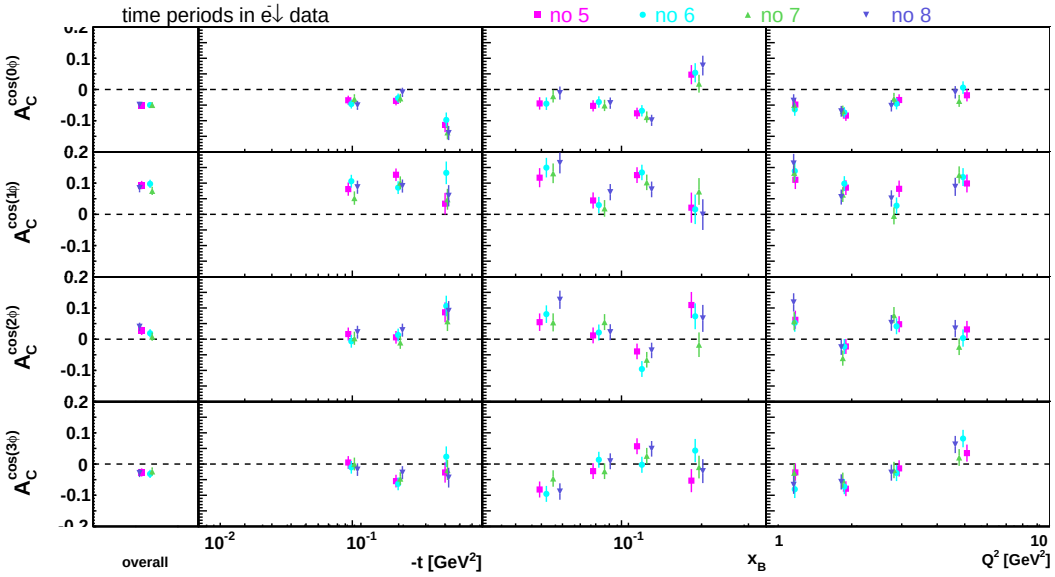

Figure 5.5.13: Time period 2, 4 and 6, under exclusion of one of the last 4 parts.

5.5.3 *Detailed analysis of time period 6*

A final test was done to disapprove the time stability of the electron data. Time period 6 in 4.5.1 which provides the essential data for the analysis was divided in 4 parts of equal size. The BCA fit was performed using all positron data but only one of the 4 electron data subsets receiving resulting in 4 half independent data sets. Figure 5.5.14 on page 92 shows the pure data sample, Figure 5.5.15 on page 92 the reference data sample and Figure 5.5.16 on page 93 the unresolved data sample. All

three samples show an inconsistent behavior that can not only be attributed to the low electron statistics. Also one of the time periods sticks out in the pure data sample. Part 3 of time period 6 in the pure sample shows a very low $A_C^{\cos(\phi)}$ overall value.

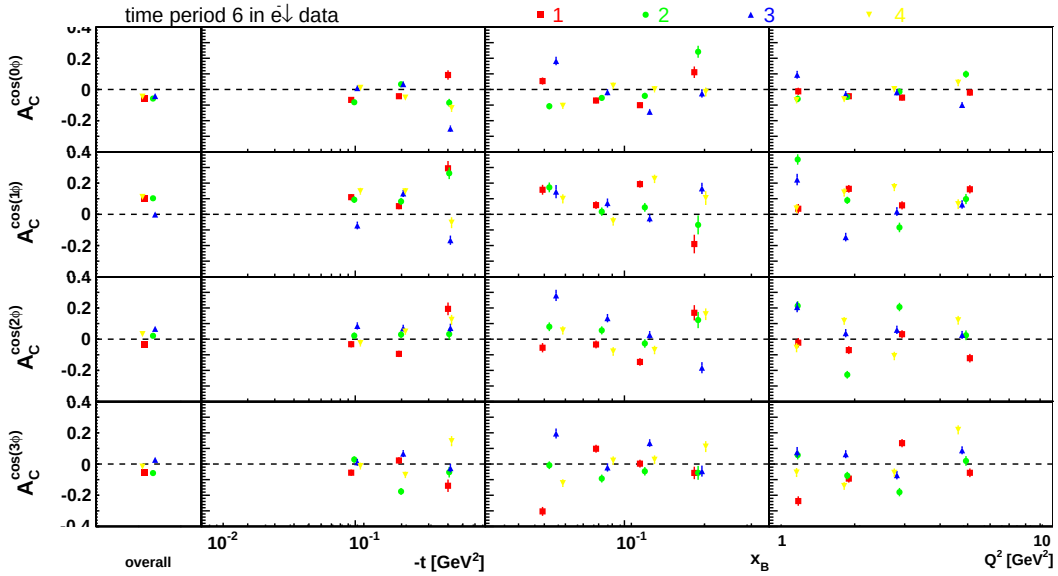

Figure 5.5.14: BCA with one quarter of time period 6 for electron data and the total set of positron data in the pure data sample

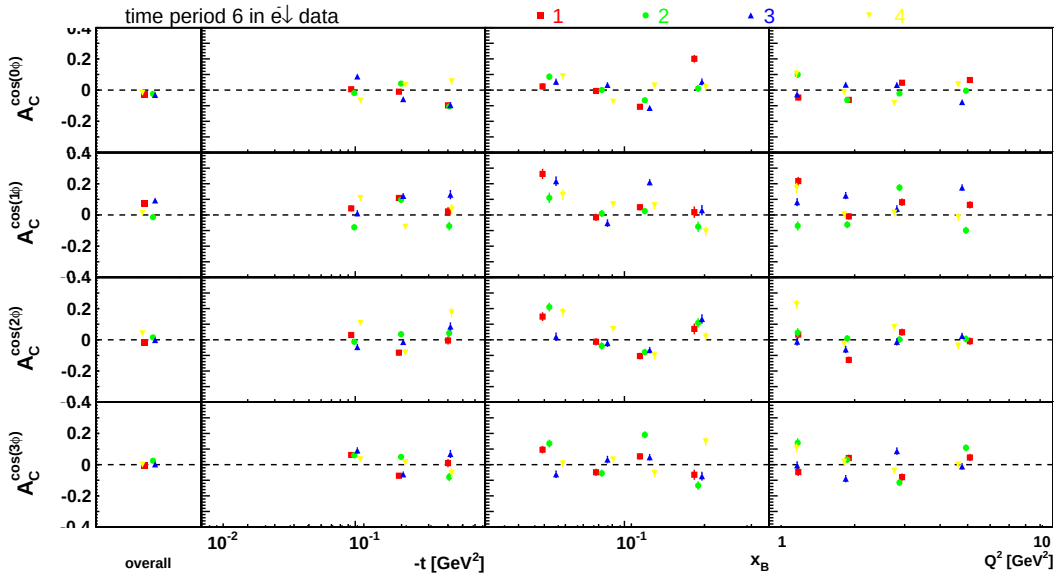

Figure 5.5.15: BCA with one quarter of time period 6 for electron data and the total set of positron data in the reference data sample

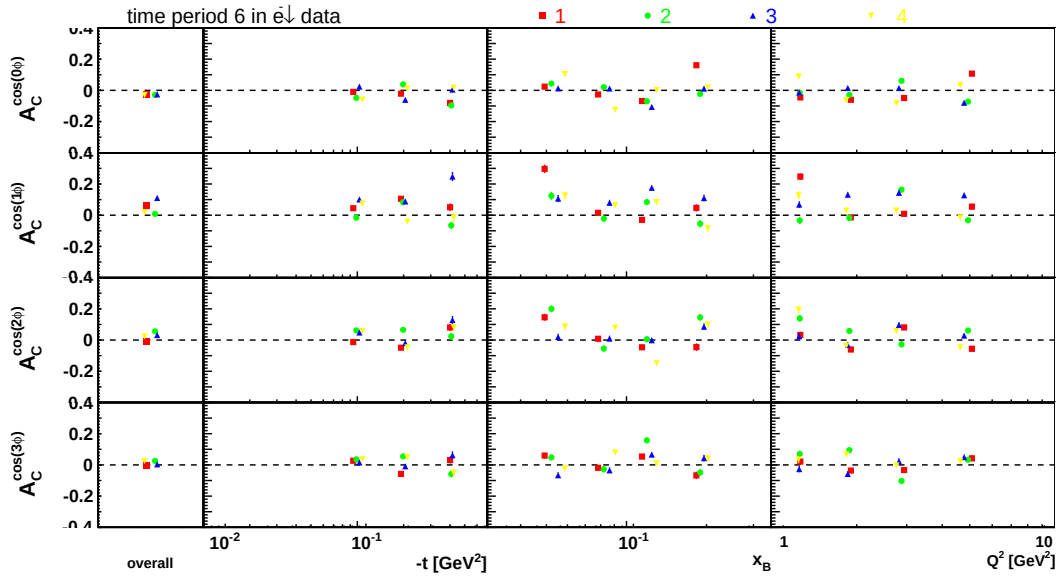

Figure 5.5.16: BCA with one quarter of time period 6 for electron data and the total set of positron data in the unresolved data sample

The instability that was already visible in section 5.5.2 has turned out a major problem that is not only restricted to the recoil detector. It needs to be attributed to time instabilities in the forward detector that could not be solved and are barely explained yet. The deviations of the different time periods will be quantified in an additional systematic error in section 6.

5.6 ADDITIONAL TERMS IN THE FIT

To find hints to what is wrong in the electron data the influence of sine harmonics in the fit is studied. The fit was extended by the sine harmonics $A_C^{\sin(\phi)}\sin(\phi)$ and $A_C^{\sin(2\phi)}\sin(2\phi)$ to:

$$\begin{aligned} A_C &= A_C^{\cos(0\phi)} + A_C^{\cos(\phi)}\cos(\phi) + A_C^{\cos(2\phi)}\cos(2\phi) + A_C^{\cos(3\phi)}\cos(3\phi) \\ &+ A_C^{\sin(\phi)}\sin(\phi) + A_C^{\sin(2\phi)}\sin(2\phi) \end{aligned}$$

Even though the fits are extended to 6 and 15 parameters they will be labeled 4 and 13 parameter fit for better clarity.

The following pictures show the sine harmonics in the 4 parameter fit in comparison between the three data samples: Figure 5.6.2 on page 94 with and Figure 5.6.1 on page 94 without the first t_c bin. From these plots a conspicuous behavior in the $\sin(\phi)$ term in the Q^2 dependence appears in all three data samples. Especially in the pure data sample the $A_C^{\sin(\phi)}$ value is unexpectedly high. In a plot without the lowest t_c bin, the reference data sample closes up to it. Still the distribution of t_c values does not seem to be a complete explanation. Comparing the 4 parameter fit to the 13 parameter fit (5.6.3) we see that the raise in the second Q^2 bin is less significant there.

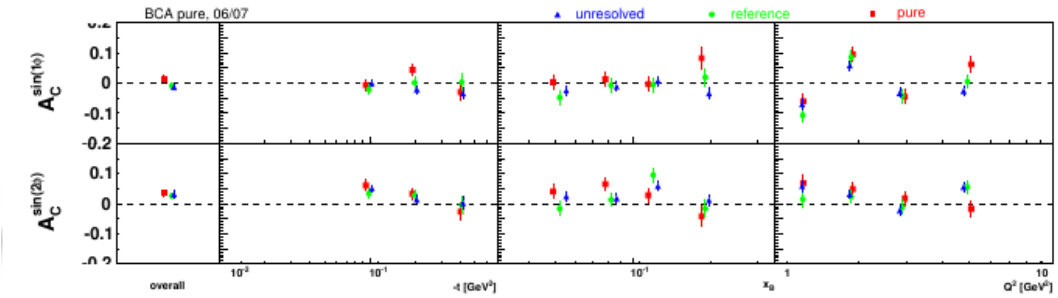

Figure 5.6.1: Sin harmonic terms in the 3 data samples without lowest t_c bin. All three data sets are cut to the same time period.

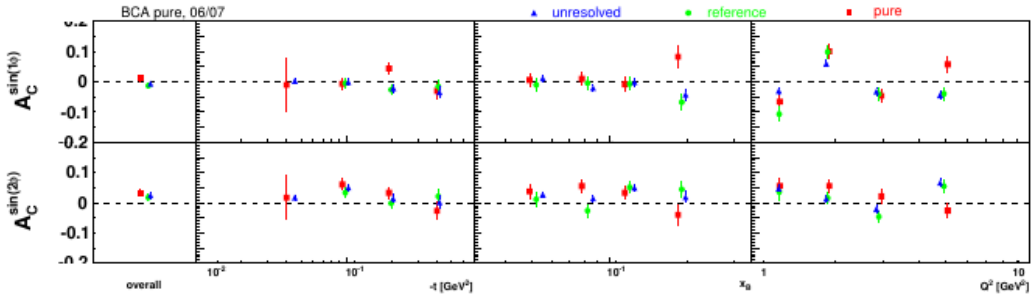

Figure 5.6.2: Sin harmonic terms in the 3 data samples with lowest t_c bin. All three data sets are cut to the same time period.

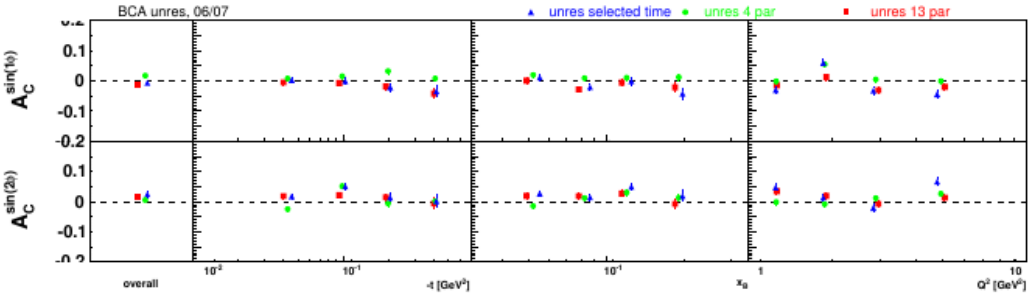

Figure 5.6.3: Sine harmonic terms in the unresolved data sample. Unresolved complete data sample in a 13 parameter fit with additional sine terms (red), unresolved complete data sample in a 4 parameter fit with additional sine terms (green) the same fit with the time periods selected in the pure data sample (blue).

5.7 INFLUENCE ON PUBLISHED RESULTS

The time instability not only affects the results of this study. Also already published asymmetries are influenced by the results of the last subsections. In the Hermes publication of the beam-helicity and beam-charge asymmetries associated with deeply virtual Compton scattering on the unpolarized proton [21] that was released in 2012 (please see 3.1.2 for the original plot) the results extracted from 2006/2007 data deviate from BCA results of the precedent years. Figure 5.2.4 on page 79 has already shown that the BCA amplitudes could be reproduced in a cross check in this study. Now the data set used for the cross check was reduced by removing runs from time period 6 and earlier (all runs <10305 in 2006 where excluded). In Figure 5.7.1 on page 95 compares the comparison between published HERMES results with data before 2006, this studies results with the full data set and the reduced data set are compared. All samples where fit with the 13 parameter maximum likelihood fit. Especially in the highest t_c bin the reduced data sample closes up to the published data points but does not reach their values completely. This shows that the time instability plays a role in the deviation between 2006/2007 and 1996-2005 HERMES data.

The publication of Beam-helicity asymmetry arising from deeply virtual Compton scattering measured with kinematically complete event reconstruction of 2012 [23] is not affected by the time instability. Here only time periods 9 and higher where used that showed no irregularity in the time stability studies.

In future publications the beginning of the year 2006 should be excluded from the studies.

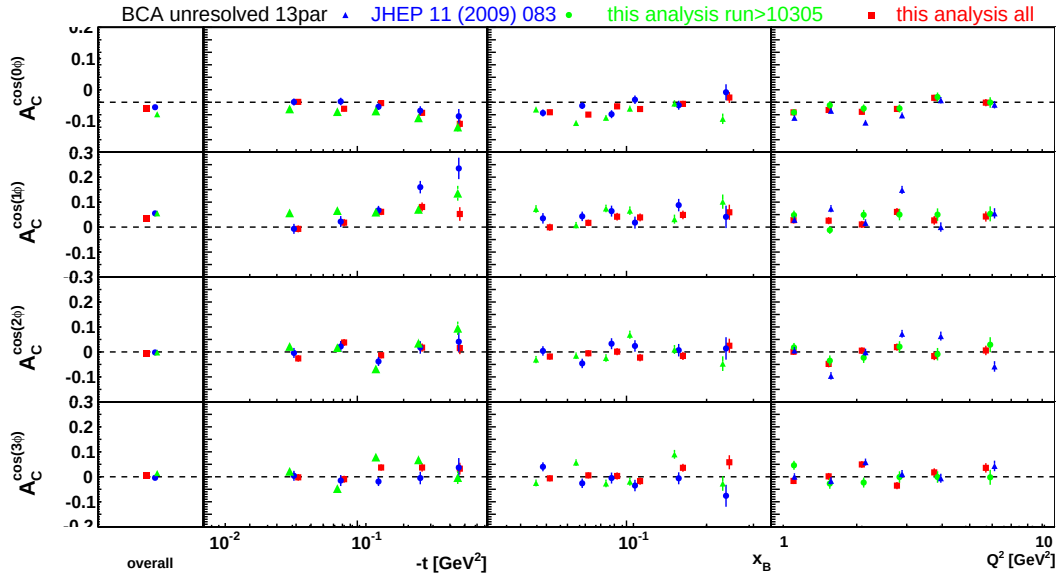

Figure 5.7.1: BCA fit with the 13 parameter fit. In comparison: Published data of the years 1996-2005 (blue), full data set of this study (red) and reduced dataset where all runs <10305 in 2006 where excluded (green). Reduced data set closes up to the published.

6

SYSTEMATIC STUDIES

6.1 3-IN-ONE SYSTEMATIC UNCERTAINTY

The uncertainties that dilute the DVCS/BH data sample arise from

1. background processes,
2. spectrometer acceptance and alignment of the forward spectrometer,
3. the recoil detector acceptance,
4. smearing and finite bin width.

These four uncertainties have been studied and quantified in the so called 4-in-1 method [52]. After the implementation of a new alignment file that allowed to eliminate the uncertainties related to misalignment this was reduced to a 3-in-1 approach.

The 3-in-1 systematic uncertainty is determined using a Monte Carlo simulation and calculating the difference in the asymmetry between the generated events and the simulated measurement in the detector taking into account all 3 uncertainties..

The program qplot produces asymmetry amplitudes according to a simulation that calculates them directly from the Fourier coefficients and the 5 VGG [74, 62] models of GPDs.

The 5 different VGG models combine the t-ansatz, skewness, b parameter and D term in different ways as summarized in 6.1.1.

qplot gives the asymmetry amplitudes according to the average $-t$, x_B and Q^2 of each bin. They are free from any detector effects.

Model	Factorized t-ansatz	Skewness	b Parameter	D-term
1	factorized	none	b$\rightarrow\infty$	none
2	factorized	included	b=1	none
3	factorized	included	b=3	none
4	factorized	included	b=1	included
5	factorized	included	b=3	included

Table 6.1.1: Contributions of the factorized t-ansatz, skewness, b parameter and D-Term to each VGG model. The b-parameter is only valid for models that include the Radyushkin double-distribution profile formula. If skewness is included it comes from the double-distribution formalism.

A set of MC events is generated with gmcDVCS and propagated through a simulation of the forward spectrometer and recoil detector. The asymmetries extracted from these reconstructed events are subtracted from the values calculated by qplot:

$$\delta^{\text{mod}}_{3-\text{in}-1,\text{sys}} = \mid A_{\text{qplot}} - A_{\text{reconstructed}} \mid \tag{6.1.1}$$

The final 3-in-1 systematic uncertainty is the RMS value

$$\delta_{3-\text{in}-1,\text{sys}} = \sqrt{\frac{1}{5}\sum_{i=1}^{5}(\delta^{i}_{3-\text{in}-1})^2} \tag{6.1.2}$$

obtained from all five VGG type models. These values can be found in table 6.1.2. They are also shown in 6.1.1.

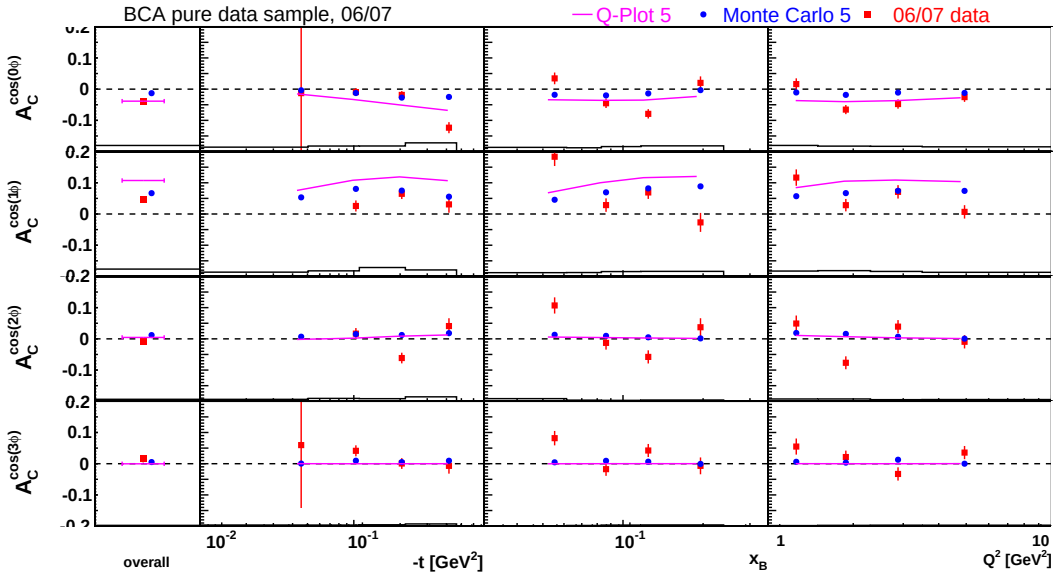

Figure 6.1.1: The 3-in-1 results for the pure BCA. In each kinematic bin, the calculated curve (qplot) and the Monte Carlo asymmetry amplitudes reconstructed with method 3. The black solid line marks the systematic error.

After exclusion of the first t_c bin the fit and error values change as shown in 6.1.3 and the fit can be viewed in 6.1.2

6.2 BACKGROUND

In the previous DVCS analyses, it has been shown that the most significant background for the selection of DVCS/BH events comes from so-called "associated production", where the target proton is exited to a Δ resonance, Semi-Inclusive Deep Inelastic Scattering (SIDIS) producing π^0 and η mesons, and hard exclusive production of π^0. The kinematically complete event reconstruction allowed to suppress this background to a negligible level. Especially the production of the exclusive neutral pions is suppressed that much [38] that it will be neglected as a background channel here.

In order to estimate the fraction of events in the data contributing to each process , the following studies were performed.

	$A_C^{\cos(0\phi)}$	$\delta_{stat}^{A_C^{\cos(0\phi)}}$	$\delta_{sys}^{A_C^{\cos(0\phi)}}$	$A_C^{\cos(\phi)}$	$\delta_{stat}^{A_C^{\cos(\phi)}}$	$\delta_{sys}^{A_C^{\cos(\phi)}}$	$A_C^{\cos(2\phi)}$	$\delta_{stat}^{A_C^{\cos(2\phi)}}$	$\delta_{sys}^{A_C^{\cos(2\phi)}}$	$A_C^{\cos(3\phi)}$	$\delta_{stat}^{A_C^{\cos(3\phi)}}$	$\delta_{sys}^{A_C^{\cos(3\phi)}}$
all	-0.056	0.009	0.015	0.089	0.013	0.011	0.008	0.013	0.008	-0.005	0.013	0.003
$0 \leq -t_c < 0.06$	0.124	0.061	0.037	0.064	0.079	0.040	-0.224	0.082	0.012	0.108	0.071	0.027
$0.06 \leq -t_c < 0.14$	-0.033	0.015	0.014	0.075	0.021	0.047	0.015	0.020	0.013	-0.005	0.020	0.003
$0.14 \leq -t_c < 0.3$	-0.046	0.014	0.013	0.109	0.020	0.017	-0.013	0.019	0.009	-0.017	0.020	0.005
$0.3 \leq -t_c < 0.7$	-0.163	0.022	0.019	0.025	0.032	0.016	0.063	0.030	0.016	0.023	0.030	0.008
$1 \leq q^2 < 1.5$	-0.023	0.020	0.016	0.175	0.028	0.020	0.045	0.028	0.019	-0.005	0.028	0.010
$1.5 \leq q^2 < 2.3$	-0.084	0.016	0.012	0.102	0.022	0.013	-0.033	0.023	0.010	0.010	0.023	0.003
$2.3 \leq q^2 < 3.5$	-0.046	0.018	0.013	0.041	0.026	0.007	0.006	0.025	0.006	-0.020	0.025	0.004
$3.5 \leq q^2 < 10$	-0.041	0.019	0.014	0.054	0.028	0.005	0.003	0.027	0.008	0.024	0.026	0.005
$0.03 \leq x_B < 0.07$	-0.031	0.019	0.009	0.166	0.029	0.017	0.070	0.027	0.046	-0.011	0.025	0.006
$0.07 \leq x_B < 0.1$	-0.053	0.017	0.007	0.067	0.025	0.012	0.029	0.024	0.017	0.027	0.024	0.002
$0.1 \leq x_B < 0.15$	-0.071	0.018	0.008	0.084	0.025	0.006	-0.041	0.025	0.010	0.013	0.025	0.005
$0.15 \leq x_B < 0.35$	-0.012	0.028	0.014	0.063	0.041	0.006	-0.003	0.038	0.030	-0.011	0.035	0.010

Table 6.1.2: Beam Charge Asymmetry Amplitudes with statistic and systematic error. δ_{sys} mean the 3-in-1 systematic uncertainty $\delta_{3-\text{in}-1,\text{sys}}$. These results where produced including the lowest t_c bin.

	$A_C^{\cos(0\phi)}$	$\delta_{stat}^{A_C^{\cos(0\phi)}}$	$\delta_{sys}^{A_C^{\cos(0\phi)}}$	$A_C^{\cos(\phi)}$	$\delta_{stat}^{A_C^{\cos(\phi)}}$	$\delta_{sys}^{A_C^{\cos(\phi)}}$	$A_C^{\cos(2\phi)}$	$\delta_{stat}^{A_C^{\cos(2\phi)}}$	$\delta_{sys}^{A_C^{\cos(2\phi)}}$	$A_C^{\cos(3\phi)}$	$\delta_{stat}^{A_C^{\cos(3\phi)}}$	$\delta_{sys}^{A_C^{\cos(3\phi)}}$
all	-0.062	0.009	0.018	0.087	0.013	0.014	0.013	0.013	0.009	-0.005	0.012	0.05
$0 \leq -t_c < 0.06$	-	-	-	-	-	-	-	-	-	-	-	-
$0.06 \leq -t_c < 0.14$	-0.033	0.015	0.016	0.075	0.021	0.008	0.015	0.020	0.013	-0.005	0.020	0.003
$0.14 \leq -t_c < 0.3$	-0.046	0.014	0.016	0.109	0.020	0.020	-0.013	0.019	0.009	-0.017	0.020	0.005
$0.3 \leq -t_c < 0.7$	-0.163	0.022	0.024	0.025	0.032	0.016	0.063	0.030	0.015	0.023	0.030	0.009
$1 \leq q^2 < 1.5$	-0.017	0.021	0.018	0.193	0.030	0.024	0.050	0.030	0.027	-0.025	0.029	0.011
$1.5 \leq q^2 < 2.3$	-0.096	0.017	0.014	0.092	0.023	0.056	-0.031	0.024	0.010	0.004	0.023	0.001
$2.3 \leq q^2 < 3.5$	-0.055	0.018	0.015	0.024	0.026	0.081	0.053	0.025	0.0159	-0.008	0.025	0.005
$3.5 \leq q^2 < 10$	-0.041	0.019	0.015	0.065	0.028	0.099	0.008	0.027	0.023	0.020	0.027	0.005
$0.03 \leq x_B < 0.07$	-0.033	0.020	0.011	0.168	0.032	0.005	0.076	0.029	0.016	-0.014	0.024	0.006
$0.07 \leq x_B < 0.1$	-0.066	0.018	0.008	0.059	0.026	0.005	0.028	0.025	0.003	0.021	0.023	0.003
$0.1 \leq x_B < 0.15$	-0.070	0.018	0.008	0.081	0.026	0.004	-0.030	0.026	0.003	0.026	0.023	0.007
$0.15 \leq x_B < 0.35$	0.020	0.028	0.015	0.065	0.042	0.008	-0.001	0.038	0.004	-0.013	0.033	0.011

Table 6.1.3: Beam Charge Asymmetry Amplitudes with statistic and systematic error. δ_{sys} mean the 3-in-1 systematic uncertainty $\delta_{3-\text{in}-1,\text{sys}}$. These results where produced excluding the lowest t_c bin.

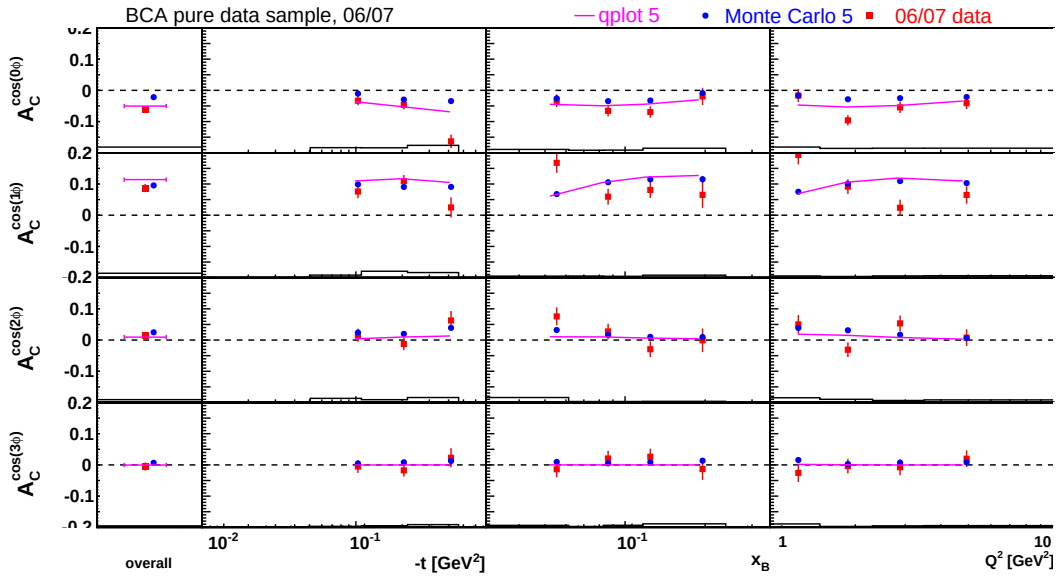

Figure 6.1.2: The 3-in-1 results for the pure BCA. In each kinematic bin, the calculated curve (qplot) and the Monte Carlo asymmetry amplitudes reconstructed with method 3 without the lowest t_c bin. The black solid line marks the systematic error.

ESTIMATION OF PROCESS FRACTIONS

Two Monte Carlo generators were used to simulate the background processes: gmcDVCS (no. 054) [52] for elastic and associated BH processes and DISng (no. 057) for the SIDIS processes. A particular process was identified in the corresponding event generator using the following selection criteria:

- Bethe-Heitler and DVCS

  g1MEvent.XTrue=1 in gmcDVCS,

- Associated Bethe-Heitler

  g1MEvent.XTrue<1 and g1MEvent.W2True <4 in gmcDVCS,

- Semi Inclusive Deep Inelastic Scattering

  (g1MEvent.bProcess<4&0xFF)=1 in DISng.

The reconstructed event data is then analyzed in order to understand which events would pass the analysis sample.

Information on the yield in each kinematic bin needs to be used to estimate the fractions of the data coming form the different processes. To satisfy this, an event weight that is the process yield normalized to the yield of DIS events is stored in the MC uDST files. The fractional contribution to the yield is calculated as:

$$f_{\text{process}} = \frac{\sum_i^{N_{\text{process}}} w_i}{\sum_i^{N_{\text{total}}} w_i}, \tag{6.2.1}$$

where w_i is the MC event weight of a process event, i and $N_{\text{process}} \in [\text{DVCS}, \text{Associated BH}, \text{SIDIS}]$ and N_{total} the total number of selected events.

This analysis gives 98.89% of the pure elastic event sample to be from BH/DVCS elastic events, <0.1% from SIDIS and 1.01% from associated BH events for the method 3 data sample.

Corrections to the asymmetry amplitudes for background

It is not possible to correct the asymmetry amplitudes for the influence of associated production since there is no reliable model of a beam charge asymmetry in associated production. The contamination by SIDIS events is considered to be too small to have an effect. For this reason no background correction on BCA was applied.

6.3 TIME DEPENDENCE UNCERTAINTY

To take into account the time inconsistent electron data the only possibility is to include the delusion in the systematic error. This error is calculated from Figure 5.5.14 on page 92. The average of the four points is calculated weighted by the statistical errors. This way the average is estimated as:

$$A_{c,av}^{\cos(i\phi)} = \frac{\sum_{j=1}^{4} A_{c,j}^{\cos(i\phi)} \cdot dA_{c,j}^{\cos(i\phi)}}{\sum_{i=1}^{4} dA_{c,j}^{\cos(i\phi)}} \tag{6.3.1}$$

Then the maximum error is chosen as the largest difference of one of the 4 fit values and this average value:

$$\Delta A_{c,av}^{\cos(i\phi)} = max\{\mid A_{c,j}^{\cos(i\phi)} - A_{c,av}^{\cos(i\phi)} \mid\}_j \tag{6.3.2}$$

It has been added to the 3-in-one systematic error.

6.4 SUMMARY OF SYSTEMATICS

The total systematic uncertainty is considered to be equal to the 3-in-1 uncertainty of the measurement, as no background correction is applied here. No systematic uncertainty due to the previously found time dependence of the DVCS yield in the 2006/2007 data set is applied because in the data productions used, this time dependence has been eliminated by correcting calorimeter pedestals in a certain time period.

6.5 SYSTEMATIC ERRORS FOR THE UNRESOLVED AND REFERENCE DATA SAMPLE

The 3-in-1 uncertainties are calculated in the same way for the reference (6.5.1) and unresolved (6.5.2) data sample in the same way. The plots of the time dependence uncertainties is shown in Figure 6.5.3 on page 104 and Figure 6.5.4 on page 105. From these plots it is clear how dominating that they are in these samples, too.

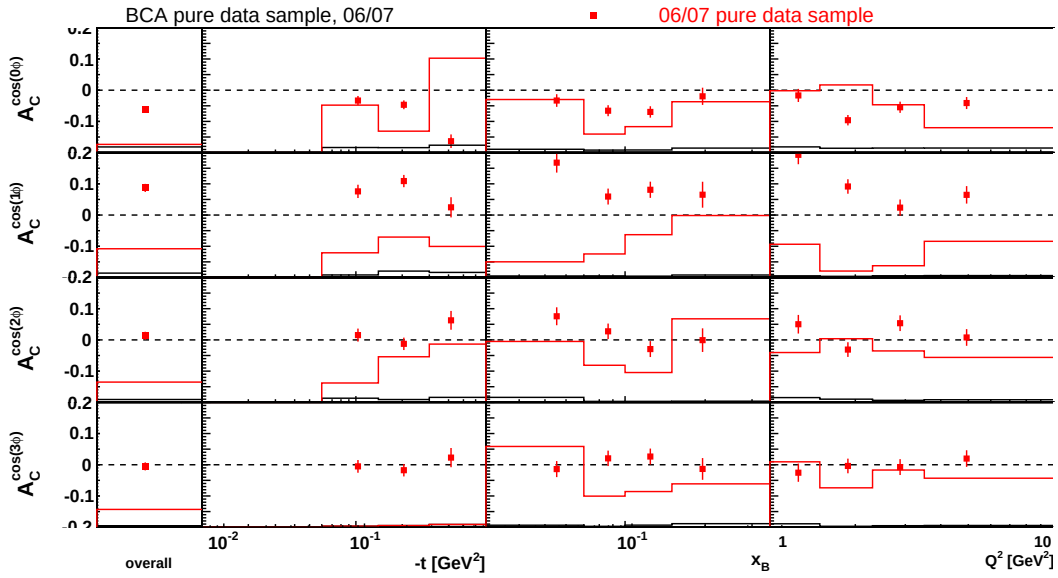

Figure 6.3.1: Pure BCA. without the lowest t_c bin. The black solid line marks the 3-in-1 systematic error. The red solid line marks the time dependence uncertainty the magnitude of this error overgrows systematic errors but also measured values.

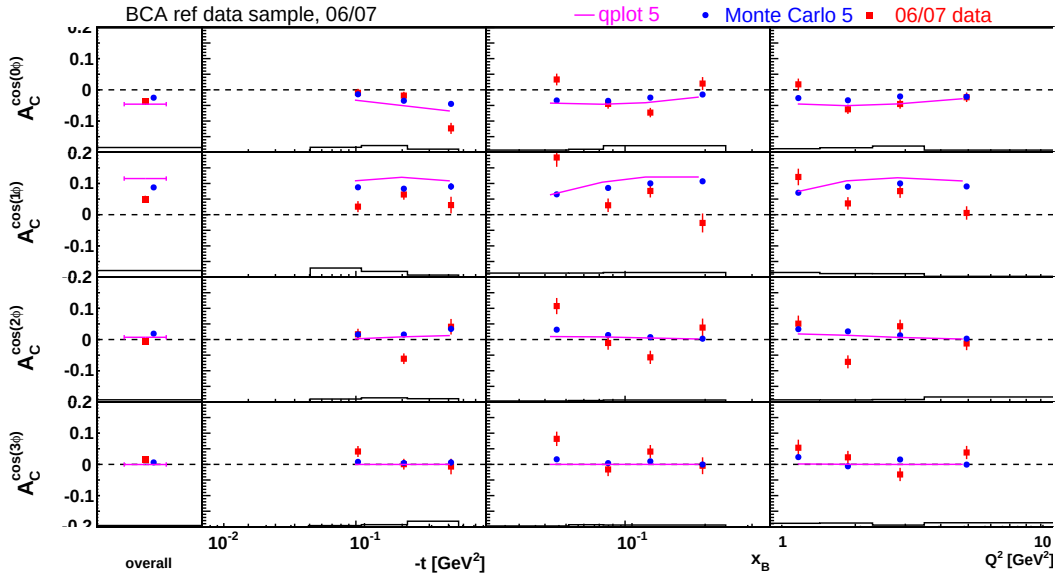

Figure 6.5.1: The 3-in-1 results for the reference BCA. In each kinematic bin, the calculated curve (qplot) and the Monte Carlo asymmetry amplitudes reconstructed with method 3 without the lowest t_c bin. The black solid line marks the systematic error.

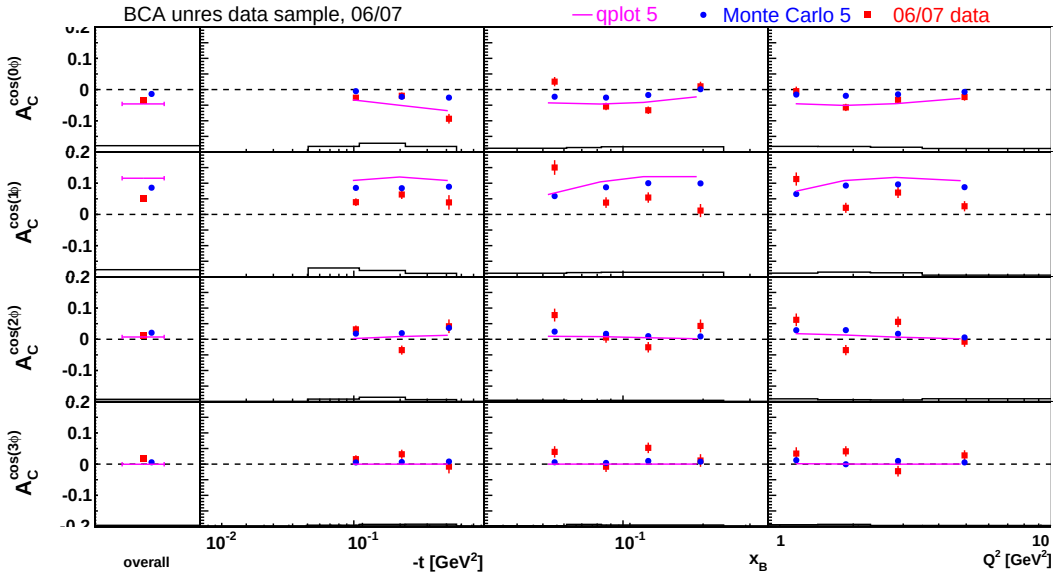

Figure 6.5.2: The 3-in-1 results for the unresolved BCA. In each kinematic bin, the calculated qplot curve (pink) and the Monte Carlo asymmetry amplitudes reconstructed with method 3 without the lowest t_c bin. The black solid line marks the systematic error.

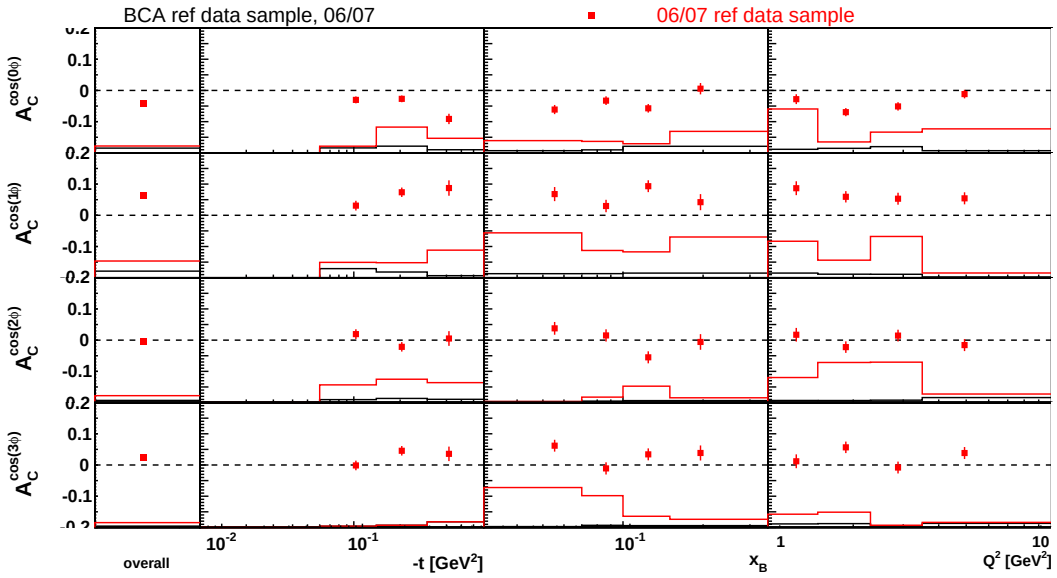

Figure 6.5.3: Reference BCA. without the lowest t_c bin. The black solid line marks the 3-in-1 systematic error. The solid red line marks the time dependence uncertainty.

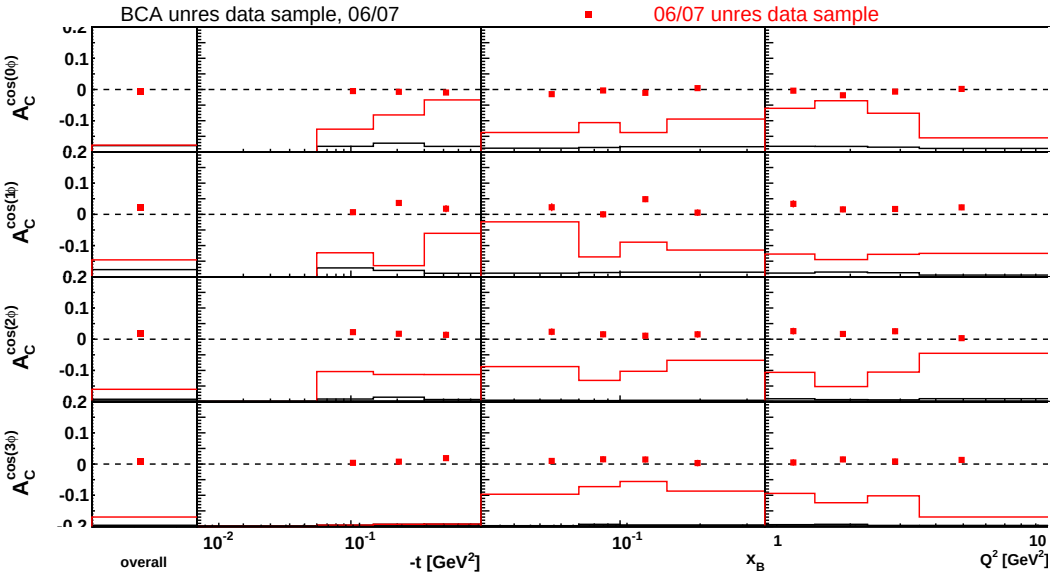

Figure 6.5.4: Unresolved BCA. without the lowest t_c bin. The black solid line marks the 3-in-1 systematic error. The solid red line marks the time dependence uncertainty.

7

CONCLUSION

This thesis has explained the theoretical fundamentals of DVCS analysis at Hermes. The connection between GPDs and asymmetries according to beam charge and helicity has been displayed.

The analysis was done by extracting DIS and DVCS data from the 06/07 data set applying data quality and data selection criteria. The recoil detector that was installed in 2006 adds information about the recoiling proton to the particle tracks recorded in the forward detector and allows a complete kinematic event reconstruction.

Extracting the BCA with recoil detector data adds several special challenges to data analysis. Not only is the data set taken with an electron beam is very small, also due to technical problems only parts of the recoil detector were functional. Only the scintillating fiber tracker can be used to reconstruct the path of the recoiling particle in the recoil detector, and one quarter of this detector turned out to be defective and tracks measured there where excluded from the analysis. Also only 3 combinations of beam and helicity were available in this data period. No positive polarized electron beam was available in the time period where the recoil detector gave valid data. For this reason the asymmetry fit method had to be changed from a simultaneous fit of BCA and BSA to a separate BCA fit.

Not all problems of the recoil detector data taking were marked in the data quality information of the events and enforced a manual time period selection.

While the use of only scintillating fiber tracker for the track reconstruction and the separate BCA fit method could be validated in this thesis the main analysis problem turned out to come not from the recoil detector itself.

One of the main conclusions that can be drawn from this analysis is a hint to what may have caused the odd behavior in the Hermes publication of A_C from the unresolved data sample [21]. Figure 5.7.1 on page 95 shows that an exclusion of the beginning of year 2006 data changes the BCA and closes up to the BCA results of 1996-2005 the to Figure 5.5.16 on page 93. The time instability contributes especially to the unexpectedly high $A_C^{\cos\phi}$ values in the higher t_c bins of the publication that were registered in the publication and were at the border of the systematic uncertainties. The time instability was shown not to be a recoil detector problem but also affects the forward detector.

The publication of Beam-helicity asymmetry arising from deeply virtual Compton scattering measured with kinematically complete event reconstruction of 2012 [23] is not affected by the instability.

The three data samples (pure, reference and unresolved) were consisted for the chosen time periods as demonstrated in Figure 5.4.2 on page 82.

Still the data instability of the crucial time period that provided electron data prevented a reliable extraction of BCA with a kinematically complete data set. The quantification of the uncertainties from the time instability in Figure 6.3.1 on page 103 shows that they are not only much higher then the systematic errors but also then the BCA values.

Nevertheless this thesis showed in Chapter 5 the usability of method 3 and also the possibility of a 4 parameter fit where an 13 parameter fit was not possible. These results can affect ongoing HERMES studies and help to explain open questions in published ones.

Part IV

APPENDIX

A

APPENDIX

A.1 SHORT EXCURSION TO WILSON LINES

A two particle state as a quark and anti-quark at different space time points x and y. This state is not gauge invariant. It transforms as

$$\overline{\psi(y)}\psi(x) \to \overline{\psi(y)}\Omega^{-1}(x)\Omega(y)\psi(x) \tag{A.1.1}$$

under a local gauge transformation $\Omega(x) \in SU(3)$. So there is an object $U_\gamma(y,x)$ needed that transforms as

$$U_\gamma(y,x) \to \Omega(y)U_\gamma(y,x)\Omega^{-1}(x) \tag{A.1.2}$$

in order to form a gauge invariant state called Wilson line:

$$\overline{\psi(y)}U_\gamma(y,x)\psi(x) \tag{A.1.3}$$

$U_\gamma(y,x)$transports some path γ connecting x and y.

For a family of orthonormal basis $|\psi^a(x)\rangle$ there is

$$\langle\psi_b^*(x)|\psi^a(x)\rangle = \delta_b^a \tag{A.1.4}$$

it follows

$$\langle\partial\psi_b^*(x)|\psi^a(x)\rangle + \langle\psi_b^*(x)|\partial\psi^a(x)\rangle = 0 \tag{A.1.5}$$

obviously the hermetian part disappears but the antihermetian part doesn't automatically. If we impose:

$$0 = \langle\psi_b^*(x)|D_\mu\psi^a(x)\rangle = \langle\partial\psi_b^*(x)|\psi^a(x)\rangle + \langle\partial\psi_b^*(x)|\text{correction}^a(x)\rangle \tag{A.1.6}$$

$$|\text{correction}^a(x)\rangle = igA_{\mu c}^a\psi^c(x)\rangle \tag{A.1.7}$$

which leads to the transport equation:

$$
\begin{aligned}
&(\partial_\mu + igA_\mu(x))\psi(x) = 0 \\
&\qquad \Rightarrow \partial_\mu \psi(x) = -igA_\mu(x)\psi(x) \qquad \gamma(0) = x, \gamma(t) = y \\
&\psi(x(t)) = \psi(x(0)) - ig\int_0^t \mathrm{ds}\frac{\mathrm{d\bar{x}(s)}}{\mathrm{ds}} A_\mu(x(s))\psi(x(s)) \\
&\qquad \text{summ over n paths} \Rightarrow \\
&\psi(x(t)) = \psi(x(0)) - ig\int_0^t \mathrm{ds_1}\frac{\mathrm{d\bar{x}^1(s_1)}}{\mathrm{ds_1}} A_\mu(x(s_1))\psi(x(s)) \\
&\qquad + \ldots + (-ig)^{n+1}\int_0^t \mathrm{ds_1}\ldots\int_0^t \mathrm{ds_{n+1}}\frac{\mathrm{d\bar{x}^1(s_1)}}{\mathrm{ds_1}} A_{\mu_1}(x(s_1)) \\
&\qquad \ldots \frac{\mathrm{d\bar{x}^{n+1}(s_{n+1})}}{\mathrm{ds}_{n+1}} A_{\mu_{n+1}}(x(s_{n+1}))\psi(x(s))
\end{aligned}
$$

Now introduce the path ordering operation

$$
\begin{gathered}
\mathcal{P}\left[A_{\mu_1}(x(s_1))\ldots A_{\mu_n}(x(s_n))\right] = \\
\sum_{\pi\in S_n} \Theta(s_{\pi(1)},\ldots,s_{\pi(n)}) A_{\mu_{\pi(1)}}(x(s_{\pi(1)}))\ldots A_{\mu_{\pi(n)}}(x(s_{\pi(n)}))
\end{gathered}
$$

θ:Heaviside step function

$$
\psi(x(t)) = U_\gamma(x(t), x(0))\psi(x(0)) \tag{A.1.8}
$$

where for $\lim_{n\to\infty}$

$$
U_\gamma(x(t), x(0)) = P\exp[-ig\int_\gamma \mathrm{d\bar{x}} A_\mu(x)] \tag{A.1.9}
$$

BIBLIOGRAPHY

[1] *Fast Switching Pockels Cell Driver for SLR Laser System*, 12 October 2008. (Cited on page 37.)

[2] K. Ackerstaff et al. The hermes spectrometer. *Nucl. Instr. Meth. A"*, 417(2–3):230–265, 1998. (Cited on pages 25 and 40.)

[3] Christine A. Aidala, Steven D. Bass, Delia Hasch, and Gerhard K. Mallot. The Spin Structure of the Nucleon. *Rev.Mod.Phys.*, 85:655–691, 2013. (Cited on page 30.)

[4] A. Airapetian et al. Evidence for a single-spin azimuthal asymmetry in semi-inclusive pion electroproduction. *Phys. Rev. Lett.*, 84:4047–4051, May 2000. (Cited on pages 25 and 27.)

[5] A. Airapetian et al. Single-spin azimuthal asymmetries in electroproduction of neutral pions in semi-inclusive deep-inelastic scattering. *Phys. Rev. D*, 64:097101, Oct 2001. (Cited on pages 25 and 27.)

[6] A. Airapetian et al. Measurement of single spin azimuthal asymmetries in semi-inclusive electroproduction of pions and kaons on a longitudinally polarized deuterium target. *Phys.Lett.*, B562:182–192, 2003. (Cited on pages 25 and 27.)

[7] A. Airapetian et al. Flavor decomposition of the sea-quark helicity distributions in the nucleon from semiinclusive deep inelastic scattering. *Phys. Rev. Lett.*, 92:012005, Jan 2004. (Cited on page 25.)

[8] A. Airapetian et al. Quark helicity distributions in the nucleon for up, down, and strange quarks from semi-inclusive deep-inelastic scattering. *Phys. Rev. D*, 71:012003, Jan 2005. (Cited on pages 25 and 27.)

[9] A. Airapetian et al. Beam-charge azimuthal asymmetry and deeply virtual compton scattering. *Phys. Rev. D*, 75:011103, Jan 2007. (Cited on page 26.)

[10] A. Airapetian et al. Precise determination of the spin structure function g_1 of the proton, deuteron, and neutron. *Phys. Rev. D*, 75:012007, Jan 2007. (Cited on page 26.)

[11] A. Airapetian et al. Evidence for a Transverse Single-Spin Asymmetry in Leptoproduction of pi+pi- Pairs. *JHEP*, 0806:017, 2008. (Cited on pages 25 and 27.)

[12] A. Airapetian et al. Measurement of Azimuthal Asymmetries With Respect To Both Beam Charge and Transverse Target Polarization in Exclusive Electroproduction of Real Photons. *JHEP*, 0806:066, 2008. (Cited on page 26.)

[13] A. Airapetian et al. Measurement of Parton Distributions of Strange Quarks in the Nucleon from Charged-Kaon Production in Deep-Inelastic Scattering on the Deuteron. *Phys.Lett.*, B666:446–450, 2008. (Cited on page 26.)

[14] A. Airapetian et al. Observation of the naive-t-odd sivers effect in deep-inelastic scattering. *Phys. Rev. Lett.*, 103:152002, Oct 2009. (Cited on pages 25 and 27.)

[15] A. Airapetian et al. Separation of contributions from deeply virtual Compton scattering and its interference with the Bethe-Heitler process in measurements on a hydrogen target. *JHEP*, 0911:083, 2009. (Cited on page 26.)

[16] A. Airapetian et al. Effects of transversity in deep-inelastic scattering by polarized protons. *Phys.Lett.*, B693:11–16, 2010. (Cited on pages 25 and 27.)

[17] A. Airapetian et al. Leading-Order Determination of the Gluon Polarization from high-p(T) Hadron Electroproduction. *JHEP*, 1008:130, 2010. (Cited on page 26.)

[18] A. Airapetian et al. Single-spin azimuthal asymmetry in exclusive electroproduction of pi+ mesons on transversely polarized protons. *Phys.Lett.*, B682:345–350, 2010. (Cited on pages 25 and 27.)

[19] A. Airapetian et al. Measurement of azimuthal asymmetries associated with deeply virtual compton scattering on a longitudinally polarized deuterium target. *Nuclear Physics B*, 842(3):265 – 298, 2011. (Cited on page 26.)

[20] A. Airapetian et al. Measurement of double-spin asymmetries associated with deeply virtual Compton scattering on a transversely polarized hydrogen target. *Phys.Lett.*, B704:15–23, 2011. (Cited on page 26.)

[21] A. Airapetian et al. Beam-helicity and beam-charge asymmetries associated with deeply virtual compton scattering on the unpolarised proton. *JHEP*, 1207:032, 2012. (Cited on pages 26, 29, 76, 95, and 107.)

[22] A. Airapetian et al. Beam-helicity asymmetry arising from deeply virtual compton scattering measured with kinematically complete event reconstruction. *JHEP*, 1210:042, 2012. (Cited on pages 26, 53, and 76.)

[23] A. Airapetian et al. Beam-helicity asymmetry arising from deeply virtual Compton scattering measured with kinematically complete event reconstruction. *JHEP*, 1210:042, 2012. (Cited on pages 28, 95, and 107.)

[24] A. Airapetian et al. Azimuthal distributions of charged hadrons, pions, and kaons produced in deep-inelastic scattering off unpolarized protons and deuterons. *Phys.Rev.*, D87:012010, 2013. (Cited on pages 26 and 27.)

[25] A. Airapetian et al. Multiplicities of charged pions and kaons from semi-inclusive deep-inelastic scattering by the proton and the deuteron. *Phys.Rev.*, D87:074029, 2013. (Cited on pages 26 and 27.)

[26] J. Ashman et al. A Measurement of the Spin Asymmetry and Determination of the Structure Function g(1) in Deep Inelastic Muon-Proton Scattering. *Phys.Lett.*, B206:364, 1988. (Cited on page 7.)

[27] J. Ashman et al. An Investigation of the Spin Structure of the Proton in Deep Inelastic Scattering of Polarized Muons on Polarized Protons. *Nucl.Phys.*, B328:1, 1989. (Cited on page 7.)

[28] Roger Barlow. Extended maximum likelihood. *Nuclear Instruments and Methods in Physics Research Section A: Accelerators, Spectrometers, Detectors and Associated Equipment*, 297(3):496 – 506, 1990. (Cited on page 62.)

[29] Martin J. Bastiaans. Application of the wigner distribution function in optics. pages 375–424, 1997. (Cited on page 8.)

[30] M. Beckmann, A. Borissov, S. Brauksiepe, F. Burkart, H. Fischer, et al. The Longitudinal polarimeter at HERA. *Nucl.Instrum.Meth.*, A479:334–348, 2002. (Cited on page 38.)

[31] Andrei V. Belitsky, Dieter Mueller, L. Niedermeier, and A. Schafer. Leading twist asymmetries in deeply virtual Compton scattering. *Nucl.Phys.*, B593:289–310, 2001. (Cited on pages 16, 20, and 21.)

[32] A.V. Belitsky, Xiangdong Ji, and Feng Yuan. Quark imaging in the proton via quantum phase-space distributions. *Phys. Rev. D*, 69(7):074014, Apr 2004. (Cited on page 8.)

[33] A.V. Belitsky, D. Mueller, and A. Kirchner. Theory of deeply virtual compton scattering on the nucleon. *Nuclear Physics B*, 629(1-3):323–392, 2002. (Cited on pages 18 and 19.)

[34] J. Bertrand, P. Bertrand, and J. Ovarlez. *The Transforms and Applications Handbook: Second Edition*. CRC Press LLC, 2000. (Cited on page 23.)

[35] Angela S. Biselli. DVCS with longitudinally polarized target using CLAS at 6-GeV. *AIP Conf.Proc.*, 1149:611–614, 2009. (Cited on page 29.)

[36] Blanka Sobloher. Polarisation and Polarimetry at HERA. In *13th International Workshop On Polarized Sources And Targets & Polarimetry (PST 2009)*, 2009. (Cited on pages 38 and 39.)

[37] Jennifer Bowles, Jonathan Burns, Morgan Murray, Wolf-Dieter Nowak, Caroline Riedl, Sergey Yaschenko for the Recoil, and DVCS Groups. Addendum to the release reportAmplitudes of the single-charge beam-helicity asymmetry in DVCS off a hydrogen target with the proton remaining in the ground state", howpublished = addendum, note = Available online at `http://www-hermes.desy.de/reports/0411/DVCS-RECOIL/addendum_dvcs_timedep.pdf`; visited on Mai 29th 2013., year = 2011. (Cited on page 78.)

[38] Jennifer Bowles, Jonathan Burns, Morgan Murray, Wolf-Dieter Nowak, Caroline Riedl, Sergey Yaschenko for the Recoil, and DVCS Groups. Release report: amplitudes of the single-charge beam-helicity asymmetry in dvcs off a hydrogen target with the proton remaining in the ground state. 2011. (Cited on pages 62, 78, and 98.)

[39] Jean Buon and Klaus Steffen. Hera variable-energy mini spin rotator and head-on ep collision scheme with choice of electron helicity. *Nuclear Instruments and Methods in Physics Research Section A: Accelerators, Spectrometers, Detectors and Associated Equipment*, 245(2-3):248 – 261, 1986. (Cited on page 38.)

[40] J. R. T. Burns. *Deeply Virtual Compton Scattering off an Unpolarised Hydrogen Target at HERMES*. PhD thesis, University of Glasgow, Glasgow, United Kingdom, DESY-THESIS-2010-036, 2010. (Cited on page 77.)

[41] E. Burtin. Proposal for GPD studies at COMPASS. *AIP Conf.Proc.*, 1374:49–54, 2011. (Cited on page 32.)

[42] John C. Collins. Light cone variables, rapidity and all that. 1997. (Cited on page 10.)

[43] P. A. M. Dirac. Note on exchange phenomena in the thomas atom. *Mathematical Proceedings of the Cambridge Philosophical Society*, 26(03):376–385, 7 1930. (Cited on page 8.)

[44] Hovanes Egiyan and Angela S. Biselli. DVCS with a longitudinally polarized target with CLAS12. *AIP Conf.Proc.*, 1149:607–610, 2009. (Cited on page 32.)

[45] Latifa Elouadrhiri. Deeply Virtual Compton Scattering with CLAS12. 2008. (Cited on pages 32 and 33.)

[46] A. Airapetian et al. The hermes recoil detector. *ArXiv e-prints*, feb 2013. (Cited on pages 42 and 50.)

[47] Erik Etzelmueller. Measurement of asymmetries inassociated dvcs using the hermes recoil detector, 2013. (Cited on pages 81 and 82.)

[48] E. Etzelmüller. Completion of feasibility study of recoil tracking and extraction of beam-helicity asymmetry using scintillating fibre tracker only. Talk on analysis meeting, 2012. (Cited on page 64.)

[49] Andrea Ferrero. Study of DVCS and DVMP processes at COMPASS. *J.Phys.Conf.Ser.*, 295:012039, 2011. (Cited on page 29.)

[50] W. Heisenberg. Ueber die inkohaerente streuung von roentgenstrahlen. A / 1:627–630, 1985. (Cited on page 8.)

[51] HERMES. Recoil data quality. HERMES Offline Data Quality, 2010. Available online at `http://hermes.desy.de/groups/daqlgrp/OFFLINE_DQ/uDST/recoil/06f/`; visited on Mai 03th 2013. (Cited on page 56.)

[52] Achim Hillenbrand. Mc generators. Hermes Wiki, 1999. Available online at `https://hermes-wiki.desy.de/MC_Generators`; visited on April 22th 2013. (Cited on pages 97 and 101.)

[53] Xiangdong Ji. Gauge-invariant decomposition of nucleon spin. *Phys. Rev. Lett.*, 78:610–613, Jan 1997. (Cited on pages 1 and 23.)

[54] Xiangdong Ji. Generalized parton distributions. *Annual Review of Nuclear and Particle Science*, 54(1):413–450, 2004. (Cited on pages 8, 12, and 23.)

[55] Hyon-Suk Jo. Deeply Virtual Compton Scattering and Meson Production at JLab/CLAS. *AIP Conf.Proc.*, 1441:136–140, 2012. (Cited on pages 29 and 32.)

[56] Rudolph Emil Kalman. A new approach to linear filtering and prediction problems. *Transactions of the ASME–Journal of Basic Engineering*, 82(Series D):35–45, 1960. (Cited on page 45.)

[57] A. Kisselev. Htc status report. talk, 2008. Available online at http://www-hermes.desy.de/PLOTS/0809/CalibrationAndTrackingMeeting/htc-report-2008-09-04.ppt; visited on Mai 13th 2013. (Cited on page 45.)

[58] Donald E. Knuth. Computer Programming as an Art. *Communications of the ACM*, 17(12):667–673, December 1974. (Cited on page 119.)

[59] V.A. Korotkov and W.D. Nowak. Extraction of the generalized parton distribution H(xi,xi,t) from DVCS. *Nucl.Phys.*, A711:175–180, 2002. (Cited on page 17.)

[60] Valery Kubarovsky. Deeply virtual exclusive reactions with CLAS. *Nucl.Phys.Proc.Suppl.*, 219-220:118–125, 2011. (Cited on pages 31 and 32.)

[61] E. Leader and M. Anselmino. A crisis in the parton model: where, oh where is the proton's spin? *Zeitschrift für Physik C Particles and Fields*, 41(2):239–246, 1988. (Cited on page 7.)

[62] Elliot Leader. New relation between transverse angular momentum and generalized parton distributions. *Phys.Rev.*, D85:051501, 2012. (Cited on page 97.)

[63] C. Lorce and B. Pasquini. Hadron tomography through Wigner distributions. *ArXiv e-prints*, October 2011. (Cited on page 23.)

[64] M.F.M. Lutz et al. Physics Performance Report for PANDA: Strong Interaction Studies with Antiprotons. 2009. (Cited on page 32.)

[65] Gerald Matz and Franz Hlawatsch. Wigner distributions (nearly) everywhere: time-frequency analysis of signals, systems, random processes, signal spaces, and frames. *Signal Processing*, 83(7):1355–1378, July 2003. (Cited on page 8.)

[66] Silvia Niccolai. Deeply virtual Compton scattering at CLAS. page 93, 2008. (Cited on page 29.)

[67] O. Kouznetsov. Prospects for DVCS measurements using the COMPASS spectrometer at CERN. *AIP Conf.Proc.*, 1350:69–72, 2011. (Cited on pages 29, 32, and 33.)

[68] B. Pasquini and C. Lorce. Quark Wigner Distributions. 2011. (Cited on pages 8 and 10.)

[69] Silvia Pisano. Generalized parton distributions at CLAS. *Nucl.Phys.Proc.Suppl.*, 207-208:69–72, 2010. (Cited on page 29.)

[70] Bogdan Povh, Klaus Rith, Christoph Scholz, and Frank Zetsche. *Teilchen und Kerne*. Physics and astronomy online library. Springer, 2009. (Cited on pages 5 and 14.)

[71] R. Ramanathan. Some properties of an extended wigner function. *J. Comput. Appl. Math.*, 160(1-2):259–263, November 2003. (Cited on page 8.)

[72] Laurent Schoeffel. Deeply virtual compton scattering at HERA and perspectives at CERN. 2009. (Cited on pages 29, 30, and 31.)

[73] M. Stahl. *Improvement of the Theta+-Analysis at HERMES*. PhD thesis, JLU Giessen, 2010. (Cited on page 45.)

[74] Swadhin K. Taneja, Kunal Kathuria, Simonetta Liuti, and Gary R. Goldstein. Angular momentum sum rule for spin one hadronic systems. *Phys.Rev.*, D86:036008, 2012. (Cited on page 97.)

[75] A. Airapetian et al. The HERMES Collaboration. Separation of contributions from deeply virtual compton scattering and its interference with the bethe-heitler process in measurements on a hydrogen target. *Journal of High Energy Physics*, (11), 2009. (Cited on page 77.)

[76] M. Vanderhaeghen, Pierre A.M. Guichon, and M. Guidal. Deeply virtual electroproduction of photons and mesons on the nucleon: Leading order amplitudes and power corrections. *Phys.Rev.*, D60:094017, 1999. (Cited on page 24.)

[77] E. Wigner. On the quantum correction for thermodynamic equilibrium. *Phys. Rev.*, 40(5):749–759, Jun 1932. (Cited on page 7.)

[78] D. Zeiler. *Deeply Virtual Compton Scattering off an Unpolarized Hydrogen Target at the HERMES Experiment*. PhD thesis, Friedrich Alexander Universität Erlangen-Nürnberg, Erlangen, Germany, DESY-THESIS-2009-041, 2009. (Cited on page 77.)

[79] D. Zeiler and X. Lu. Combined analysis of the deeply virtual compton scattering process on the proton. *Fortschritte der Physik*, 42:101, 2008. (Cited on pages 46 and 47.)

— Donald E. Knuth [58]

ACKNOWLEDGMENTS

A dissertation is never only one persons work. Now it is time to thank the people who enabled the completion of this thesis.

I want to thank Prof. Michael Dueren, my supervisor for his advise and encouragement and for letting me figure out things at my own speed.

The HERMES group at DESY, especially Sergey Yaschenko and Caroline Riedl helped my with technical and scientific questions in many hours of Skype conferences, Carlotte van Hulse, Ami Rostomyan and Gunar Schnell for corrections, and advises and to Erik Etzelmueller and Hrachya Marukyan for seemingly endless cross checks.

Also i would to thank all the people who read my thesis for spell checks and mistakes, those are Peter Koch, Bernd Schmidt, and Jens Falter.

I thank my parents, my grandmother and my sister who believed in me and supported my efforts to find my way. I am grateful to my friends and flatmates, Peter, Bernd, Jörn and Daniel who helped me out when i was unsure how to overcome obstacles and to face challanges. A special thank to you.

ERKLÄRUNG ZUR DISSERTATION

Ich erkläre: Ich habe die vorgelegte Dissertation selbständig und ohne unerlaubte fremde Hilfe und nur mit den Hilfen angefertigt, die ich in der Dissertation angegeben habe. Alle Textstellen, die wörtlich oder sinngemäß aus veröffentlichten Schriften entnommen sind, und alle Angaben, die auf mündlichen Auskünften beruhen, sind als solche kenntlich gemacht. Bei den von mir durchgeführten und in der Dissertation erwähnten Untersuchungen habe ich die Grundsätze guter wissenschaftlicher Praxis, wie sie in der „Satzung der Justus-Liebig-Universität Gießen zur Sicherung guter wissenschaftlicher Praxis“ niedergelegt sind, eingehalten.

Giessen, February 21st, 2014

Irina Brodski